3D Finite Element Modelling of the Central Andean subduction zone with realistic geometry

Dissertation

zur Erlangung des akademischen Grades doctor rerum naturalium
(Dr. rer. nat.)

vorgelegt dem Rat der Chemisch-Geowissenschaftlichen Fakultät der
Friedrich-Schiller-Universität Jena

von Diplom-Geophysikerin Stefanie Zeumann
geboren am 21.11.1980 in Sömmerda

Gutachter
1. PD Dr. Thomas Jahr, FSU Jena
2. Prof. Dr. Gerhard Jentzsch, FSU Jena
3. Prof. Dr. Hans-Jürgen Götze, CAU Kiel

Tag der öffentlichen Verteidigung: 12. Juni 2013

Zusammenfassung

Subduktion ist ein komplexer Prozess mit vielen Aspekten, die berücksichtigt werden müssen bei der Modellierung von Subduktionszonen. Eine der interessantesten Subduktionszonen befindet sich am Westrand von Südamerika, wo die ozeanische Nazca-Platte unter die Südamerika-Platte abtaucht. Der zum Ozean hin konvex gekrümmte Trench (Tiefseegraben) ist einzigartig auf der Welt und die Anden sind das größte aktive Orogen, welches durch Subduktion gebildet wurde. Für die vorliegende Dissertation wurde ein Untersuchungsgebiet in den Zentral-Anden zwischen $17°S - 23.5°S$ and $60°W - 75.5°W$ ausgewählt. Das Gebiet hat damit eine Größe von 1630 x 725 km^2. Mit Hilfe der Finiten Elemente Methode (FEM) wurden dreidimensionale dynamische Modelle entwickelt um den Einfluss von unterschiedlichen Materialparametern und Randbedingungen auf die Deformationen in der kontinentalen Kruste zu untersuchen und mit einem Referenzmodel zu vergleichen. Die Geometrie der Modelle wurde von einem Dichtemodell, in das viele Randbedingungen aus Geophysik, Geologie und Petrologie eingegangen sind, übernommen. Des Weiteren wurde die Topographie der Anden in der Modellierung berücksichtigt. Zum ersten Mal wurde daher eine realistische Geometrie für eine dynamische Modellierung gewählt, die die heutige Situation im Untersuchungsgebiet beschreibt. Die Modellaufzeit beträgt 100 000 Jahre. Einerseits ist diese Zeitspanne länger als das Einlaufverhalten zu Beginn der Modellierung andererseits ist es ein kurzer Zeitraum im Vergleich zur Zeitspanne der Gebirgsbildung der Anden (∼40 Millionen Jahre). Die Modellierungsergebnisse geben daher die heutige Situation in den Anden wieder und können mit heutigen geodätischen und geologischen Beobachtungen verglichen werden. Die Modelle bestehen, wie das zugrunde liegende Dichtemodell, aus 16 Einheiten mit unterschiedlichen rheologischen Parametern und berücksichtigen sowohl die Lithosphäre als auch den Erdmantel bis in eine Tiefe von 410 km.

Die Modelle können anhand der Trench-Geometrie in einen südlichen Teil und eine nördlichen Teil unterteilt werden. Im Süden ist der Trench Nord-Süd ausgerichtet und die Nazca Platte bewegt sich nicht senkrecht zum Trench sondern in einem Winkel von 20°. Im Norden ist der Trench seewärts konkav gekrümmt und die Nazca Platte bewegt sich fast senkrecht zum Trench. Diese Geometrie und die daraus folgenden unterschiedlichen Bewegungsrichtungen beeinflussen sowohl die vertikalen Deformationen der kontinentalen Kruste, als auch den horizontalen strain. Die Ergebnisse des Referenzmodels zeigen eine Subsidenzrate (Absinkung) von -5 bis zu -9 mm/a für den nördlichen Teil und eine Hebungsrate von 2 bis zu 4 mm/a im südlichen fore-arc Bereich. Untersucht wurden die Deformationen (strain) in der kontinentalen Kruste. Nahezu das gesamte Model zeigt Kompression (Negative Werte). Nur im mittleren Teil des Modells tritt Dehnung im Küstenbereich auf. Die größten Kompressionen treten in den Prekordillieren und in den

Westkordillieren auf. Durch die Trench-Geometrie bedingt ist die Kompression im Süden jedoch stärker (Werte bis -0.006 strain) als im Norden (Werte bis zu -0.005 strain). Die für das Subandean aus den Modellergebnissen berechneten Verformungsraten (Strainraten) liegen bei -0.02 μstrain/a. Dieser Wert liegt in der gleichen Größenordnung wie die aus geodätischen und geologischen Beobachtungen abgeleiteten Strainraten. Die modellierten Verschiebungsraten in Ostrichtung passen gut zu aktuellen GPS-Messungen.

Aufgrund der wirkenden Gravitation und Zugkraft am unteren Ende der abtauchenden Platte (slab pull), tritt fast im gesamten Modell Subsidenz auf. Eine Verstärkung des slab pulls führt zu verstärkter Subsidenz, zu mehr kompressiver Verformung und zu einer schnelleren Bewegung in Richtung Osten.

Die Viskosität im Mantel beeinflusst die Deformationen in der kontinentalen Kruste. Eine Erhöhung der Mantelviskosität führt zu erhöhter kompressiver Verformung in den Westkordillieren und dem Subandean. Eine Erhöhung der Viskosität von 10^{21} Pa·s auf 10^{22} Pa·s verringert die Verformung in den Westkordillieren um 750 μstrain. Die Änderungen der Verschiebungsraten liegen bei ± 1 mm/a und somit innerhalb der Fehlerbereiche der GPS-Messungen.

Das Einfügen von viskoelastischem oder elastoplastischem Materialverhalten für die kontinentale Kruste führt zu stärkerer kompressiver Verformung, sowie zu stärkerer Subsidenz in den Westkordillieren und im Subandean, und zu verringerter Subsidenz im Bereich des Altiplano-Puna Plateaus. Dabei beeinflussen elastoplastische Eigenschaften die Ergebnisse stärker als viskoelastische Eigenschaften.

Die Spannungsverteilung auf der Oberfläche der abtauchenden Nazca-Platte lässt sich mit der Erdbebenverteilung im Untersuchungsgebiet korellieren. Die Richtung der maximalen horizontalen Spannung passt annähernd zu den Spannungsrichtungen der World Stress Map, die aus Herdflächenlösungen, Bohrloch Beobachtungen, und geologischen Beobachtungen bestimmt wurden.

Die Ergebnisse der Modellierung stimmen mit geologischen, geodätischen, und geophysikalischen Beobachtungen überein. Diese Beobachtungen können durch die hier dargestellten dynamischen Modelle mit ihren rheologischen Parametern und Randbedingungen erklärt werden.

Es wird gezeigt, wie wichtig die Geometrie und Dichte für die geodynamische Modellierung sind. Sowohl Dichten als auch Geometrie wurden aus einem existierenden Dichtemodell übernommen, welches anhand gravimetrischer Daten sowie Randbedingungen aus

Geophysik, Petrologie und Geologie erstellt wurde. Zum ersten mal wurde ein Dichtemodell als Basis für die Geometrien und Dichten dynamischer Modelle genutzt. Die Arbeit zeigt, dass dieser Ansatz erfolgreich ist und Dichtemodelle viel zur Entwicklung und Verbesserung dynamischer Modelle beitragen können.

Summary

Subduction is a complex process and many aspects have to be considered for modelling. One of the most interesting subduction zones is the western margin of Central South America, where the Nazca plate descends beneath the South American plate. In the area of southern Peru and northern Chile the oceanward concave curvature of the trench is unique on earth and the Andes are the largest active orogen caused by subduction. In this study 3D dynamic models of the Central Andes between $17°S-23.5°S$ and $60°W-75.5°W$ are created using the Finite Element Method (FEM). The models are 1630 x 725 km^2 wide and 410 km deep. For the first time the dynamic models include a realistic geometry taken from a well constrained density model describing the geometry and density distribution in the investigation area. Topography and curvature of the trench are part of the models. The models contain 16 units with different rheological parameters and consider lithospheric and asthenospheric domains up to a depth of 410 km. The effect of different parameters and boundary conditions on the deformation patterns in the continental crust is investigated and compared to the reference model. The models run for 100 000 years. On one side this timespan is longer than the running in behaviour at the beginning of modelling time, and on the other side it is a short timespan compared to the time scale of Andean orogeny ($\sim$40 million years). Therefore, the results can be regarded as the recent situation and can be compared with present day observations.

Due to the trench geometry the models can be distinguished in a southern part where the trench is straight and convergence velocity is oblique with an angle of 20°, and in a northern part where the trench has an oceanward curved shape and the convergence velocity is nearly perpendicular to the trench. This geometry and therefore different obliquity angles cause vertical deformation as well as the horizontal strain. The results of the reference model show a subsidence rate of -5 to -9 mm/a in the offshore fore-arc in the northern part but an uplift rate of 2 to 4 mm/a for the southern fore-arc region. Nearly the whole model shows compressional (negative values) east-west strain, except an area in the centre of the model within the fore-arc region. The highest compression occurs in the Precordillera and Western Cordillera (arc region). However, due to the trench geometry the compressional strain is higher in the southern part of the model with values up to -0.006 strain whereas in the northern part of the model values up to -0.005 strain occur only. Average strain rates calculated from the model results for the Subandean region are -0.02 μstrain/a which fits quite well to estimated strain rates from geological observations. The calculated east velocity fits quite well to the GPS measurements.

Nearly the whole model shows subsidence due to the applied gravitational force and the slab pull. Higher slab pull increases the subsidence rate, the compressional east-west

strain rate and the east velocity.

The viscosity of the asthenosphere affects the deformation pattern in the continental crust. Higher asthenosphere viscosities lead to lower compressional east-west strain in the Precordillera, Western Cordillera, and Subandean region. Increasing the viscosity from 10^{21} Pa·s to 10^{22} Pa·s lowers the compressional strain in the Western Cordillera about 750 μstrain. The changes in east velocity are smaller than ± 1 mm/a, which is within the error bars of the GPS measurements.

Including a viscoelastic or elastoplastic material behaviour for the continental crust leads to higher compressional east-west strain, to more subsidence in the Western Cordillera and Subandean region, and to less subsidence in the Altiplano plateau, compared to a pure elastic rheology of the crust. The bearing of elastoplasticity is stronger than of viscoelasticity.

The modelled stress pattern on the descending Nazca plate correlates with the earthquake distribution in the investigation area. Stress orientations in the continental crust fits to the maximum horizontal stress directions of the World Stress Map estimated from focal mechanisms, borehole breakouts, and geological indicators.

The results of the modelling fit to geological, geodetical, and geophysical observations. Therefore, these observations can be explained by the presented dynamic models with the used rheological parameters and boundary conditions.

It is shown how important the geometry and density are for geodynamic modelling. Densities and geometries were taken from an existent density model, which was developed from gravity data and constrainted by data from geophysic, petrology, and geology. For the first time a density model was used as basis for geometry and densities of dynamic models. This work shows that this is a successful approach and that density models can help a lot to develop and improve geodynamic models.

Contents

Zusammenfassung I

Summary V

1 Introduction and motivation 1

2 The subduction zone of Central South America 11
2.1 Geological setting . . . 11
2.2 The density model . . . 15
2.3 The seismic profile . . . 20
2.4 GPS measurements and strain rates . . . 22
2.5 Forces driving and resisting subduction . . . 23

3 Theoretical background 25
3.1 Physical equations . . . 25
3.1.1 Equations of equilibrium . . . 25
3.1.2 Conservation equations . . . 26
3.1.3 Elasticity . . . 27
3.1.4 Viscosity . . . 28
3.1.5 Viscoelasticity . . . 30
3.1.6 Plasticity . . . 31
3.2 Finite Element Method (FEM) . . . 33
3.2.1 HyperMesh . . . 34
3.2.2 ABAQUS . . . 34

4 Numerical modelling 39
4.1 From static density model to finite element modelling . . . 40
4.2 Model set up . . . 41
4.2.1 Model geometry . . . 41
4.2.2 Boundary conditions . . . 42
4.2.3 Interactions . . . 43
4.2.4 Implementing gravity . . . 45
4.2.5 Material parameters - Model rheology . . . 47

4.2.6 Model assumptions and restrictions 49

5 Results **53**

5.1 Results of the reference model 54
5.2 Effect of gravity 62
5.3 Effect of slap pull 63
5.4 Effect of mantle viscosity 66
5.4.1 Non-Newtonian viscosity in the uppermost continental asthenosphere 66
5.4.2 Variation of mantle viscosity 67
5.5 Effect of viscous lithosphere 72
5.6 Effect of upper continental crust rheology 74
5.7 Effect of density of the upper continental crust 79
5.8 Effect of homogeneous slab 83
5.9 The stress pattern on the Nazca plate 85
5.10 The stress pattern on the continental crust 88

6 Conclusions and future research **89**

References **106**

Appendix **i**

Acknowledgements **ix**

Selbstständigkeitserklärung **xi**

1 Introduction and motivation

The lithosphere of the earth consists of several main and micro plates drifting on the asthenosphere (e.g. *Bird*, 2003). The idea of a lithosphere, representing a strong outer layer of the earth overlying a weak asthenosphere, was first introduced by *Barrel* (1914), long before the realization that the outer shell of the earth forms a thermal boundary layer of a convecting system (*Wessel and Müller*, 2009). The concept of seafloor spreading was originally proposed by *Dietz* (1961) and *Hess* (1962), who suggested that new seafloor is created at mid-ocean ridges, spreads away from the mid-ocean ridges as it ages, and is subducted back to the mantle at subduction zones (*Wessel and Müller*, 2009). *Wilson* (1965) suggested that the active mobile belts on the surface of the earth, marked by active seismicity, separate the earth into a set of rigid plates and that these belts consist of ridges, where plates are created, trenches, where plates are destroyed, and transform faults, which connects the other two belts to each other (*Wessel and Müller*, 2009). The relative motion of the plates gives rise to earthquakes and these earthquakes define the plate boundaries. Three types of plate boundaries are distinguished today: Divergent plate margins, where new oceanic lithosphere is created, convergent plate margins where lithosphere is destroyed because one plate descend beneath another, and transform boundaries where lithosphere is neither produced nor destroyed and the plates slide horizontally past each other (*Wessel and Müller*, 2009). There are regions where plate boundary zones involve more than two plates which lead to complicated geological structures and earthquake patterns. Different methods can be used to determine the instantaneous relative plate motions (e.g. *Wessel and Müller*, 2009 and references therein). A global model for current plate motions based on different methods has been constructed by e.g. *DeMets et al.* (1990), *DeMets* (1995) or *Prawirodirdjo and Bock* (2004).

Oceanic lithosphere originates from mid-ocean ridges as hot material. Depending on the spreading rate of the mid-ocean ridge the oceanic lithosphere moves away at it ages, cools down, and densifies. The spreading rate of a mid-ocean ridge can be determined from the magnetic anomaly patterns at the ocean floor and consequently the age of the oceanic lithosphere can be determined. Global models of ages of oceanic lithosphere were developed by *Müller et al.* (1997) and *Müller et al.* (2008). At subduction zones the oceanic lithosphere descends into the mantle because it is cooler, denser, thinner, and consequently weaker than continental lithosphere. Due to the outer bending of the oceanic

plate subduction results in large ocean trenches (e.g. *Press and Siever*, 2003) like the Japan trench east of Japan, the Aleutian trench reaching from Kamchatka to Alaska, or the Middle America Trench west of Central America. The deepest trench of the world is the Mariana trench east of the Philippines with a maximum depth about 11 000 m (*Leier*, 2007). Magmatic arcs are also consequences of subduction processes. The cold oceanic lithosphere subducts into the warmer mantle and the temperature in the lithosphere rises during descending. Therefore, the plate loses water and other volatiles by dehydration. These volatiles rise to the above lying mantle wedge and cause melting processes. Melted material rises to the surface and forms the volcanic belt at the surface. The volcanic or magmatic arc can be an island arc if one oceanic plate descends beneath another oceanic plate like Japan or it lies on the continental lithosphere like in South America. Another feature occurring at subduction zones is the development of large orogenic belts on the continental plate behind the magmatic arc. The most prominent orogen of this type is the Andes orogen on the western margin of South America.

Much research has been done so far that deal with the parameters that control the tectonic regime in a subduction zone (e.g. *Forsyth and Uyeda*, 1975; *Jarrard*, 1986; *Doglioni et al.*, 2007; *Heuret and Lallemand*, 2005; *Cruciani et al.*, 2005; *Schellart*, 2008; *Guillaume et al.*, 2009). The authors have shown that a large variety of structural environments and plate interactions at convergent plate margins can be illustrated by two end member types, the Marianas and the Peru-Chile plate boundary (*Ramos*, 2010). After *Uyeda and Kanamori* (1979) the Marianas type is characterized by an old oceanic crust that is underthrusting a tensional overriding plate, accompanied by relatively modest maximum earthquakes. In contrast the Peru-Chile type is characterized by rapidly converging and younger oceanic crust that is underthrusting a compressional overriding plate. But these are the end members only.

Regions with active subduction zones have the largest natural hazards of the world. Besides active volcanoes in the magmatic arc the largest earthquakes occur in subduction zones due to the frictional coupling between the descending and overriding plate. Prominent subduction zones with large disastrous earthquakes are for example: The eastern margin of Japan (e.g. Tohoku eartquake 2011 9.0); Sunda at the western margin of Indonesia (e.g. Sumatra earthquake 2004 9.1); Hikurangi at New Zealand (Christchurch 2011 6.1); the western margin of Middle America (e.g. Costa Rica earthquake 2012 7.6); Aleutian reaching from Kamchatka to Alaska (Alaska earthquake 1964 9.2); the western margin of South America (e.g. Valdivia earthquake 1960 9.5; Maule earthquake 2010 8.8) (Magnitudes from USGS).

One of the most interesting subduction zones for geodynamic studies is the western margin

of Central South America where the oceanic Nazca plate descends beneath the continental South American plate (Figure 1.1). After *Oncken et al.* (2006a) the subduction of the Nazca plate is going on since at least Jurassic time creating the Peru-Chile trench with a depth up to 8000 m (*Leier*, 2007) and the Andes. With an entire length of more than 7000 km (N-S) and a width of over 800 km in the central part (*ANCORP Working Group*, 2003), the Andes are the largest active orogen caused by subduction. The seaward concave bending of the trench between 10°Sand 25°S is unique

For a long time the Andes are a research interest and many geological, geophysical, geodetical, and petrological observations and measurements have been realized to learn more about subduction zone processes and developing of the Andes. Lots of data and results were gained during the Colaborative Research Center (SFB 267) "Deformation processes in the Andes" and presented in different publications and dissertations (e.g. *ANCORP Working Group*, 2003; *Hindle et al.*, 2002; *Oncken et al.*, 2006b; *Reutter and Götze*, 1994; *Sobolev and Babeyko*, 2005). Investigations of the Nazca plate were done for example by *Mahatsente et al.* (2012).

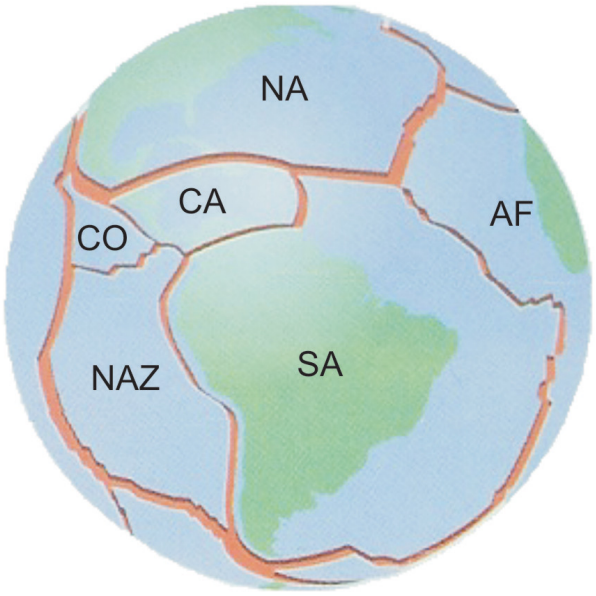

Figure 1.1: Plate mosaic around South America region: AF - African plate, CA - Caribian plate, CO - Cocos plate, NA - North American plate, NAZ - Nazca plate, SA - South American plate (after *Dumont Weltatlas*, 2003).

After (*Ramos*, 2010) there is some consensus that the main parameters that control the geometry, coupling, and tectonic setting of Andean-type subduction zone are: length of

Benioff zone, relative convergence rate, age of the descending slab, slab dip angle, direction of mantle flow, absolute motion of the overriding plate and slab retreat among others (*Jarrard*, 1986; *Doglioni et al.*, 2007; *Oncken et al.*, 2006a). In the last years the influence of climate has been investigated (e.g. *Montgomery et al.*, 2001; *Lamb and Davis*, 2003). Another main factor controlling the uplift in the Andes is the frictional coupling between the two plates (e.g. *Hampel and Pfiffner*, 2006; *Sobolev and Babeyko*, 2005). The friction is directly related to the amount of sediments in the trench. Starving trenches under extreme arid conditions like in the Central Andean region have a maximum coupling, while overfilled trenches in humid climates like in the southernmost or northernmost part of the Andes have a minimum of coupling. Second order features like the collision with a seismic ridge or fracture zones may influence the regional stress state of the overriding plate, and localized tectonics in the Andes (e.g. *Gutscher et al.*, 2000; *Ramos*, 2005; *Ramos*, 2010).

For this work an investigation area between $17°S - 23.5°S$ and $60°W - 75.5°W$ in the Central Andes was chosen (rectangle in Figure 1.2). This area includes the oceanward concave curved trench, which is unique on earth. The descending Nazca plate in this region has an crustal age of ∼50 Ma (*Müller et al.*, 2008). Because, of former investigations (e.g. SFB 267) there are a lot of geophysical, geological, and petrological information available which can be used as constraints for this work. The black arrows in Figure 1.2 denote the plate velocities and the direction of motion used for the investigations in this study.

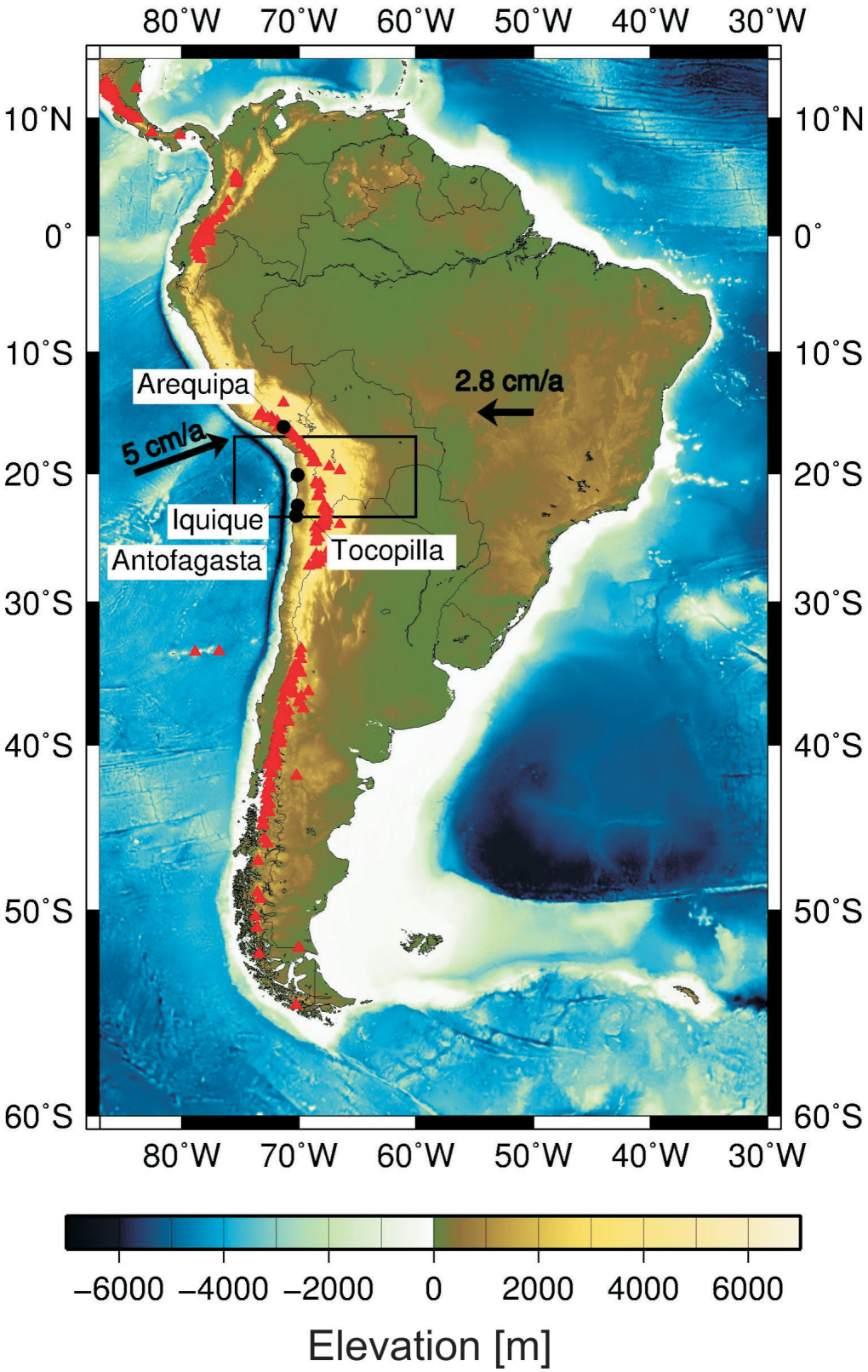

Figure 1.2: Map of South America: Rectangle marks the investigation area of this work, black arrows indicate the plate velocities after *Somoza* (1998) and *Silver et al.* (1998), and red triangles denote the volcanoes (www.volcano.si.edu/world/).

Besides observations and measurements numeric modelling has been established in geosciences. Subduction is a complex active dynamic process and therefore dynamic modelling is essential for a better understanding of these processes. For developing such models boundary conditions are necessary gained from independent measurements, observations, and geological prospects (e.g. seismic measurements, density modelling). As mentioned before subduction is a complex process with many aspects to be considered. However, due to limitation of computational capacity dynamic models cannot consider all aspects. Therefore, several authors and working groups investigated subduction zone processes by dynamic modelling in 2 dimensions (2D) as well as in three dimensions (3D). Some models are generic not related to a special subduction zone, but investigating the principal basics of subduction e.g. onset of subduction. Other models are created to represent one special subduction zone using available information about the specified region (e.g Moho depth or slab geometry from seismic data). Some of existing 2D and 3D dynamic models related to subduction zones especially to the Andean subduction zone are discussed shortly in the following passage, but the listing will not fulfil the demand of completeness.

Liu et al. (2002) simulate viscoelastic finite-element 3D models to investigate the spatial distribution of the Andean crustal shortening. The South American plate was modelled with a depth of 70 km and a six layer lithosphere with variable viscosities. The movement of the Nazca plate was realized by boundary conditions. Therefore, no slab or interplate coupling is included in the models. The authors found a nearly uniform short-term velocity gradient across the Andes, which is consistent with measured GPS data and a concentrated long-term crustal shortening which is consistent with geolocical observations. The movement of the continental plate is neglected in these models. But, *Hampel and Pfiffner* (2006) found in elasto-visco-plastic 2D models with a depth of 100 km, that the trenchward motion of the continental plate plays a key role for the development of mountain belts at convergent plate margins like the Andes in South America. The downward drag of the subducting plate is a combination of slab pull and interplate coupling. The motion of the continental overriding plate overcomes this downward drag which results in high topography on the continental plate depending on the friction coefficient between the two plates. Due to the fact of the low model depth the asthenosphere is not included in the above mentioned model approaches and also thermodynamic effects were neglected. Other authors (e.g. *Sobolev and Babeyko*, 2005; *Babeyko and Sobolev*, 2008) developed thermomechanical elasto-visco-plastic models in 2D with a depth of 400 km and investigated mainly the stress distribution in the descending slab. They found a double zone of compression in the upper part of the slab and a zone of extension below. They conclude that the stress in the slab is mainly controlled by the velocity of the overriding plate and the direction of slab pull force. Due to the fact that they are 2D these models cannot consider oblique convergence velocities.

Deformation caused by oblique convergence were investigated in elasto-plastic 3D models with a depth of 180 km by *Kellner* (2007). The investigation was concentrated on the fore-arc and asthenosphere is not included in the model. The intensity of deformation increases significantly with an increasing obliquity angle. It was also found that the friction coefficient in the northern part of the Chilean subduction zone is reduced compared to the friction coefficient of the southern region, which is probably compensated by an increasing width of the friction zone in the southern investigation area (see also *Hoffmann-Rothe et al.* (2006)).

Because obliquity influences the deformation trench geometry should be taken into consideration. This was done for example by *Bonnardot et al.* (2008), *Boutelier and Oncken* (2010) or *Gassmöller* (2011). All authors found that trench geometry controls the stress and strain pattern in the upper plate. An oceanward convexity causes an accumulation of the subducted material beneath the upper plate and induces an important uplift, whereas an oceanward concavity causes subsidence in the fore-arc zone (*Bonnardot et al.*, 2008). *Boutelier and Oncken* (2010) conclude that a trench parallel compression in the centre of an oceanward concave curved plate boundary can be produced by the stress conditions along the interplate zone. Low dip angle and high convergence obliquity favour trench parallel compression in the centre of curvature.

The aim of this work is to investigate the deformation pattern in the fore-arc and back-arc region at the subduction zone region of the Central Andes depending on several rheology parameters and boundary conditions and compare the results with geodetic and geological observations. Investigated are the influence of slab pull, varied asthenosphere viscosities, as well as different rheologies of the lithosphere and upper continental crust.

All modelling approaches mentioned above have more or less generic model geometries. One aim for this work is to achieve a most realistic geometry of the Central Andean subduction zone for the dynamic models. This aim leads to the question how to get this geometry. One possibility are density models based on gravity data. From measured gravity data the Bouguer anomaly can be calculated. The density models are developed by forward modelling with the aim that the modelled Bouguer anomaly fits the observed Bouguer anomaly. For this many constraints from geophysical, petrological, and geological data are used. At the end one have a 3D model with a realistic structure and densities describing the observed Bouguer anomaly in the investigation area.

The approach for this work is now to take a constrained density model and transfer the geometry and densities to dynamic models. With this approach density models can

improve the dynamic modelling.

Terrestrial gravity measurements are not available in every region of the world. Satellite missions like GRACE and GOCE have significantly improved the coverage and availability of gravity data and can improve density models lacking terrestrial data (e.g. *Reigber et al.*, 2005; *Mayer-Gürr*, 2007; *Pail et al.*, 2010; *Pail et al.*, 2011). Compared to terrestrial data satellite data have lower spatial resolution but, it is sufficient for interpretation of large-scale structures (*Köther et al.*, 2012). Higher resolution is provided by combined gravity models of satellite-derived and terrestrial data (e.g. *Förste et al.*, 2012; *Pavlis et al.*, 2008). Including satellite-derived gravity data will improve density models and if these density models can be taken as basis for dynamic models the satellite data will indirectly improve the dynamic modelling.

Various 3D density models exist showing the mass distributions at regional and more global scales of the subduction zone of South America (*Strunk*, 1990; *Kirchner et al.*, 1996; *Kösters*, 1998; *Tašárová*, 2007; *Tassara et al.*, 2006; *Prezzi et al.*, 2009). For this work the density model of *Tassara et al.* (2006) was chosen as the structural basis for the dynamic models, because it encompasses the bent trench region which was chosen as investigation area for the dynamic models.

The finite-element models presented in this work describe the region between $17°S - 23.5°S$ and $60°W - 75.5°W$ in the Central Andes (rectangle in Figure 1.2). Like the density model the dynamic models are 410 km deep which means they include parts of the asthenosphere. They are 3D and include the oblique convergence of the Nazca plate as well as the trenchward motion of the South American plate. Further, the oceanward concave curved trench geometry in the region of the Central Andes is regarded. The effect of gravity is included in all models. The models have a most realistic structure taken from a well constrained density model. The slab is not homogeneous but divided in several parts, implicating the densification with depth due to metamorphic phase transitions. The rheological parameters are taken and calculated from the density model and seismic data. Therefore, for the first time models of the Central Andes were developed using a most realistic geometry and rheological parameters.

The models run for 100 000 years. Due to the fact that the geometry taken from a density model describes the present situation the model results show the future. But, the timespan of 100 000 years is very short compared to the time span of subduction and orogenesis and therefore the modelled results can be considered as recent and compared to recent observations .

This study was accomplished within the project NOGAPSGRAV (NOvel Geophysical And Petrological applications of new-generation Satellite-derived GRAVity data with a focus on hazardous and frontier regions) and the follow on project IMOSAGA (Integrated Modelling Of Satellite and Airborne Gravity data of Active plate margins). The projects are in cooperation with the university of Kiel and TU Munich and have been parts of the priority program "Mass transport and mass distribution in the system Earth" (SPP1257) of the German Research Foundation (DFG).

The frictional coupling between the subducting Nazca plate and the overriding South America plate plays a major role for the deformation and stress pattern in the continental crust (e.g. *Hampel and Pfiffner*, 2006). The frictional parameters as friction coefficient or width of coupling zone are not discussed in this thesis, but a separate work within the IMOSAGA project has been investigate the influence of frictional behaviour (Sharma in prep.). The results show that the trenchward movement of the overriding plate is essential to build high orogens and that a high friction coefficient induces subsidence whereas a low friction coefficient supports uplift, which is consistent with the results of *Hampel and Pfiffner* (2006). Beside frictional parameters the differences between a steep subduction region and a flat subduction region along the South American margin have been investigated (Sharma in prep.).

2 The subduction zone of Central South America

2.1 Geological setting

The Andean Cordillera along the edge of western South America is the result of subduction of the oceanic Nazca plate beneath the South American plate. Andean subduction has been going on since at least Jurassic time (*Oncken et al.*, 2006a). This development leads to the earth largest active orogen caused by subduction with an entire length of more than 7000 km (N-S) and a width of over 800 km in the central part (*ANCORP Working Group*, 2003). *Somoza* (1998) investigated the changes in the relative motion of the Nazca plate with respect to a stable South America for the last 40 million years. The results suggest for the Nazca plate a NE-SW convergence of 5-8 cm/a during the early Cenozoic and increased abruptly to ∼15 cm/a and an E-W convergence about 26 million years ago. After this the velocity decayed to the present value of 7.8 cm/a (22°S) absolute motion and an obliquity of 20° with respect to a stable South America. The absolute motion of South America increased during the last 30 million years from 2 cm/a to 2.8 cm/a (*Silver et al.*, 1998). Therefore, in this work relative motions of 5 cm/a are considered in NE direction (20° obliquity) for the Nazca plate and 2.8 cm/a in west direction for the South American plate (black arrows in Figure 1.2).

The Peru-Chile trench is up to 8000 m deep (*Leier*, 2007) and the Central Andean margin between 5°N-34°S is known as a prominent erosive margin since the 1970's (*Rutland*, 1971). This means erosion of continental material at the base of the upper plate during subduction. Some characteristic features for subduction erosion observed in the Central Andes are (1) migration of the volcanic arc, (2) continental margin retreat, (3) high convergence rate, (4) no or minor sediment input, (5) high roughness, (6) fore-arc extension and fore-arc subsidence (*Kukowski and Oncken*, 2006, and references therein).

The Andes are characterized by along strike variations like subduction geometry, topography, volcanism, tectonic and geological units, etc. (e.g. *Jordan et al.*, 1983; *Oncken et al.*, 2006a; *Haschke et al.*, 2006; *Kley et al.*, 1999). Following the differentiation of (*Tassara et al.*, 2006) the Andes can be separated in a northern part (10°N-5°S), a central

part (5°S-33.5°S), a southern part (33.5°S-46.5°S) and an austral part (46.5°S-56°S).

Several trench parallel tectonic units can be distinguished (e.g. *Mpodozis and Ramos*, 1989; *Reutter and Götze*, 1994). The units shown in Figure 2.1 are depicted from *Tassara* (2005). From west to east they are: offshore and onshore fore-arc region, Western Cordillera (WC), Altiplano plateau (AP) and Puna plateau (PU), Eastern Cordillera (EC) and Subandes (SubA). The onshore fore-arc in the Central Andes is further subdivided into different units. From west to east these are the Coastal Cordillera (CC) with an average elevation of 1000 m and peaks up to 3000 m, the Longitudinal Valley (LV) and the Precordillera (PC) with altitudes up to 4300 m. The fore-arc region contains two big trench parallel fault systems, the Atacama Fault Zone (AFZ) located in the Coastal Cordillera initiated in the late Jurassic and the Precordilleran Fault System (PFS) formed in the late Eocene. However, the fault systems are not included in the dynamic models.

The magmatic arc experienced an east ward shift in four stages (e.g. *Scheuber et al.*, 1994; *Haschke et al.*, 2006): The Jurassic arc (195-130 Ma) along the Coastal Cordillera (CC in Figure 2.1), the mid Cretaceous arc (125-90 Ma), aligning with the Longitudinal Valley (LV) and the late Cretaceous-Eocene arc (78-37 Ma) along the Precordillera (PC). The active (26 Ma-recent) magmatic arc is located in the Western Cordillera (WC) approximately 200 km away from the trench and 100 km above the Wadati-Benioff zone (*ANCORP Working Group*, 1999). There are two gaps in the magmatic arc between 3°S-13°S (Peru) and 27°S-34°S (Central Chile) where no volcanism occurs (Figure 1.2). These gaps correlate with flat subduction segments. In contrast to normal subduction segments with a mean dip angle of 30°, the flat subduction segments descend at 30° down to a depth of 100 km, than proceeding nearly horizontal for several hundred kilometers before bending again. Flat subduction changes the thermal structure by displacing the hot asthenospheric wedge away from the trench (*Gutscher et al.*, 2000; *Gutscher*, 2002). Assuming that the down dip limit of the seismogenic zone is controlled by the 350-450°C isotherms (*Tichelaar and Ruff*, 1993; *Oleskevich et al.*, 1999) the cooler temperature of the fore-arc predicts a larger seismogenic zone. Further, higher degree of upper plate seismicity was observed over flat subduction segments implying a higher degree of interplate coupling (*Gutscher et al.*, 2000).

The morphology of the Central Andes is dominated by high plateaus: the Altiplano between 15°S-23°S with nearly constant elevation of ∼3.8 km, and the Puna 23°S-28°S with an averaged elevation of ∼4.2 km and higher relief. The Altiplano-Puna plateau extends about 1800 km north to south and about 200 - 450 km west to east with the maximum extension in the bent of the Bolivian orocline at circa 18°S (*Barnes and Ehlers*, 2009).

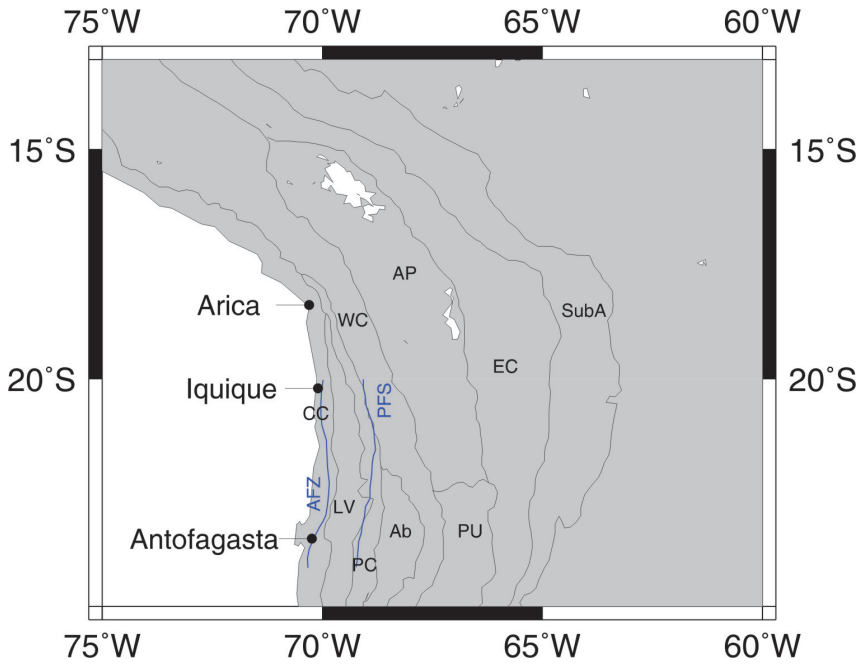

Figure 2.1: Morphotectonic unit boundaries are depicted from *Tassara* (2005) (modified from *Mpodozis and Ramos* (1989)), fault zones are depicted from *Kellner* (2007): CC Coastal Cordillera, LV Longitudinal valley, PC Precordillera, Ab Atacama basin, WC Western Cordillera, AP Altiplano, PU Puna, EC Eastern Cordillera, SubA Subandean, AFZ Atacama Fault Zone, PFS Precordilleran Fault System

Uplift history of the Andean plateau is not fully understood yet. *Barnes and Ehlers* (2009) evaluate opposed models for the surface uplift including a slow and steady rise of the plateau since ∼40 million years ago and a model with rapid rise of 2.5 km ∼10-6 million years ago. They found that the steady uplift model is more consistent with available observations. The eastern border of the Altiplano-Puna plateau is the Eastern Cordillera with peaks up to 5000 m. The uplift rate for the Altiplano plateau and the Eastern Cordillera estimated from Paleoelevation data is 0.2-0.3 mm/a for the last 10 million years (*Gregory-Wodzicki*, 2000). The Subandean east of the Eastern Cordillera is characterised by a thrust and fold belt and represents the thin-skinned foreland of the Central Andes. South of 23 °S the foreland thrusting structure changes first to a thick-skinned inversion structure in the Santa Babara System (*Kley and Monaldi*, 2002) and then to large-scale basement thrusts in the Sierras Pampeanas (*Oncken et al.*, 2006a).

Since the compilation of shortening rates by *Kley and Monaldi* (1998), several shortening rates estimated from balanced cross sections have been published (e.g. *Kley and Monaldi*, 2002; *Victor et al.*, 2004; *Elger et al.*, 2005). *Oncken et al.* (2006a) compiled published data of shortening rates and deformation time. However, most cross sections cover the foreland belt only and sections over the entire mountain belt are rare. In the

Central Andes between 17°S and 21°S the total post Eocene shortening is nearly constant with values about 250-275 km and decreases to a poorly constrained value of some 120 km north and south of this segment (*Oncken et al.*, 2006a).

The short overview of evolution of shortening given here is following the work of *Oncken et al.* (2006a). Shortening starts in the Precordillera/Western Cordillera around 46 Ma ago. The Precordillera/Western Cordillera has experienced two phases of shortening between 46-36 Ma with a shortening rate of 1 mm/a and a second phase between 30-7 Ma with shortening rates one order of magnitude lower. For the Altiplano two main stages can be identified. The entire western and central Altiplano was affected by shortening during the Oligocene (35-25 Ma) with local shortening rates of 0.1 to 3 mm/a. After this there was a lull of deformation during early Miocene until in the middle to late Miocene (20-10 Ma) a second phase of deformation with shortening rates of 1.7 to 3 mm/a occurred. The Eastern Cordillera experienced shortening over long time starting about 40 Ma ago with a maximum shortening rate of 6-9 mm/a between 30 and 17 Ma. Deformation ceased between 12 and 8 Ma and shifted eastwards. The Subandean fold and thrust belt was initiated with shortening rates about 8-14 mm/a with maximum rates around 7 and 2 Ma. *Bevis et al.* (2001) investigated GPS measurements and found present shortening rates between the GPS stations in the Subandean region and the stable South American craton of ∼9.5 mm/a at 18.5°S and of ∼6.5 mm/a at 21.5°S.

Several geophysical observations found a thickened crust up to 70 km beneath the Central Andes (*Wigger et al.*, 1994; *ANCORP Working Group*, 1999; *Giese et al.*, 1999). This crustal thickness and the present-day topography cannot be explained by the observed shortening of 275 km alone. Other processes like magmatic addition (*Lamb and Hoke*, 1997), thinning (delamination) of the mantle (*Pope and Willett*, 1998), lower crustal flow (*Kley and Monaldi*, 1998), and deep mantle flow (*Russo and Silver*, 1996) may also contribute to the evolution of the Andes (*Stein and Sella*, 2002).

2.2 The density model

Several 3D density models exist showing the mass distributions at different scales of the subduction zone of South America (*Strunk*, 1990; *Kirchner et al.*, 1996; *Kösters*, 1998; *Tašárová*, 2007; *Tassara et al.*, 2006; *Prezzi et al.*, 2009). For the Central Andes (*Strunk*, 1990; *Kirchner et al.*, 1996; *Prezzi et al.*, 2009) and the Southern Central Andes (*Tašárová*, 2007) 3D density models at a regional scale have been developed, whereas *Tassara et al.* (2006) presented a more global density model encompassing the Pacific Ocean and the Andean margin between northern Peru (5°S) and Patagonia (45°S) (Figure 2.2).

For this work the density model of *Tassara et al.* (2006) was chosen as the structural basis for the dynamic models, because it encompasses the bent trench region which was chosen as investigation area for this study. A short description of the density model is given here for more details see *Tassara* (2005) and *Tassara et al.* (2006).

The database for this model was acquired over the last 30 years. The offshore Bouguer anomalies were computed from the KMS01 satellite derived free-air anomaly database (*Andersen and Knudsen*, 1998). Lots of onshore data were measured between 1982 and 1990 and in 2000 (*Götze et al.*, 1994; *Götze and Krause*, 2002; *Schmidt and Götze*, 2006). Aditional data were provided by the Chilean and Argentinean oil industry, different academic groups in Chile, Argentina and Bolivia, and governmental institutions (*Schmidt and Götze*, 2006). The database was provided in the framework of a cooperation agreement with the German Collaborative Research Centre SFB267 "Deformation Processes in the Andes".

Approximately 20 000 stations were used for the Bouguer map and after *Tassara et al.* (2006) the presented Bouguer anomaly (Figure 2.2) has an average uncertainty of ±20 mGal (1 mGal $=10^{-5} m/s^2$). The observed Bouguer anomaly reveals a negative anomaly up to -450 mGal in the central Andean orogen (Figure 2.2). The uncertainty of ±20 mGal (*Tassara et al.*, 2006) is small enough in comparison to the total range of Bouguer values from 400 to -400 mGal.

The density model was created by forward modelling of the Bouguer anomaly using the software IGMAS (*Götze and Lahmeyer*, 1988; *Schmidt and Götze*, 1998; *Schmidt et al.*, 2010). For model input the user has to define the geometry and density of each modelled unit on a series of parallel vertical cross sections. The software triangulates between these cross sections forming three dimensional bodies and calculates the resulting anomaly. By interactively changing geometry and density of the units the user has to find an optimal fit between the observed Bouguer anomaly and the calculated anomaly. Because there

is more then one solution for the modelling further constraints from other geophysical methods (e.g. seismic), geology and petrology are needed for modelling.

The resulting density model has 43 cross sections (black lines in Figure 2.2) separated by 1° in latitude with a length of 3000 km and a depth of 410 km. Figure 2.3 shows one cross section (white line in Figure 2.2) of the density model with several units and densities. The coordinates used for the models are UTM coordinates with meridian 19 ($69°W$) as a reference. The difference between observed and modelled Bouguer anomaly is a possibility to quantify the accuracy and quality of the gravity model. At wavelengths greater than some hundred kilometres the residual anomalies lie within the average uncertainty of the Bouguer map ($\pm$20 mGal). Less than 10 % of the investigation area have residual anomalies bigger than 20 mGal and these anomalies have short wavelengths ($<$ 300 km). The final density model reproduces the regional- to continental-scale features of the observed Bouguer anomaly with an accuracy better than the error in the measured anomaly, which means that the model represents the mass distribution along the Andean margin fairly well (*Tassara et al.*, 2006).

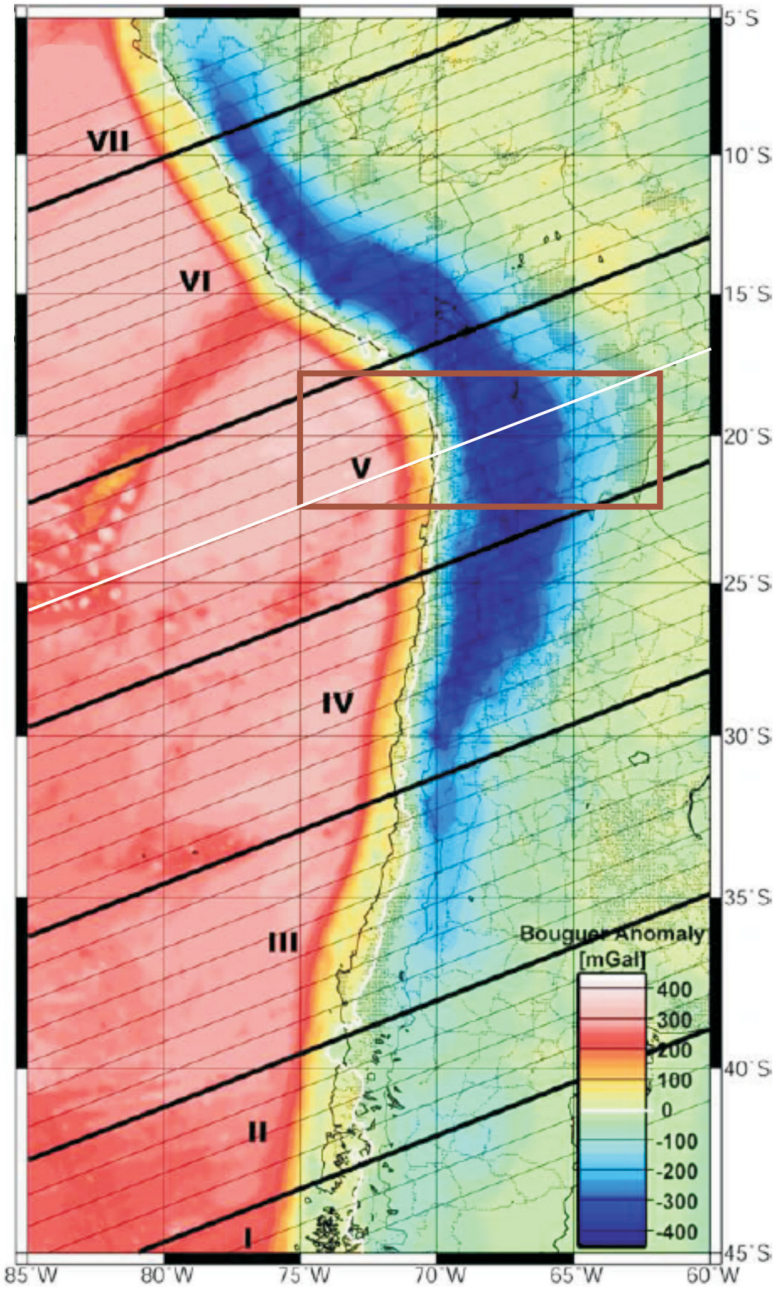

Figure 2.2: Bouguer anomaly map (*Tassara et al.*, 2006): Black lines mark the 43 cross sections from the density model. The white line marks the cross section shown in Figure 2.3, and the rectangle denotes the area of the investigation area of this work.

The oceanic Nazca plate is formed by a one-layer crust (OC) overlying a mantle lithosphere body (OM). The initial thickness of the oceanic crust was 7 km, the average global value and then the Moho was adjusted to fit the constraints given by refraction seismics and fitting the measured Bouguer anomaly. Seismic investigations worldwide show that the oceanic crust can be divided in 3 seismic layers: layer 1 representing the sediments, and the dominant basalt and gabbro bearing layers 2 and 3. The density of 3050 kg/m^3 for the oceanic crust implies a mixture of 85 % fresh basalts and gabbros and 15 % fully metamorphed basalts, which is adequate for the seismic layers 2 and 3. The sediment layer is not considered for the calculation of the average crustal density because seismic profiles show only a thin layer lower than 300 m of sediments for the Nazca plate (*Krabbenhöft et al.*, 2004). For modelling the geometry and density of the oceanic lithospheric mantle petrology and the age of the incoming Nazca plate were taken into account. Due to metamorphic reaction under high temperatures and pressures the descending slab changes its composition with depth and therefore a densification occurs. Hence, OC and OM are divided in several parts (I to V) with different densities increasing with depth. Beneath the oceanic lithosphere there is one body representing the oceanic asthenospheric mantle (OA). The continental South American crust is separated in an upper (UC) and lower (LC) part. The density of 2700 kg/m^3 corresponds to a felsic upper crust ($\sim$ 70 wt % SiO_2) whereas LC represents an intermediate to mafic lower crust with a density of 3100 kg/m^3 suitable for a composition of andesitic to basaltic rocks (60-50 wt % SiO_2). The boundary between upper and lower crust is not constrained by independent information and it was adjusted to fit the Bouguer anomaly (*Tassara et al.*, 2006).

The continental crust overlies an eastern (MW) and a western (CM) mantle lithosphere. CM represents the cold and dense mantle lithosphere below the Andean foreland and shield regions. WM underlies the fore-arc and the hot volcanic arc and should therefore be less dense then CM. For the same reason the upper continental asthenosphere above 150 km is also divided in an eastern (UCAe) and a western (UCAw) part overlying a single lower asthenosphere body (CA).

The geometry and densities of this model are the best possible solution to fit the observed Bouguer anomaly using all available constraints. This model is the basis for the geometries and densities of the different parts of the dynamic numerical models (Section 4.1). The used densities are summarized in Table 4.1.

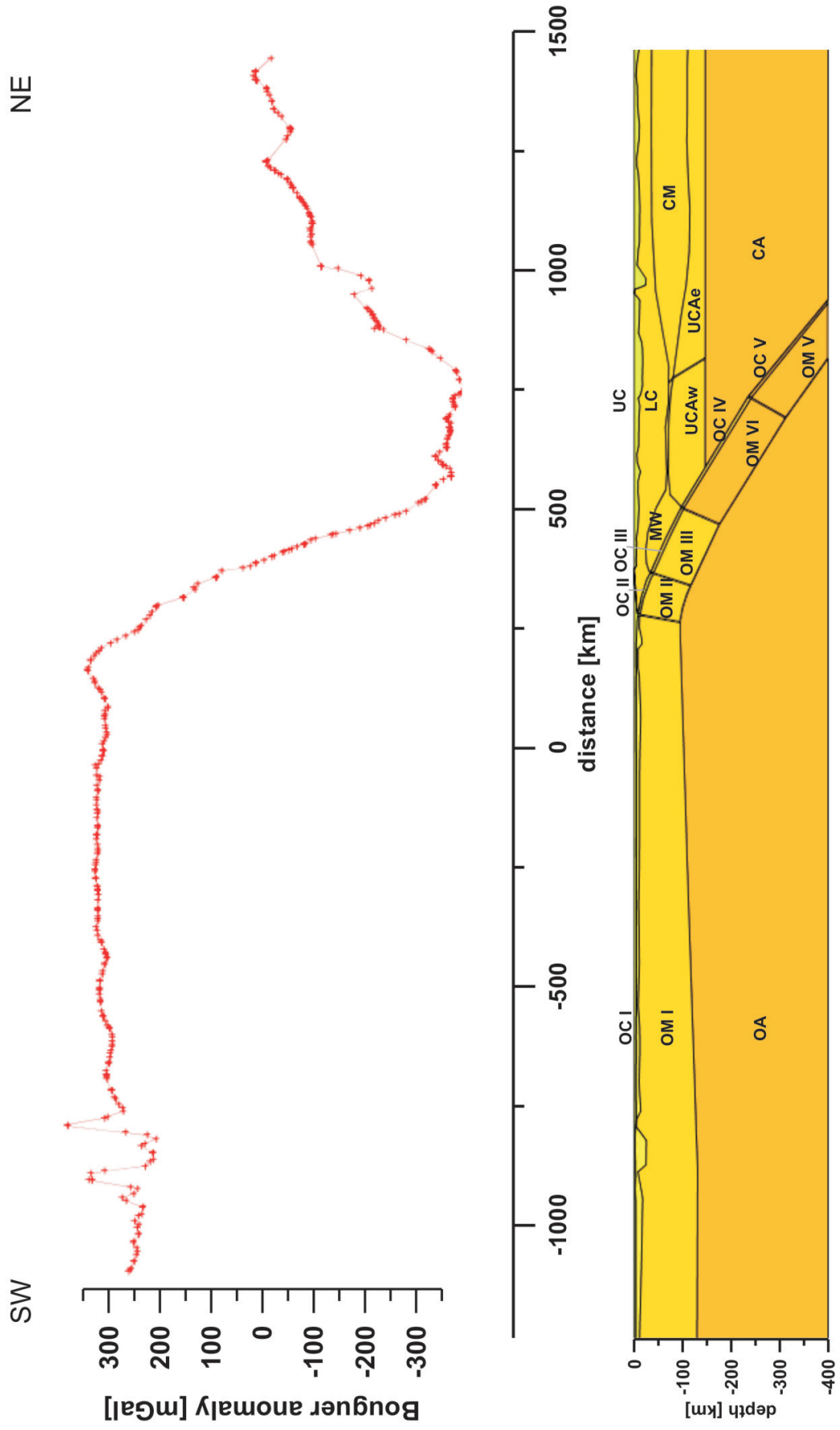

Figure 2.3: Vertical cross section (white line in Figure 2.2) with different units (after *Tassara et al.*, 2006). For abbreviations of the unit names refer to text and Table 4.1

2.3 The seismic profile

To calculate the Young's moduli for the models, density and seismic velocities are needed (Equation 3.16). A seismic velocity model is provided by the "Andean Continental Research Project 1996" (ANCORP). The ANCORP profile is a 400 km long seismic wide-angle reflection profile crossing the Central Andes at 21°S (*ANCORP Working Group*, 2003). It is the onshore continuation of the offshore reflection profile by the "Crustal Investigations off- and on-shore Nazca/Central Andes project 1995" (CINCA95) (*Patzwahl et al.*, 1999). A combined interpretation of the profiles merged with wide-angle and receiver function results of *Yuan et al.* (2000) is shown in Figure 2.4. From this model the seismic v_p velocities were taken to calculate the Young's moduli for several parts of the numerical models (Section 4.2.5). For the oceanic crust (OC) I used v_p velocities from 6.2 to 6.5 km/s. The oceanic lithospheric mantle (OM) is described by 8.1 km/s. In the continental crust v_p varies between 3.6 km/s and 6.4 km/s. Because of the resolution of the numerical models it is impossible to model every detailed structure with different seismic velocities. Therefore, an average velocity for the different model parts were chosen. I decided for a velocity of 5.9 km/s for the upper crust (UC) and 6.3 km/s for the lower crust (LC). For the continental lithospheric mantle values of 6.4 km/s (MW) and 7 km/s (CM) were chosen. The upper continental asthenosphere is characterized by 7.7 km/s (UCAw) and 8.1 km/s (UCAe). The velocity model is only 100 km deep and provides no velocities for the deeper asthenosphere. Therefore, I assume a velocity of 8.5 km/s for the deeper continental and oceanic asthenosphere. The seismic velocities chosen for the different parts of the models together with the corresponding densities and Young's moduli are shown in Table 4.1 in Section 4.2.5.

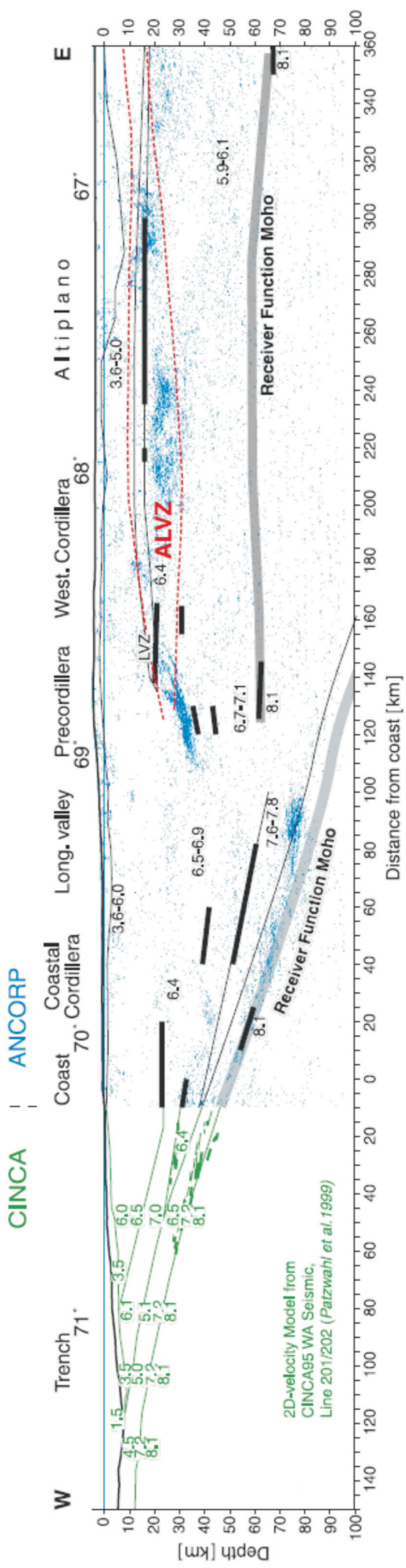

Figure 2.4: Seismic v_p velocity model of the CINCA (*Patzwahl et al.*, 1999) and ANCORP profile at 21°S including onshore wide-angle and receiver function results from *Yuan et al.* (2000) (*ANCORP Working Group*, 2003). ALVZ marks the Andean Low Velocity Zone.

2.4 GPS measurements and strain rates

Current deformation rates of the Central Andes can be observed by GPS data. Even though the time scale of GPS time series (years) differ significantly from the running time of the numerical models (100 000 years), it is one possibility to compare modelled results with observed data. The direct comparison between both, like in *Kellner* (2007) and here in this work should be made with care. The GPS data considered in this work are from the South America-Nazca Plate Project(SNAPP) and the central Andes GPS project (CAP) (*Kendrick et al.*, 2001). Figure 2.5 shows the velocity vectors between 16°S

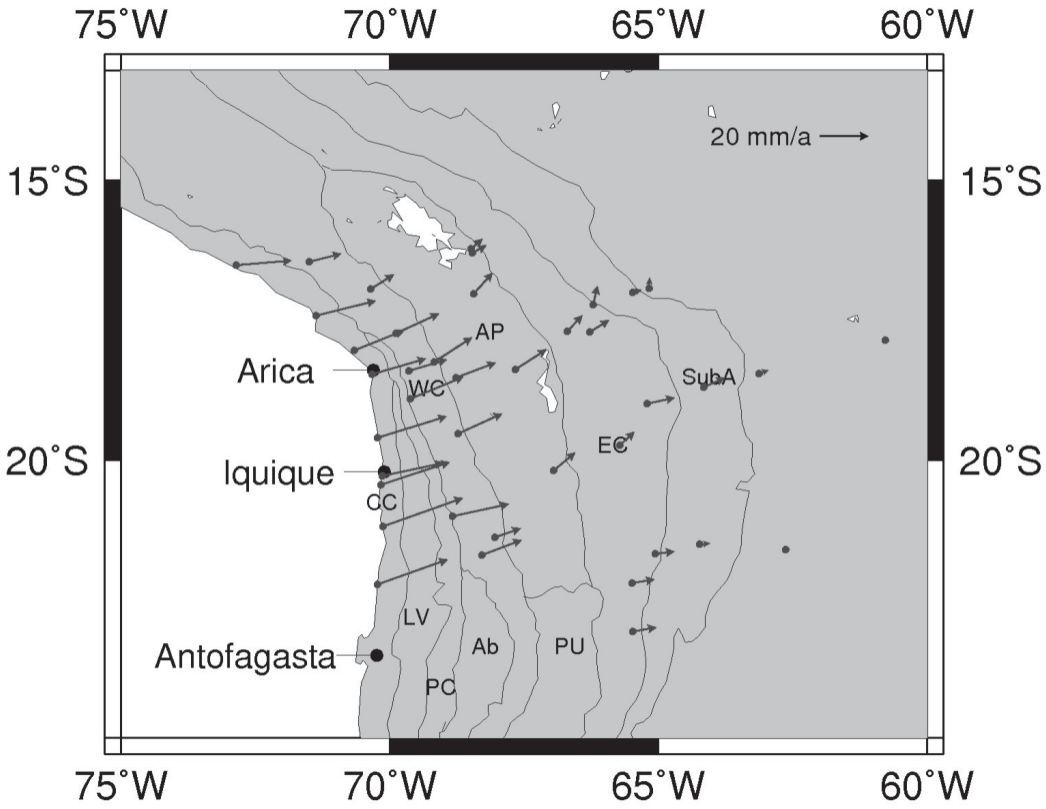

Figure 2.5: GPS vectors for the central Andes (*Kendrick et al.*, 2001): Black lines denote the morphotectonic units as in Figure 2.1.

and 22°S. For a closer explanation of the GPS data refer to *Kendrick et al.* (2001). The GPS data are given relative to the stable core of the South American plate (*Kendrick et al.*, 2001). In the numerical models both plates are moving (Section 4.2.2). Therefore, the applied velocity of the South American plate (-2.8 cm/a) was subtracted from the model results to make the results comparable to the GPS data. The east and north component of the GPS velocities are compared to the modelled results. Comparing the modelled strain rates with strain rates estimated from geological observations is another possibility to check the modelling results. *Hindle et al.* (2002) estimated recent strain

rates for the Subandean region in the Central Andes (Table 2.1) from GPS measurements and geological observations. For the estimation from geological observations the authors consider one time the last 10 Ma and one time the last 25 Ma. At 20°S the recent strain rate estimated from GPS and the recent strain rate estimated by geological observations considering the last 10 Ma are nearly equal whereas the recent strain rate estimated from geological observations considering the last 25 Ma are by the factor 2 smaller.

Table 2.1: Principal strain rates and azimuths in the Subandean region estimated from GPS and geological observations (*Hindle et al.*, 2002).

		μstrain/a	azimuth [°]
17°	GPS	-0.063	53
	geological 10 Ma	-0.041	53
	geological 25 Ma	-0.021	58
20°	GPS	-0.038	83
	geological 10 Ma	-0.041	83
	geological 25 Ma	-0.022	88

2.5 Forces driving and resisting subduction

The effect of forces driving plate motions are still not fully understood (*Wessel and Müller*, 2009). There are two classes of forces important for subduction, which are the driving and the resisting forces. Driving forces are the ridge push from the mid-ocean ridges and the slab pull, which originates from the negative buoyancy of the subducting cold dense oceanic lithosphere (*Wessel and Müller*, 2009). Further the phase transition from olivine to spinel at a depth of about 410 km results in a negative buoyancy force (*Billen*, 2008). Resisting forces include the bending of the lithosphere, frictional coupling between slab and overriding plate and the viscous shear in the mantle. The phase transition from spinel to perovskite and magnesiowustite results in a positive buoyancy force and therefore hinder the subduction (*Billen*, 2008).

The relative importance of these forces is still a matter of debate (e.g. *Wessel and Müller*, 2009; *Mahatsente et al.*, 2012). Generally, the negative thermal buoyancy of subducting slabs (slab pull) is thought to be about one order of magnitude larger than ridge push once subduction becomes self-sustaining, but since it is locally balanced by the viscous resistance of the mantle, its effective contribution may be of the same order as the ridge push (e.g. *Forsyth and Uyeda*, 1975; *Lithgow-Bertelloni and Richards*, 1998; *Mahatsente et al.*, 2012)

Forsyth and Uyeda (1975) consider the slab pull as the major force with a potential energy stored in the descending slab of one order higher than any other force acting on plate. Other authors suggest that the force on the plate from subduction is equal or less than other forces driving the plate movement mentioned above. (*Sandiford et al.*, 1995). *Schellart* (2004) propose that slab pull is twice as high as ridge push. The effect of slab pull on the model results is described in Section 5.3.

3 Theoretical background

3.1 Physical equations

Deformation and flow of earth materials are of primary importance in many branches of earth science, from seismology to plate tectonics (*Ranalli*, 1995). Different rehological behaviour play a role in geodynamics. One one side viscosity is important in the mantle even for short time scales of 1000 of years, whereas the lithosphere can be considered as elastic on time scales in the range of millions of years. On the other side plasticity in the crust play a role for material failure in the crust which is important for faulting, earthquakes, and folding. In this work the importance of different rheology parameters is investigated. Therefore, a short overview over the physical background of rheology and conservation equations is given in this section. For further explanations refer e.g. *Ranalli* (1995), *Kennett and Bunge* (2008) or *Turcotte and Schubert* (2002).

3.1.1 Equations of equilibrium

To be in equilibrium the resultant component of force in any coordinate direction must be zero. Therefore the condition of equilibrium in general case is

$$\frac{\partial \sigma_{ij}}{\partial x_j} + \rho X_i = 0 \tag{3.1}$$

where σ_{ij} is the stress tensor, ρ is the density, and X_i is the body force. If g is the acceleration of gravity and the x_3 axis is vertical and pointing upwards then the components of X_i are $X_3 = -g$, $X_1 = X_2 = 0$ and we get the equations of equilibrium

$$\frac{\partial \sigma_{11}}{\partial x_1} + \frac{\partial \sigma_{21}}{\partial x_2} + \frac{\partial \sigma_{31}}{\partial x_3} = 0 \tag{3.2}$$

$$\frac{\partial \sigma_{12}}{\partial x_1} + \frac{\partial \sigma_{22}}{\partial x_2} + \frac{\partial \sigma_{32}}{\partial x_3} = 0 \tag{3.3}$$

$$\frac{\partial \sigma_{13}}{\partial x_1} + \frac{\partial \sigma_{23}}{\partial x_2} + \frac{\partial \sigma_{33}}{\partial x_3} = g\rho. \tag{3.4}$$

3.1.2 Conservation equations

In non-relativistic mechanics either mass, momentum, or energy can be lost, which leads to the fundamental conversation equations in the most general form

$$\frac{\partial M}{\partial t} = 0 \tag{3.5}$$

$$\frac{\partial P}{\partial t} = 0 \tag{3.6}$$

$$\frac{\partial U}{\partial t} = 0 \tag{3.7}$$

where M is the mass, P is the momentum and U is the energy. The conversation of mass (3.5) can be described by the continuity equation which relates the velocity $\vec{v}$ to the density ρ

$$\frac{\partial \rho}{\partial t} + \frac{\partial}{\partial x_i}(\rho v_i) = 0. \tag{3.8}$$

Introducing the total derivative expression

$$\frac{D}{Dt} = \frac{\partial}{\partial t} + v_j \frac{\partial}{\partial x_j} \tag{3.9}$$

Equation 3.8 becomes

$$\frac{D\rho}{Dt} + \rho \frac{\partial v_i}{\partial x_i} = 0. \tag{3.10}$$

The acceleration of a continuum due to the acting forces can be described in terms of velocity as

$$\frac{Dv_i}{Dt} = \frac{\partial \sigma_{ij}}{\partial x_i} + g_i \tag{3.11}$$

which represents a form for conservation of momentum (*Kennett and Bunge*, 2008) and is called equation of motion. σ_{ij} is related to the strain over the relevant constitutive equation for the rheological behaviour (Sections 3.1.3 and 3.1.4). The conversation of energy is mainly regarded to thermal effects and it can be described after *Kennett and Bunge* (2008) as

$$\rho \frac{DU}{Dt} = h + \frac{\partial}{\partial \mathbf{x}}(k \frac{\partial T}{\partial \mathbf{x}}) + \sigma_{ij} \frac{\partial v_j}{\partial x_i} \tag{3.12}$$

with U as inertial energy per unit mass, h as internal heat generation (e.g. radioactive processes in the earth), k as thermal conductivity of the material and T as temperature. But temperature is not considered in the models of this work (Section 4.2.6) and therefore

Equation 3.12 is not solved in the modelling process.

3.1.3 Elasticity

Applying a load to a deformable body leads to stresses and strains. In an elastic body the stress is linear proportional to the strain and the latter is fully reversible when the load is removed. Figure 3.1 show the strain-stress diagram and the strain-time diagram for an elastic behaviour.

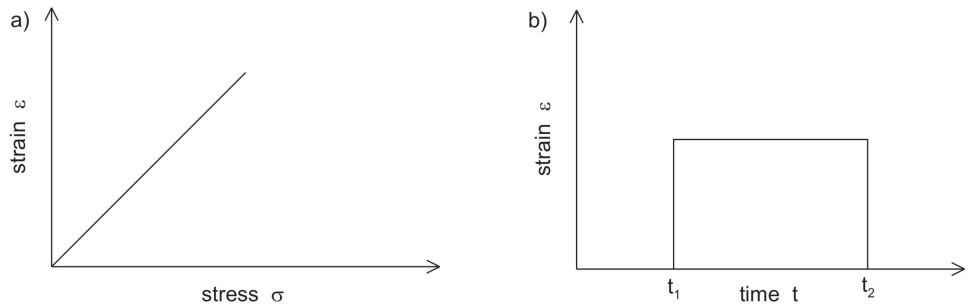

Figure 3.1: Strain-stress (a) and strain-time (b) diagram for an elastic body: Loading starts at time t_1 and strain is completely reversible after loading ends at time t_2 (after *Ranalli*, 1995).

Elasticity is described by Hooke's law. The most general form is

$$\sigma_{ij} = C_{ijkl}\epsilon_{kl} \tag{3.13}$$

with the elastic parameters consisting of a set of 81 coefficients represented by C_{ijkl}, but only 36 parameters are independent due to symmetric behaviour of the tensors. σ and ϵ are the stress and strain tensor. For a homogeneous, isotropic continuum where the elastic behaviour is independent from direction the elasticity can be described by only two independent elastic parameters and the Hooke's law becomes the constitutive equation

$$\sigma_{ij} = \lambda\epsilon_{ii}\delta_{ij} + 2\mu\epsilon_{ij} \tag{3.14}$$

where δ_{ij} is the Kronecker delta ($\delta_{ij} = 1$ for $i = j$, $\delta_{ij} = 0$ for $i \neq j$) and λ and G are the Lamé's parameters. Other common elastic parameters are the Young's modulus E and the Poisson's ratio ν which can be expressed by Lamé's parameters

$$E = \frac{\mu(3\lambda + 2\mu)}{\lambda + \mu}; \qquad \nu = \frac{\lambda}{2(\lambda + \mu)}. \tag{3.15}$$

The Young's modulus and Poisson's ratio can be determined by the density ρ and the seismic velocities v_p and v_s

$$\nu = \frac{v_p^2 - 2v_s^2}{2(v_p^2 - v_s^2)}; \qquad E = \rho v_s^2 \left(\frac{3v_p^2 - 4v_s^2}{v_p^2 - v_s^2} \right). \tag{3.16}$$

For most rocks in the crust E is in the range of 50 to 100 GPa (*Eisbacher*, 1996). Equation 3.14 shows, that the stress and strain relationship is linear. Strain depends on the acting load but not on the duration of loading. If the load vanishes then the strain is fully recoverable and the elastic body takes the same shape as before the loading. Elastic rheology is strain-rate independent.

3.1.4 Viscosity

Viscosity describes the creep characteristics of a material. In contrast to elastic behaviour the deformation for a viscous body is permanent and irreversible when loading ends (Figure 3.2). Viscous behaviour (ductil behaviour) is strain independent but the stress is a function of the strain-rate. When the stress-strain rate dependence is linear one speaks of Newtonian viscous deformation and when the dependence is non-linear it is called Non-Newtonian viscous (*Burov*, 2009). The stress-strain rate relation has the form of

$$\dot{\epsilon} = A\sigma^n \tag{3.17}$$

with $\dot{\epsilon} = \frac{\partial \epsilon}{\partial t}$. A is in general a function of temperature, pressure and material parameters, whereas n is a constant with $n = 1$ for Newtonian viscous and $n \neq 1$ for Non-Newtonian viscous behaviour. A linear viscous body can be described after *Ranalli* (1995) as

$$\sigma = 2\eta\dot{\epsilon}. \tag{3.18}$$

Substitute $\dot{\epsilon}$ in Equation 3.17 by Equation 3.18 results in

$$A = \frac{1}{2\eta}. \tag{3.19}$$

For Newtonian bodies the viscosity is independent from stress (Equation 3.19) but it is a function of stress for non-Newtonian rheologies. In the earth there are mainly two types of creep. The diffusion creep is linear Newtonian and dominates for high temperature and low stress conditions. For moderate temperatures and high stress the dislocation creep (Power law creep) with n=3 to 3.5 dominates. Figure 3.2 shows the stress strain-rate diagrams for Newtonian and Power law ($n = 3.5$) creep.

Another important equation for describing viscous bodies is the Navier-Stokes equation,

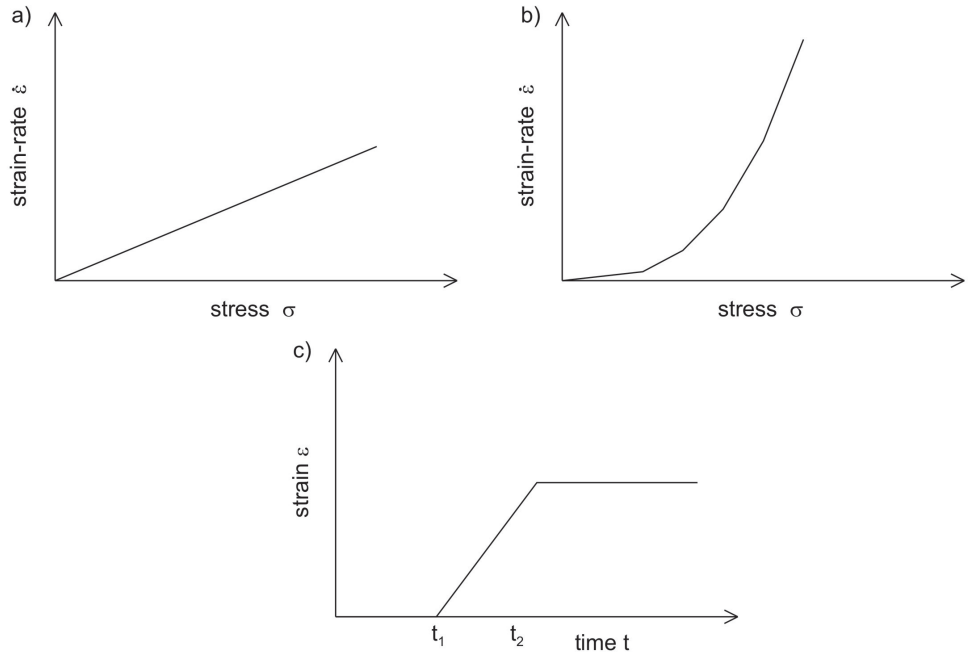

Figure 3.2: a) Stress-strain rate diagram for a linear viscous body. The slope is related to viscosity as $1/2\eta$. b) Stress-strain rate diagram for a non-Newtonian behaviour (Power law creep) with $n = 3.5$. c) Strain-time diagram, loading starts at t_1 and the strain remains after loading ends at t_2 (after *Ranalli*, 1995).

which is the conservation of momentum subject to conservation of mass (*Billen*, 2008). Assuming a Stokes fluid the stress σ is related to the velocity v of the fluid by

$$\sigma_{ij} = -p\delta_{ij} + \eta(\frac{\partial v_j}{\partial x_i} + \frac{\partial v_i}{\partial x_j}) - \frac{2}{3}\eta\delta_{ij}\frac{\partial v_k}{\partial x_k} \tag{3.20}$$

where p is the hydrostatic pressure and η the viscosity. Combining the constitutive equation of the fluid (3.20) with the equation of motion (Equation 3.11) we require

$$-\frac{\partial p}{\partial x_j} + \frac{\partial}{\partial x_i}\left[\eta(\frac{\partial v_j}{\partial x_i} + \frac{\partial v_i}{\partial x_j}) - \frac{2}{3}\eta\delta_{ij}\frac{\partial v_k}{\partial x_k}\right] + \rho g_i = \rho\frac{Dv_j}{Dt}. \tag{3.21}$$

If viscosity is constant than (3.21) can be expressed as

$$-\frac{\partial p}{\partial x_j} + \eta\frac{\partial^2 v_j}{\partial x_i \partial x_i} + \frac{1}{3}\eta\frac{\partial^2 v_k}{\partial x_j \partial x_k} + \rho g_i = \rho\frac{Dv_j}{Dt}. \tag{3.22}$$

which is the equation of motion or Navier-Stokes equation for a fluid with Newtonian viscosity. For an incompressible fluid the 3rd term on the left site vanishes and if the material acceleration is negligible the right site becomes 0.

3.1.5 Viscoelasticity

Often bodies are neither totally elastic nor totally viscous. There are various constitutive models to combine elastic and viscous behaviour. Here only the Maxwell model is described, for other models like Kelvin or Burgers see *Ranalli* (1995) or *Kennett and Bunge* (2008). All of these models are combinations of elastic Hooke elements, represented by a spring, and viscous Newton elements, realized by a dashpot. To describe a viscoelastic (elasticoviscous) body one spring and one dashpot are combined in series (Maxwell body). The relationship between stress and strain for an elastic body is e.g. for shear components given by

$$\sigma = 2\mu\epsilon \tag{3.23}$$

where μ is the rigidity or shear modulus $\mu = E/(2 + 2\nu)$. A linear viscous body can be described by Equation 3.18 as

$$\sigma = 2\eta\dot{\epsilon}. \tag{3.24}$$

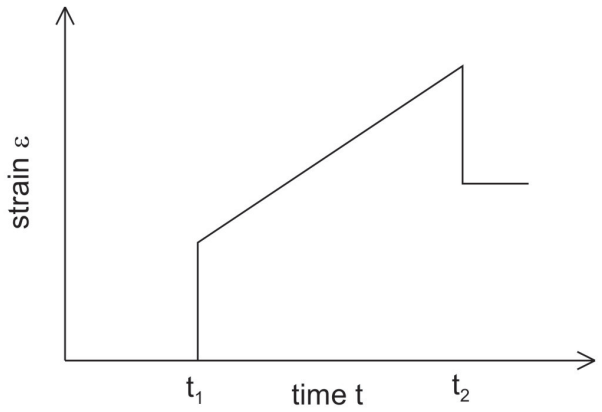

Figure 3.3: Stress-strain rate diagram for a viscoelastic or Maxwell body: Loading starts at t_1 and ends at t_2; only the elastic part of strain is recoverable (after *Ranalli*, 1995).

The total strain ϵ^t for a Maxwell body is the sum of the elastic strain ϵ^e and the viscous strain ϵ^v

$$\epsilon^t = \epsilon^e + \epsilon^v = \frac{\sigma}{2\mu} + \frac{\sigma}{2\eta}t. \tag{3.25}$$

Expressed in terms of strain rates the constitutive equation for a Maxwell body is

$$\dot{\epsilon}^t = \frac{\dot{\sigma}}{2\mu} + \frac{\sigma}{2\eta}. \tag{3.26}$$

The strain time diagram for a Maxwell body is shown in Figure 3.3. At the beginning the behaviour is elastic and later the reaction is viscous. After the load ends only the elastic strain is recoverable. The maxwell relaxation time τ_M (Equation 3.27) defined as

$$\tau_M = \frac{\eta}{\mu} \tag{3.27}$$

determines the relation between elastic and viscous behaviour. For $t < \tau_M$ elasticity dominates, for $t > \tau_M$ viscous creep is dominant.

3.1.6 Plasticity

Linear elastic behaviour as discussed in Section 3.1.3 occurs only below a critical stress. Above this stress deformation is at first non-linear and the material fails when the deviatoric stress (Equation 3.30) reaches a maximum value called yield stress or yield strengths σ_y. The value of σ_y depends on material, temperature, pressure, chemical environment, and conditions of loading (*Ranalli*, 1995). Plastic deformations are irreversible. There are two possibilities how a material can fail after reaching σ_y. First it can fail by fracture (brittle behaviour) with very little or no permanent deformation. In this case the stress drops to zero when σ_y is reached (Figure 3.4 a). The second possibility of failure is plastic flow (ductile behaviour). In plastic flow the stress is ideally constant after σ_y is reached (Figure 3.4 b). However, strain (or work) hardening is possible, where yield stress increases with increasing deformation. The opposite behaviour is called strain softening. If a material fails by fracture or by plastic flow depends on the fracture stress and the yield stress. Both depend on temperature and pressure, but pressure affects more the fracture stress, whereas the effect of temperature is much stronger on the yield stress (*Ranalli*, 1995). If the fracture stress is lower than the yield stress (at low pressure and temperature) failure will be brittle, and if fracture stress is higher than yield stress (at high pressure and temperature) failure will be ductil (*Ranalli*, 1995).

Fracture and plastic flow play an important role in the mechanics of the upper lithosphere. It is linked to earthquakes, faulting and folding. The depth of the transition between brittle and ductile behaviour has an important bearing on the depth distribution of earthquakes. Nearly all seismicity occurs in the brittle regime (*Ranalli*, 1995), and it is a consequence of fast slip of the two sides of a new or preexisting fault plane. Slow slip will not cause earthquakes. To generate an earthquake, dynamic instabilities must occur, with consequent fast slip, stress drop, and release of energy in form of seismic waves

(*Ranalli*, 1995).

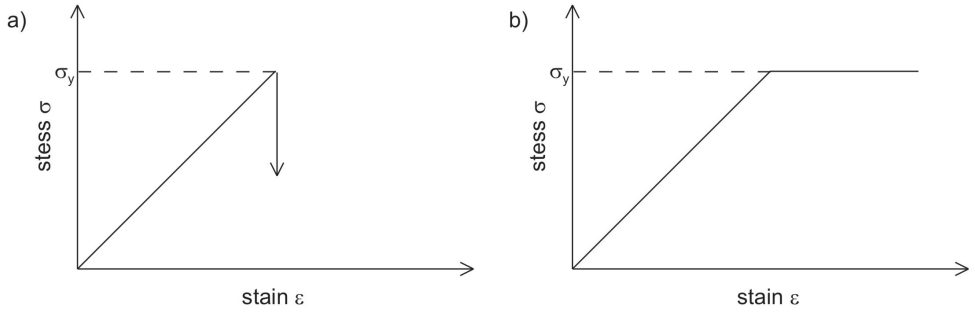

Figure 3.4: Stress-strain rate diagram for a plastic behaviour: a) Brittle failure where stress drops in theory to zero (denote by the downward arrow) when the yield strength (σ_y) is reached. b) In perfect ductile (or plastic) flow, stress is ideally constant with increasing strain (after *Ranalli*, 1995).

Plasticity can be characterized by the yield function F and is expressed in a perfectly rigid-plastic body by:

$$F = \sigma - \sigma_y = 0. \tag{3.28}$$

This means plastic deformation occurs when $\sigma = \sigma_y$ (Figure 3.4 b). The most common yield criteria used for the plastic deformation in the crust are the Mohr-Coulomb and the Drucker-Prager criterion. In numerical modelling often the Drucker-Prager approach is used (e.g. *Kellner*, 2007; *Babeyko and Sobolev*, 2008), which is based on the work of *Drucker and Prager* (1952) and uses a smoothed yield condition. Therefore, it can be handled numerically more easy (e.g. *Zienkiewicz et al.*, 2005). In this work Drucker-Prager plasticity is applied to the upper continental crust in models discussed in Section 5.6.

The yield function F_{DP} for the Drucker-Prager yield criterion is

$$F_{DP} = \frac{-2sin\phi}{\sqrt{3}(3 + sin\phi)} I_1 + \sqrt{J_2} - \frac{6Ccos\phi}{\sqrt{3}(3 + sin\phi)} = 0 \tag{3.29}$$

where ϕ is the angle of internal friction, C is the cohesion, and I_1 is the first invariant of the stress tensor ($I_1 = \sigma_{xx} + \sigma_{yy} + \sigma_{zz}$). J_2 is the second invariant of the deviatoric stress tensor S_{ij}. S_{ij} can be obtained by subtracting the hydrostatic stress tensor (second term in Equation 3.30) from the stress tensor (σ_{ij}):

$$S_{ij} = \sigma_{ij} - \frac{1}{3}\sigma_{kk}\delta_{ij} \tag{3.30}$$

$$J_2 = \frac{1}{2} s_{ij} s_{ij} = \frac{1}{6} \left[(\sigma_{xx} - \sigma_{yy})^2 + (\sigma_{yy} - \sigma_{zz})^2 + (\sigma_{zz} - \sigma_{xx})^2 \right] + \sigma_{xy}^2 + \sigma_{yz}^2 + \sigma_{zx}^2. \quad (3.31)$$

Besides ϕ and C there is a third parameter describing plasticity, the dilatation angle ψ. This angle accounts for dilatation in shear that occurs due to sliding over interface asperities (*Burov*, 2009). After *Vermeer and de Borst* (1984) dilatancy can be described as the change in volume that is associated with shear distortion of an element in the material. When $\psi = \phi$ plasticity is associative and it is nonassociative when $\psi \neq \phi$. Most rocks are nonassociative with $\phi = 30° - 40°$ and $\psi < 10°$ (*Vermeer and de Borst*, 1984).

3.2 Finite Element Method (FEM)

To solve the system of equation for every point in the models numerical methods are necessary. There exist different numerical methods to solve complex problems and provide quantitative results. Most popular are the Finite Difference Method (FDM), Discrete Element Method (DEM), and the Finite Element Method (FEM). The latter is used for this work and a short explanation is given here. For further details see e.g. *Zienkiewicz et al.* (2005). One advantage of the FEM is the ability to handle complex geometries and to implement complex boundary conditions and contacts between surfaces.

The FEM is established for complex engineer and physical problems as well as geodynamic modelling. The basis idea is division (discretization) of a complex continuum into a finite number of smaller parts, the finite elements. The elements can vary in size and shape and have several nodes located at the corners, at the edges and/or within the element depending on the element type. Neighbouring elements share their nodes, when no contact definition is applied between the elements. For solving the equation system boundary conditions at the model edges have to be specified.

Every element has a shape function N_k which defines the value of functions inside an element by using the values at their nodes. One unknown function F inside an element has the form

$$F(x) = \sum_{k=1}^{n} N_k(x) F_k. \quad (3.32)$$

with N_k is the shape function, n is the number of nodes and F_k are the values of F at the nodes. Combining all elements of the model and boundary conditions into one system of equation leads to a solution of the entire field of unknown functions. The computational time needed for a model solution depends mainly on the number of nodes. More nodes

increases the accuracy of the solution but, it increases the degree of freedom also which results in a longer computational time. Therefore, the user has to find a compromise between the accuracy of the solution and the computational time. Generating the "right" mesh (set of all elements) is therefore the most important task for Finite Element modelling. For further details of the method see e.g. *Zienkiewicz et al.* (2005).

In geodynamics the method has been applied for investigating fluid migration (e.g. *Kurz et al.*, 2004; *Jahr et al.*, 2008), slab dynamics (e.g. *Liu et al.*, 2002; *Babeyko et al.*, 2006), crustal deformation (e.g. *Heidbach and Drewes*, 2003; *Buiter et al.*, 2006; *Fischer*, 2006; *Hampel and Pfiffner*, 2006; *Gebauer et al.*, 2010), fore-arc deformation (e.g. *Kellner*, 2007), thermal models (e.g. *Springer*, 1999), mantle convection (e.g. *Bunge*, 2005), faulting and seismic cycles (e.g. *Nüchter and Ellis*, 2010).

3.2.1 HyperMesh

For developing the model geometry and creating the according mesh HyperMesh, belonging to the commercial software package HyperWorks by Altair Engineering GmbH (*Hyperworks version 11*, 2011), was used. HyperMesh is a software to create FE models. It provides different linear and quadratic element types in 2D and 3D for meshing. Single nodes, e.g. a topography grid, can be imported into the model. It is also possible to define contacts, materials or boundary conditions, but in this work HyperMesh is used for mesh generation only. The meshed model can be written in an output file with the coordinates of all nodes and the element definition and all other parameters which have been specified before. Because HyperMesh is compatible with several FE solvers (e.g. Ansis, Comsol, ABAQUS, etc.) the solver type needs to be specified to get the correct output format. For presenting the results HyperView of the HyperWorks package was used.

3.2.2 ABAQUS

In this work the ABAQUS software from Simulia (*ABAQUS tutorial version 6.10*, 2010) is used for defining model parameters and solution of the equations. ABAQUS is commercial software for finite element modelling. It provides various element types for mesh generation and several possibilities to implement different rheologies like elasticity, different types of plasticity (Mohr-Coulomb, Drucker-Prager, etc.), different types of viscosity (linear, power law, etc.) or combinations. Further, several boundary condition types (velocity, displacement, etc.), forces (gravity, etc.), or contact formulation (surface to surface, node to surface, hard contact, etc.) can be applied to the model. Initial conditions like initial stress can be specified at the beginning of the model. It is possible to choose the increment size (time steps) for calculation and to specify at which time steps the results should be reported. Stress, strain, displacement or energy are only some output possibil-

ities offered by ABAQUS.

Every part of the model is defined by a material. The basic rheology is elasticity and the material is described by density, Young's modulus and Poisson's ratio. Therefore, at least these parameters must be known to define a plain rheological behaviour for the model. Young's modulus and Poisson's ratio can be calculated from density and seismic velocities (Equation 3.16) provided by a given density model (Section 2.2) and a seismic velocity model (Section 2.3).

For viscous behaviour the creep formulation of ABAQUS was used described by Equation 3.17. For a Newtonian material the relation between the pre-exponential factor A and the viscosity η is normally described by Equation 3.19. However, ABAQUS works internally with the von Mises equivalent stress q and the equivalent creep strain rate $\dot{\epsilon}^{cr}$ (*ABAQUS tutorial version 6.10*, 2010)

$$q = \sqrt{\frac{3}{2} S_{ij} S_{ij}} \tag{3.33}$$

$$\dot{\epsilon}^{cr} = \sqrt{\frac{2}{3} \dot{\epsilon}^{cr}_{ij} \dot{\epsilon}^{cr}_{ij}}. \tag{3.34}$$

$\dot{\epsilon}^{cr}_{ij}$ are the components of the creep strain rate tensor and S_{ij} are the components of the deviatoric stress tensor (Equation 3.30).

Therefore, ABAQUS works with the equivalent pre-exponential factor A' and this is related to A as

$$A' = \frac{2}{3} A \tag{3.35}$$

(*Steffen 2012, pers. communication*). Combining this with Equation 3.19 the equivalent pre-exponential factor in ABAQUS is really

$$A' = \frac{1}{3} \eta. \tag{3.36}$$

For numerical reason A' should not be smaller than $1e^{-27}$ (*ABAQUS tutorial version 6.10*, 2010). Smaller values can lead to convergence problems.

In this work the stress results are expressed as the von Mises equivalent stress q defined by Equation 3.33. It is a combination from all stress components

$$q = \sqrt{\frac{1}{2}[(\sigma_{11} - \sigma_{22})^2 + (\sigma_{22} - \sigma_{33})^2 + (\sigma_{33} - \sigma_{11})^2 + 6(\sigma_{12}^2 - \sigma_{23}^2 + \sigma_{31}^2)]}. \tag{3.37}$$

For contacts the surface to surface hard contact definition of ABAQUS is used. Every contact consists of a master surface and a slave surface. Master and slave surfaces are defined by the user. Sometimes the two surfaces fit not exactly to each other and there are overlappings and/or gaps between the two surfaces at the beginning of modelling process (Figure 3.5). To avoid stress artefacts due to such imprecise contact definition the position of slave nodes lying not at the master surface has to be modified to match the contact zone at the start of modelling. However, the master surface remaines unchanged. All slave nodes within a defined position tolerance which do not fit the master surface are displaced stress free to the master suface. After this correction all slave nodes are positioned on the master surface and the modelling process can start.

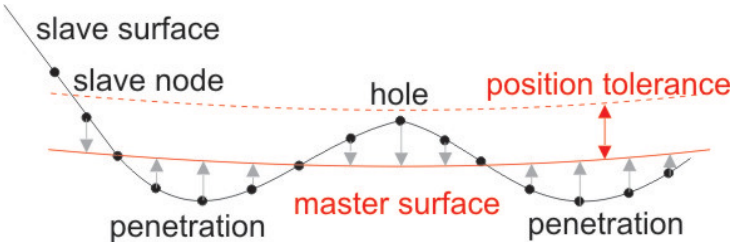

Figure 3.5: Slave nodes penetrating the master surface or lying within position tolerance are displaced to the master surface at the beginning of modelling.

Most of the models used here are computed for 100 000 years. To see the evolution of modelling results with time the output was reported every 5000 years. An output at more time steps will lead to smaller modelling time steps which will increase computational time. The output variables used in this work are the components of displacement (U), the total strain (LE), the elastic strain (EE), the viscous strain (VE) and the stress (S). In literature the strain and stress is often given as principal strain (stress) and principal axes. In two dimensions the principal strains and axes can be calculated as follows (*Turcotte and Schubert*, 2002):

$$\epsilon_{1,2} = 0.5(\epsilon_{11} + \epsilon_{22}) \pm \sqrt{0.25(\epsilon_{11}^2 - \epsilon_{22}^2) + \epsilon_{12}^2}. \tag{3.38}$$

One principal axis can be calculated by

$$tan(2\theta) = \frac{2\epsilon_{12}}{\epsilon_{11} - \epsilon_{22}} \tag{3.39}$$

and the second axis is perpendicular ($\theta_2 = \theta_1 + 90°$). These equations are used when the horizontal strain is considered only and the vertical component is neglected. This is

useful to compare the modelled strain rates with strain rates estimated from GPS data or geological observation.

4 Numerical modelling

In this chapter the set up of the numerical models is presented. But, first the model type has to be explained. After *Billen* (2008) the forces driving and resisting subduction have to be balanced at any instant in time, which is expressed by the Navier-Stokes equation (Equation 3.22). With density and viscosity defined for every part of the model and described boundary conditions the velocity field and pressure required to balance the forces can be calculated. The structure of the slab is predetermined. *Billen* (2008) calls such model types instantaneous models. Coupling the conversation of energy with the Navier-Stokes equation results in time dependent models, where the thermal structure is varied with time owing to conduction and advection of heat and internal heat generation. There are two types of time dependent models, the fully dynamic models of subduction have no prescribed velocities or force boundary conditions and only the buoyancy force can drive flow (*Billen*, 2008). However, often kinematic boundary conditions are used to define the direction and rate of plate motion.

In the models developed here no temperature field is considered and boundary conditions are kinematic, therefore after *Billen* (2008) the models belong to the instantaneous model type. The rheological parameters are time independent but for the viscoelastic parts elasticity dominates at the beginning of the model (model time $<$ Maxwell time) and later viscosity plays an important role (model time $>$ Maxwell time). Therefore, time controls the results and the models can be regarded as partially dynamical models. The models run for 100 000 years which needs 10 to 15 hours computational time. To investigate the evolution the results were reported every 5000 years. Smaller reporting intervals will increase the computational time. A timespan of 100 000 years is short compared to the timespan of subduction and orogenesis. Therefore, the modelled results can be considered as recent and compared with recent observations.

It is important that all model parameters have the same units. Here the SI unit system is used. However, for a better understanding and comparison with observed data it is often necessary to use other units in the text. For example a plate velocity of 2.8 cm/a is a velocity of $8.89e^{-10}$ m/s, with a year of $3.15e^{7}$ seconds. The x-axis points in east direction, the y-axis corresponds to the north direction and the upward pointing z-axis is the vertical direction. The density model has UTM coordinates with zone 19 (meridian

$69°W$) as reference and therefore the FE-model has the same coordinates.

4.1 From static density model to finite element modelling

Density models based on gravity measurements are static. They show one possible density distribution in the underground fitting the instantaneous observed Bouguer anomaly. In order to take into account the future time, numerical modelling is one possibility. The geometry of the density model should be the basis for the structure of the dynamic models and must therefore be transferred. The density model was developed with the program IGMAS and later transfered to the IGMAS+ format. IGMAS+ is a redesigned version of IGMAS according to modern software architecture for optimal man machine communication and grid computing features (*Alvers et al.*, 2010). An advantage of IGMAS+ is the interoperability to widely used existing software like GOCAD and Geosoft. For further information about IGMAS and IGMAS+ see (*Götze and Lahmeyer*, 1988; *Schmidt and Götze*, 1998; *Alvers et al.*, 2010; *Schmidt et al.*, 2010). The IGMAS+ output contains the coordinates for every node. The nodes belonging to one special unit are given as a polygonal line for every cross section and the triangulation between the cross section nodes is denoted for every unit. With a newly developed program the IGMAS+ output is transferred into an input for HyperMesh. The input file contains a coordinate block and an 2D element block in the form:

*Node
node number, x, y, z
node number, x, y, z
...
*ELEMENT, TYPE = S3, ELSET = unit name
element number, node1, node2, node3
element number, node1, node2, node3
...

The two dimensional (2D) elements are identical with the triangulation elements of IGMAS+. The program creates an import file for every polyeder and a file with all units. After importing this file in HyperMesh surfaces from the 2D elements were created and the geometry was changed slightly where it was necessary because of to steep angles. To include topography an additional surface was created from a topography grid (Section 4.2.1). Than the surfaces have been meshed with new 2D elements, and from these elements a tetrahedral 3D mesh was developed. Due to the size and shape of the IGMAS+ triangulation elements, they could not be used directly to create a 3D mesh. The geometry of the density model and the dynamic models are nearly identical. The geometry

were changed slightly only where angles of the density model are to steep for dynamic modelling.

4.2 Model set up

Besides geometry the mesh, boundary conditions, interaction properties and rheological parameters are essential for the numerical models. Therefore, the model set up is described in the following sections and the assumptions made for the models are discussed. The ABAQUS input file for the reference model can be found in the appendix.

4.2.1 Model geometry

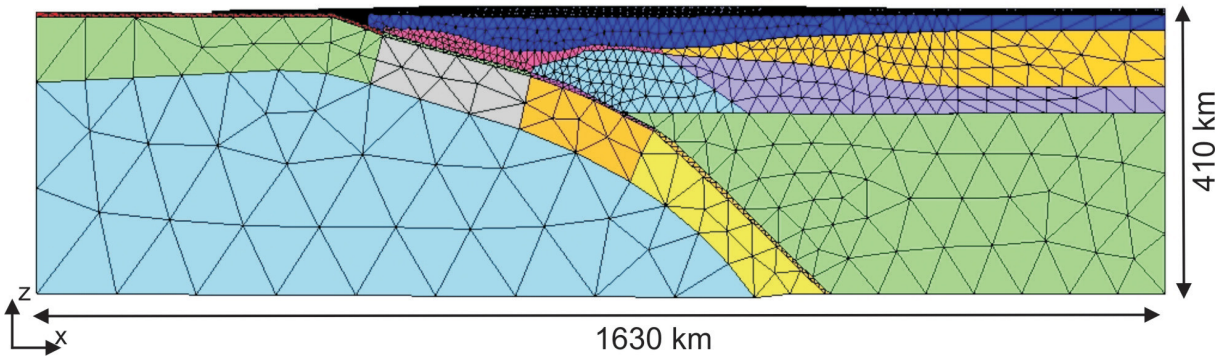

Figure 4.1: x-z view of the final mesh of the FE-models: The models are 725 km wide in north-south (y) direction which is not shown here. The different colours represent different material properties (Figure 4.3).

For the models discussed in this work the area $17°S - 23.5°S$ and $60°W - 75.5°W$ was chosen (rectangle in Figure 1.2), because it includes the bending of the trench. Therefore, the effect of trench geometry can be investigated. The geometry was taken from the density model (Section 2.2) developed by *Tassara et al.* (2006). In this region normal subduction occurs with an average subduction angle of circa 30°. In former works it was shown, that the trench geometry effects the model results (*Bonnardot et al.*, 2008; *Boutelier and Oncken*, 2010; *Gassmöller*, 2011; *Zeumann et al.*, 2013). The trench in the investigation area shows a oceanward concave bending. A topography grid of 10 minutes from ETOPO1 (*Amante and Eakins*, 2009) was added to the continental plate. But, bathymetry is not considered because this would need a finer mesh for the oceanic plate which will increase the element and node number and therefore the computational time. The primary part I am interested in is the continental plate. Due to the fact that ABAQUS has problems with elements with angles $< 20°$, geometries with small angles need a very fine mesh which will increase the computational time considerably. Therefore,

the first 50 km away from trench of the fore-arc are neglected because it is not the region investigated in this work. The fore-arc wedge of South America was investigated by *Kellner* (2007). Fault systems like the Atacama fault zone and the Precordilleran fault system are not included in the model geometry. The final models are 1630 km long in EW, 725 km wide in SN and 410 km deep. The models consist of 1 346 296 continuum elements with 1st order tetrahedron shape (in ABAQUS element type C3D4) and 327 389 nodes. The element size reaches from 2 to 3 km in the upper continental crust to 100 km in the oceanic asthenosphere (Figure 4.1). Like the density model the FE-models consist of 18 different units with various rheological parameters (Section 4.2.5). The geometry, mesh and interaction properties are equal for all models discussed in this work. Rheological parameters and boundary conditions are different to investigate their effects on the deformation and stress field.

4.2.2 Boundary conditions

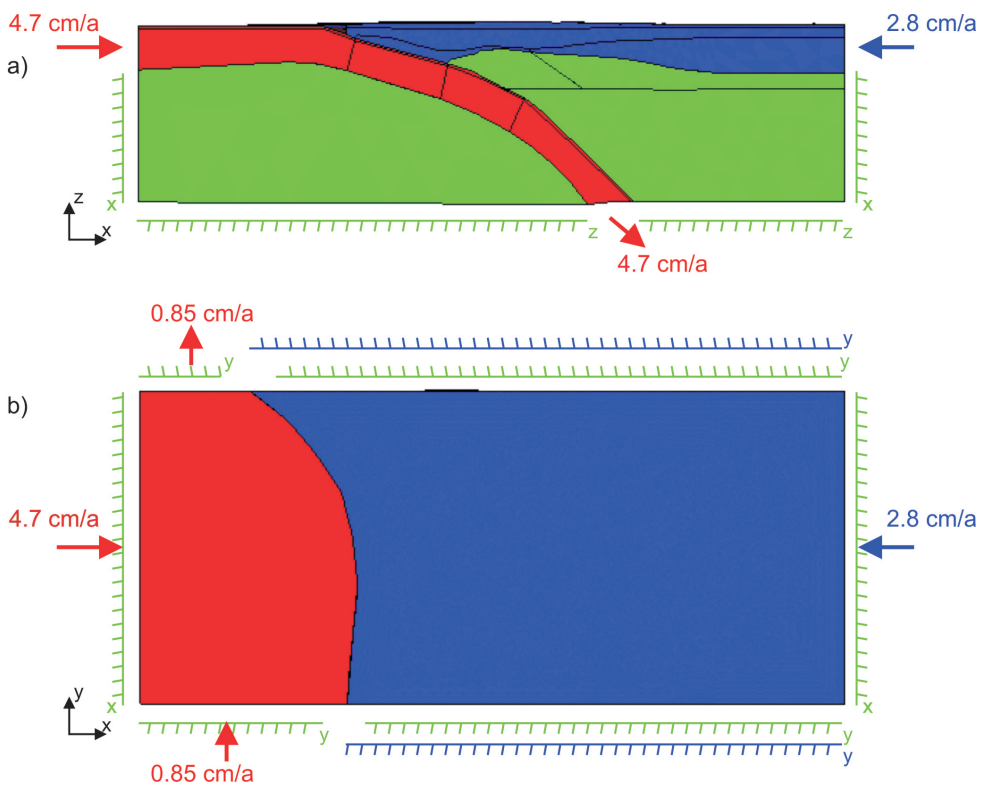

Figure 4.2: Boundary conditions applied to the model: Side view (a) and top view (b). Blue are the boundary conditions for continental lithosphere, red for oceanic lithosphere and green for asthenosphere.

The simulation is realized in two steps. The first static step is needed to implement the gravity (Section 4.2.4) and is calculated in one increment. For this step the bottom is fixed in vertical direction (z), north and south edge are fixed in y-direction, east and west

edge are fixed in x-direction and the surface boundary is free. In this step gravity acts as a load on every element of the model with a value of 9.81 m/s^2 and an initial stress field is given to minimize deformations (Section 4.2.4).

In the viscous second step gravity continues and additional velocities simulating the plate movements are applied as kinematic boundary conditions. The asthenosphere edges are still fixed as in step 1 and only at the edges of the lithospheric plates velocity boundary conditions are applied (Fig 4.2). Various modelling results in former times show, that the movement of the continental plate towards the trench is important for high mountain building (*Hampel and Pfiffner*, 2006; *Babeyko and Sobolev*, 2008). In the models presented in this work the South American plate is moved by 2.8 cm/a in west direction and the Nazca plate has a convergence rate of 5 cm/a (*Silver et al.*, 1998; *Somoza*, 1998).

Considering an obliquity of 20° the value of 5 cm/a is split in an east component of 4.7 cm/a applied at the west edge of the slab and a north component of 1.7 cm/a. The north component is divided by 2 and the value of 0.85 cm/a is applied to the south and the north edge of the slab. The amount of slab pull is not well known (Section 2.5). For the reference model the same value as for the east component of the ridge push (4.7 cm/a) were taken acting at the bottom of the slab with an angle of 30°, the subduction angle of the models. In Section 5.3 the amount of slab pull is varied to investigate the effect on the model results.

4.2.3 Interactions

As the density model of *Tassara et al.* (2006) the dynamic models have 16 different parts characterizing the main geological structures. If there should be no contact interaction (e.g. friction or free sliding) between neighbouring parts these two parts have to be connected. Usually these units share their edge nodes to be connected, but this is not always possible due to the different mesh size of the neighbouring parts. To combine such parts or to define a contact interaction between the units, a master surface and a slave surface have to be defined. For combination the two surfaces are tied together. In the models this was the case between the continental asthenosphere and the upper continental asthenosphere, between the lower and upper continental crust and between the oceanic mantle lithosphere and the oceanic crust (green lines in Figure 4.3). To avoid gaps between the surfaces a position tolerance of 4000 m was defined for the slave nodes (Figure 3.5).

For contact interactions like friction or free sliding an interaction option has to be defined between the surfaces. A contact with free sliding is modelled between the upper continental asthenosphere and the continental lithosphere and between the oceanic asthenosphere

and the oceanic lithosphere with a position tolerance of 4000 m (blue lines in Figure 4.3).

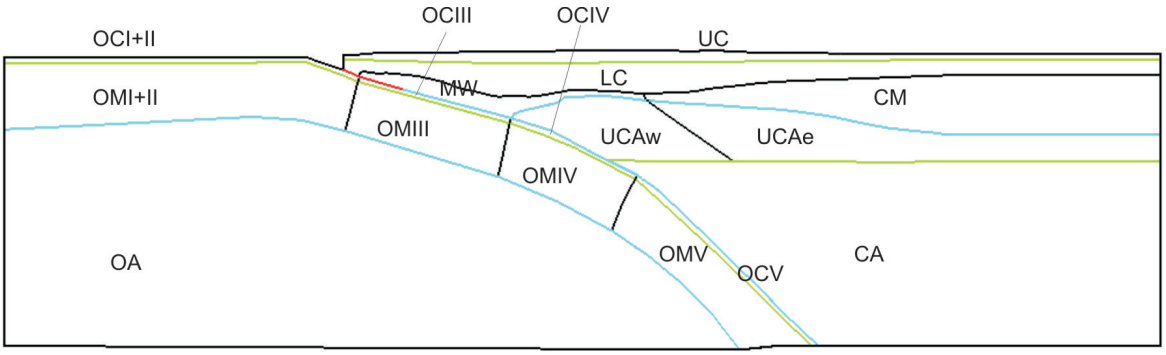

Figure 4.3: Different parts of the model and their contact interactions: Green lines specify tied surfaces, blue lines denote contact interaction with free sliding, and the red line highlights the frictional coupling zone with 0.3 as friction coefficient. For abbreviations of the unit names see Table 4.1.

A fundamental controlling factor of the deformation pattern at the surface of subduction zones is the frictional coupling of the descending slab and the overriding plate. After *Wang and Suyehiro* (1999) the downdip limit of the seismogenic zone can be taken for the depth extent of the frictional coupling zone. The extension of the coupling zone can be estimated from phase transitions occurring at specified temperatures, from seismic events or from elastic modelling of GPS data. The upper boundary is controlled after *Hyndman et al.* (1997) by the phase transition of smectite to illite at temperatures between 100-150°C, which corresponds to a depth of 5 to 15 km. But also other mechanisms than clay minerals transformation may be important (*Saffer and Maroneb*, 2003). The down-dip limit of the coupling zone is defined by the max. temperature of 350°C. Above this temperature most rocks and minerals behave viscous or plastic. Therefore, the down-dip limit can be estimated in 40 to 50 km depth. *Tichelaar and Ruff* (1991) estimated the down-dip limit in the northern Chile region from large underthrusting earthquakes and conclude that coupling extends at least as deep as 45-48 km. *Husen et al.* (1999) determined the seismogenic zone between 20 km and 46 km based on the aftershock locations of the Antofagasta earthquake in July 1995. The coupling depth based on elastic dislocation modelling of GPS data is 33 km for northern Chile (*Khazaradze and Klotz*, 2003; *Hoffmann-Rothe et al.*, 2006) which is lower than the estimation from seismic events or phase transition.

Besides the extension of the coupling zone the friction coefficient is important and is still a matter of discussion. Strong interplate coupling, which is revealed by high magnitude earthquakes, is likely associated with tectonic erosion (*Bonnardot et al.*, 2008). The

Central Andean margin is a region with large earthquakes, like the Antofagasta earthquake in 1995 with a magnitude of M_w 8.1, the Arequipa earthquake in 2001 with M_w 8.4, or the Toccopilla earthquake in 2007 with M_w 7.7 (*Schurr et al.*, 2012), and is also known as a prominent erosive margin (*Rutland*, 1971).

Kellner (2007) found friction coefficients for South America between $0.3 \leq f \leq 0.4$ running 3D numerical models for 150 000 years and compared the results to GPS data. These values are in good correlation with results of laboratory experiments (*Kellner*, 2007). *Sobolev and Babeyko* (2005) investigated the evolution of the Central Andes over the last 35 million years considering a subduction channel between the plates. They found that friction coefficients f > 0.1 resulted in slab break off and termination of subduction, and for f between 0.05 and 0.1 subduction survived but shortening of the overriding plate is too strong. The model that replicates the case of the Central Andes most closely has a friction coefficient of f ∼0.05 (*Sobolev and Babeyko*, 2005). After *Ramos* (2010) the friction coefficient in the subduction channel is a first-order parameter to transmit deformation to the upper plate. The friction is directly related to the amount of sediments in the trench. Starving trenches under extreme arid conditions, as the Peru-northern Chile trench in region of the Central Andes, will have a high coupling, while the overfilled trenches in humid climates as in the southernmost and northernmost Andes will have a lower plate coupling (*Ramos*, 2010).

In this work the up dip limit is not needed, because the first approx. 50 km of the fore-arc wedge are neglected (Section 4.2.1). Therefore, the coupling zone starts immediately which corresponds to a depth of 20 km and extends until a depth of approx. 50 km (red line in Figure 4.3). The models run 100 000 years and model setup is more close to the work of *Kellner* (2007) than to the long time evolution models (e.g. *Sobolev and Babeyko*, 2005; *Babeyko and Sobolev*, 2008). Therefore, a friction coefficient of 0.3 was chosen for the coupling zone. Below the coupling zone the contact is modelled as frictionless with free sliding between the Nazca and the South American plate. The position tolerance for these two contacts is 3000 m.

Investigations of frictional parameters have been done in a separate work within the IMOSAGA project (Sharma in prep.).

4.2.4 Implementing gravity

Gravity is one fundamental force acting on everything on earth. It hinders uplift and has to be considered to study crustal deformation. To implement gravity a static step at the beginning of the model process was included, where only gravity acts on the whole model

and no plate velocities are applied. The major problem of this step is the subsidence of the model especially in the subduction zone area due to the contact between the two plates. The maximum subsidence is larger than 20 km (Figure 4.4 model 1) destroying the geometry of the model. To minimize this effect a pre-stress is used at the beginning of the step calculated as follows. First model 1 runs without pre-stress. After this step ABAQUS generates an output of the resulting stress components for each element. In an equilibrium

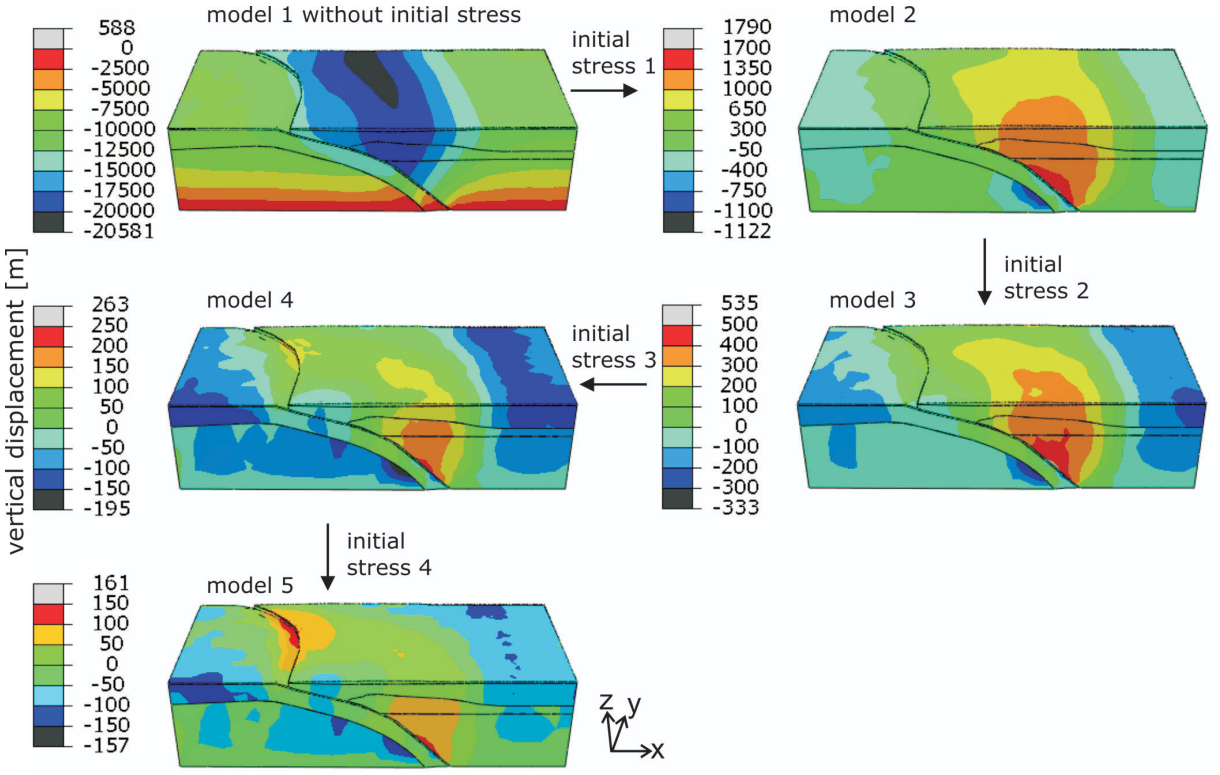

Figure 4.4: Workflow of the initial stress calculation and its effect on the vertical displacement: Note that pictures of vertical deformations have different scales.

state the normal stress components are equal to the vertical stress component (S_{zz}) and the shear components vanish, because gravity is acting only in negative z-direction and there are no forces applied to the model edges. Therefore, the normal stress components were set to S_{zz} and the shear components to 0 for each element. This stress field is then used as initial stress condition to model 2. After running model 2 with pre-stress the subsidence is one order less than for model 1 but uplift deformation is increased (Figure 4.4 model 2). Therefore, the stress components of model 2 are reported and a new initial stress field is generated and used in model 3 and so on. Figure 4.4 shows the workflow of the initial stress calculation. In model 5 the deformations are max. 160 m only which are small enough compared to the model depth of 410 km. Therefore, this initial stress was used at the beginning of modelling and after the static step a second viscous step with plate velocities (Section 4.2.2) was added. For the static step viscosity parameters are ignored and therefore all models in this work have the same initial stress field as long

as densities and Young's moduli remain the same.

4.2.5 Material parameters - Model rheology

The density model of *Tassara et al.* (2006) (Section 2.2) satisfies the observed gravity data and is well constrained by seismic observations and petrological data. Therefore, these densities are taken for the dynamic models. The elastic parameter Young's modulus can be calculated from the density and seismic velocity (Equation 3.16). For all units a Poisson's ratio of 0.25 was used. With v_p velocities taken from the velocity model (Section 2.3) and the relation $v_s = 1/\sqrt{3}v_p$ Equation 3.16 results in the Young's moduli given in Table 4.1.

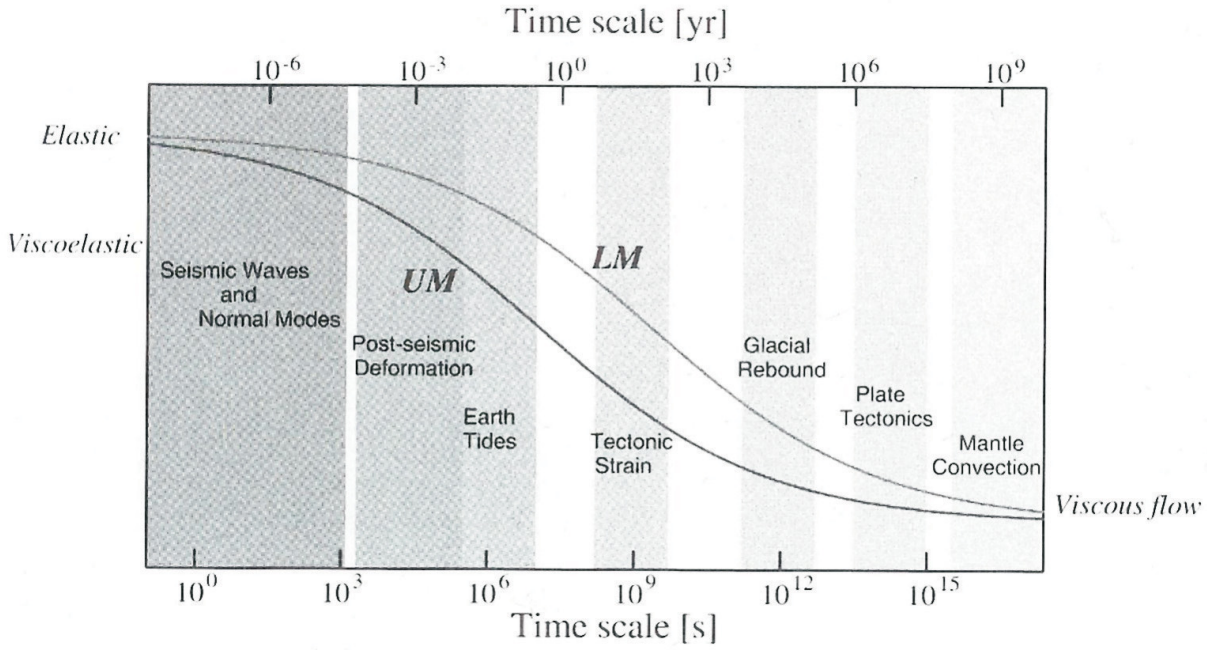

Figure 4.5: Different rheological behaviour of upper (UM) and lower (LM) mantle under consideration of time scales (*Kennett and Bunge*, 2008).

If transient phenomena are neglected the mantle can be considered as a viscoelastic (Maxwell) body with an elastic response for short time scales followed by a linear (Newtonian) viscous response as exemplified from postglacial rebound data (*Ranalli*, 1995). Assuming the mantle as 'half-space' an average viscosity of the order of 10^{20}-10^{21} Pa·s for the upper mantle, and for the lower mantle values one to two orders of magnitudes higher, seems to be well established. These values satisfy postglacial rebound data, observations on geoid anomalies, plate motions, and convective patterns in the mantle as inferred from seismic tomography (*Ranalli*, 1995). However, in the uppermost part of the asthenosphere viscosity can drop to 10^{19} Pa·s (*Eisbacher*, 1996). Figure 4.5 shows the

rheological behaviour of upper and lower earth mantle under consideration of different time scales. For very short time scales (some seconds) even the mantle can treated as elastic but for larger time spans viscosity has to be considered.

Table 4.1: Rheological parameters for the reference model: Densities (ρ) are taken from the gravity model (*Tassara et al.*, 2006), seismic velocities (v_p, v_s) are taken from the seismic profile (*ANCORP Working Group*, 2003) and calculated by the relation $v_s = 1/\sqrt{3}v_p$. E is the Young's modulus and η is the viscosity.

model part	ρ [kg/m^3]	v_p [m/s]	v_s [m/s]	ν	E [GPa]	η [Pa·s]
upper crust (UC)	2700	5900	3406	0.25	78	-
lower crust (LC)	3100	6300	3637	0.25	103	-
con. lith. mantle west (MW)	3230	6400	3695	0.25	110	-
con. lith. mantle east (CM)	3320	7000	4041	0.25	136	-
upper con. asth. west (UCAw)	3320	7700	4446	0.25	164	10^{19}
upper con. asth. east (UCAe)	3350	8100	4677	0.25	183	10^{19}
con. asth.(CA)	3430	8500	4907	0.25	207	10^{21}
oc. crust (OCI+II)	3050	6200	3580	0.25	98	-
oc. crust (OCIII)	3200	6500	3753	0.25	113	-
oc. crust (OCIV)	3300	6500	3753	0.25	116	-
oc. crust (OCV)	3550	6500	3753	0.25	125	-
oc. lith. mantle (OMI+II)	3350	8100	4677	0.25	183	-
oc. lith. mantle (OMIII)	3370	8100	4677	0.25	184	-
oc. lith. mantle (OMIV)	3400	8100	4677	0.25	186	-
oc. lith. mantle (OMV)	3500	8100	4677	0.25	191	-
oc. asth. (OA)	3411	8500	4907	0.25	205	10^{21}

"Thin channel" models as described by *Artyushkov* (1983) restrict the flow to a thin channel below the lithosphere with viscosities in the order of 10^{19}-10^{20} Pa·s. With $\eta \simeq 10^{21}$ Pa·s and $\mu \simeq 10^{11}$ Pa the Maxwell time (Equation 3.27) is of the order of 1000 a. From post glacial rebound it is firmly established that the mantle is a "fluid" even at deviatoric stresses as low as 1 MPa, and that the evidence for characteristic times longer than about 1000 to 10 000 years is compatible with a Newtonian, steady-state rheology (*Ranalli*, 1995). After *Billen* (2008) at least in the upper mantle diffusion creep (linear viscosity) and dislocation creep (nonlinear viscosity) act together. However, diffusion creep dominates deformation at cooler temperatures and larger grain sizes whereas dislocation creep is grain size independent and more important at higher strain-rates. For most of the models a linear viscosity is assumed, because power law creep leads to a very small pre-exponent ($A < 10^{-30}$) which causes convergence problems. The effect of nonlinear viscosity for the upper continental asthenosphere is investigated in Section 5.4.1.

Typical viscosities for lithospheric rocks are of the order of 10^{23} Pa·s (*Turcotte and Schubert*, 2002). This results in a Maxwell time of the order of $\sim 10^5$ to 10^6 years which is equal or higher than the time span of the models. Therefore, the lithosphere is considered as elastic in the reference model. See Section 5.5 for an explanation how a viscosity of 10^{23} Pa·s in the lithosphere affects the deformation patterns in the continental crust. For the asthenosphere a viscosity of 10^{21} Pa·s for the continental and oceanic asthenosphere and of 10^{19} Pa·s for the upper most part of the continental asthenosphere were taken following *Turcotte and Schubert* (2002). The influence of the mantle viscosity will be investigated in this work. Parameters used for the reference model are listed in Table 4.1. The results of this reference model are discussed in Section 5.1.

4.2.6 Model assumptions and restrictions

Subduction is a very complex process with many aspects, which are up to now not fully understood. Some of these aspects are related to rheological parameters of lithosphere and asthenosphere, affects of fluids like water and magma, phase transitions, temperature, coupling between the plates, coupling between lithosphere and asthenosphere, etc. Therefore, it is not possible to consider every detail and process in one model and simplifications and assumptions are neccesary for modelling. Some of the assumptions for the models in this work are discussed in this section.

The spherical shape of the earth is not considered for the models. The height difference h for a point in the centre of the model can be calculated as follows:

$$h = 2rsin^2\left(\frac{\alpha}{4}\right); \qquad \alpha = \frac{360°b}{2\pi r}. \tag{4.1}$$

With r=6371 km, the average earth radius, this results in h=52 km for b=1630 km and h=10 km for b=725 km. In most models the curvature of the earth is not considered (e.g. *Babeyko and Sobolev*, 2008; *Bonnardot et al.*, 2008; *Boutelier and Oncken*, 2010). However, a flat approximation of the models might lead to deviations (*Antonioli et al.*, 1998; *Heidbach and Drewes*, 2003).

The models presented in this thesis are 410 km deep and include the asthenosphere which is neglected in various other model approaches (e.g. *Liu et al.*, 2002; *Hampel and Pfiffner*, 2006; *Kellner*, 2007). Thus, the effect of varied asthenosphere viscosity can be investigated. Viscosity depends as other material parameters strongly on temperature and pressure. But, temperature is not considered in the models. To include it, a 3D temperature model is needed for the investigation area, which can be implemented in ABAQUS. Temperature boundary conditions alone will not be sufficient, because the model has to run a few millions of years to establish a realistic temperature distribution,

but this will change the geometry of the model as well. In the short computation time span of 100 000 years the temperature will change only slightly. Therefore, temperature is neglected in this work. Other authors consider temperature in long term evolution models of the Andes in 2D (e.g. *Babeyko and Sobolev*, 2008).

Due to limitation of computational capacity not all aspects of the complex subduction process can be considered in one model. Mantle convection in the earth mantle is connected to temperature and play a role as driving mechanism for plate movements. Fluids play also an important role for subduction processes, especially for the developing of the magmatic arc. But, this is not the subject of this work and therefore mantle convection and fluids are neglected here. Erosion works against uplift. For erosion the climate conditions are relevant. However, investigation of erosion is not the intention of this work and thus erosion is ignored. Due to the resolution of the models a subduction channel as described by *Babeyko and Sobolev* (2008) is disregarded in this work.

Gassmöller (2011) investigated the influence of the element type on the results. He comes to the conclusion, that 2nd order elements show more precise stress patterns than 1st order elements and that cubic elements are more precise than tetrahedrons. But 2nd order elements have more nodes per element and therefore increase the computational time significantly. Here 1st order tetrahedral elements are used because cubic elements are not suitable for the geometry and 2nd order elements would need too much computer capacity. To investigate stress the thickness of the units should be at least 3 elements (*ABAQUS tutorial version 6.10*, 2010), which is the case for the continental crust, but not for the oceanic crust. Modelling the thin oceanic crust with smaller elements would dramatically increase the element and node number and therefore the computational time. Another possibility would be to consider oceanic crust and oceanic mantle as one unit, but then the material parameters would be equal which is not true in reality. The parameters of the slab will influence the deformation pattern in the continental crust, where the main interest of this study lies. Therefore, the distinction in crust and mantle was made for the slab, which is closer to reality. Because of the few elements the stress solution on the oceanic plate should be considered with care and the effect on the interpretation should be taken into account.

The existing models have generic geometries and the slab is modelled as one homogeneous unit (e.g. *Sobolev and Babeyko*, 2005; *Hampel and Pfiffner*, 2006; *Kellner*, 2007; *Babeyko and Sobolev*, 2008; *Bonnardot et al.*, 2008). The 3D models presented here have a structure taken from a well constrained density model. However, the density model is one possible solution fitting the observed Bouguer anomaly and the seismic velocities used for Young's modulus calculation have also small uncertainties. Due to the fact, that

these models are well constrained, they are the best possible boundary conditions for the dynamic models. The structure of the FE-models is therefore most realistic including also the curved trench of the Central Andes region. The slab is not considered as a single unit but divided in several parts like the density model on which the structure is based. These different parts are a first approximation to imply the densification with depth of the slab due to metamorphic reactions caused by increased temperature and pressure conditions. However, the unit parameters did not change during subduction. The precise viscosity of the earth is unknown and therefore it can be roughly estimated only for the models. To investigate the influence of asthenosphere its viscosity is varied in a model series and the results are compared. The effect of different lithosphere rheologies is also tested.

Besides a most realistic structure (e.g. trench geometry, slab distinction) and nearly realistic material parameters the models include gravity, oblique convergence and over-riding velocity of the continental plate. Therefore, this work presents for the first time models with realistic structure and parameters for the central part of the South American subduction zone and the Central Andes.

5 Results

In the following chapter the results for different models are described. In most figures the results are shown as top view on the model. The subject of interest is the South American plate. Therefore, the legend interval was chosen to show the results on this plate and the results of the oceanic plate are in some pictures out of legend range. Because, the scale is valid for the whole model there are regions with higher (grey) or lower (black) values than the chosen legend interval. Therefore, every picture has a legend with grey and black even when it is not visible in the top view. On some of the model results the morphotectonic units (*Tassara*, 2005), described in Section 2.1, are plotted in yellow or black. For abbreviations of the units see Figure 2.1. The left line of these units marks the coastline. Note that the black curved line in the middle of the models is the edge of the modelled continental plate and not the trench. Due to the fact, that the first ∼50 km of the fore-arc are neglected for numerical reasons (Section 4.2.1), the trench and beginning of the continental plate is not identical. The trench is ∼50 km farther west parallel to the black curved line. The scale at the bottom of the models shows the distance away from trench to the east, which is valid for the southern model part where no trench curvature occurs. The definition of sign for extensional and compressional strain is not consistent in geosciences. In ABAQUS an extensional regime is defined by a positive sign and compression has a negative sign. The term "higher strain" is therefore equal with the term "lower compressional strain", which might lead to confusion. For example -0.02 is higher than -0.04 (-0.02 higher strain), but -0.02 mean less compressional strain than -0.04 (-0.02 lower compressional strain), because more negative equals more compression. In case of vertical displacement positive values denote uplift and negative values mean subsidence. Subsidence occurs in most parts of the model due to gravity and slab pull.

5.1 Results of the reference model

Model setup, boundary conditions and rheological parameters for the reference model were described in the previous sections. The model runs for 100 000 years and the output was reported after every 5000 years. Figure 5.1 a) shows the vertical displacement after 100 000 years running time. The result after step 1 (beginning of step 2) was subtracted, because the uplift due to plate motion is the matter of interest. Most parts of the continental crust show subsidence (negative values). Only in the offshore fore-arc and at the eastern edge uplift occurs. The subsidence is less in the area of the Coastal Cordillera (CC) and the Longitudinal valley (LV) with values in the range from -500 m to 0 m vertical displacement. Same values are modelled for the Subandean range. The largest subsidence fits an area called the Atacama basin (Ab) with values down to -2500 m. However, an edge effect cannot be excluded because of the nearby model boundary. Altiplano plateau (AP) and Eastern Cordillera (EC) show a subsidence of -500 to -1000 m.

To compare the modelled uplift/subsidence with estimated uplift rates from geological observations (e.g. *Gregory-Wodzicki*, 2000) it is useful to express the results in mm/a (Figure 5.1 b). Figure 5.1 c) shows the evolution of the deformation components over the whole modelling time for the orange dot in Figure a). It shows that there is not a linear evolution. At the beginning of modelling time there is a running in behaviour which is caused by gravitational force (Section 5.2) and should not be considered for trend calculations. For the last years the trend can be assumed as linear. Therefore, the displacement rate (or velocity) was calculated by subtracting the results at 95 000 years from the results at 100 000 years, divided by 5000 years. After this the result was multiplied by 1000 to get the unit mm/a.

The model results in the fore-arc can be distinguished in a southern and northern part (Figure 5.1 b). In the southern part of the model the trench is oriented in north-south direction and the convergence velocity of the Nazca plate is oblique. The onshore fore-arc and Coastal Cordillera show an uplift rate of 2 to 4 mm/a. By investigation of ancient preserved marine terraces in the coastal area an uplift rate of about 0.15 mm/a is observed (*Ortlieb et al.*, 1996a; *Ortlieb et al.*, 1996b; *Kukowski and Oncken*, 2006). These values are one order of magnitude lower than the modelled uplift. In contrast, the northern part of the model has a curved trench and the convergence velocity is nearly perpendicular to the trench. Here the offshore fore-arc shows subsidence rates with values of -5 to -9 mm/a. Note, that the total vertical deformation after 100 000 years shows uplift in the northern part of the offshore fore-arc region and subsidence in the southern model part (Figure 5.1 a). But, the deformation rates reveal subsidence in the northern part and uplift in the southern part of the fore-arc region (Figure 5.1 b). Due to the thickness of the single units,

which is not constant in the model, and the surface topography, the effect of gravity is different for several parts. This leads to various running in behaviours for different points in the model, which is the reason for the difference between the total deformation pattern after 100 000 years and the deformation rate pattern calculated from the last 5000 years. The result of fore-arc subsidence at the oceanward concave margin (northern part) and uplift at the straight margin (southern part) fits to the modelling results of *Bonnardot et al.* (2008). These authors come to the conclusion that an oceanward concave margin induces subsidence and a convex shape margin induces uplift approximately 80 km away from the trench.

It seems that the trench geometry influences the vertical deformation in the fore-arc only, because east of the Western Cordillera a distinction in north and south cannot be made (Figure 5.1 a and b). The Atacama basin shows a subsidence rate of circa -9 mm/a. The Altiplano plateau shows a subsidence of -3 to -4 mm/a. In contrast to this result *Gregory-Wodzicki* (2000) estimated from paleoelevation data an uplift rate of 0.2 to 0.3 mm/a for the Eastern Cordillera and Altiplano plateau for the last 10 million years. The Subandean range shows a modelled uplift rate of some mm/a.

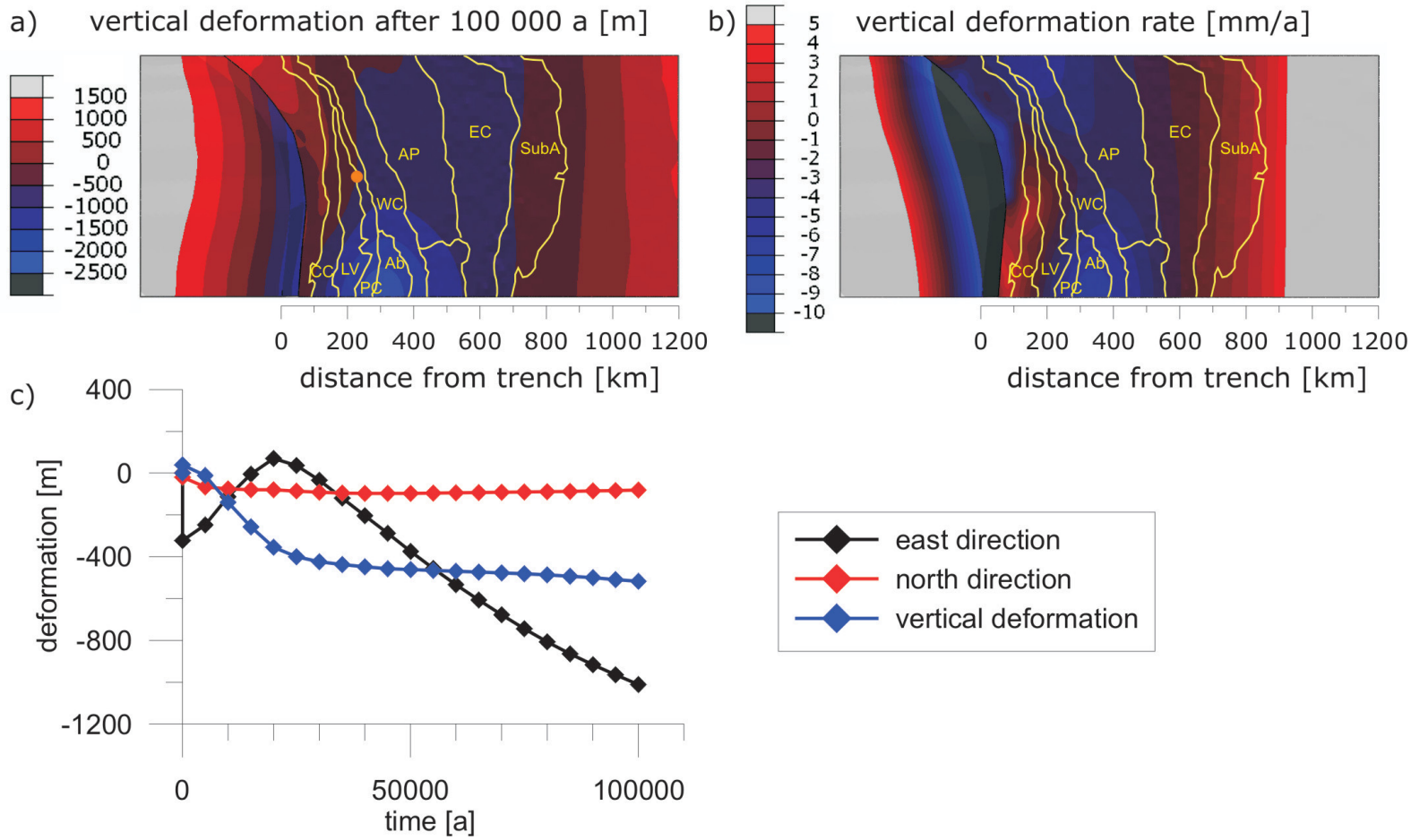

Figure 5.1: Vertical deformations after 100 000 years (a), and expressed in mm/a calculated from the last 5000 years (b). Yellow lines denote the morphotectonic units. For abbreviations see Figure 2.1. c) Evolution of the vertical and horizontal deformations for the orange point in a) shows a running in behaviour at the beginning of modelling caused by gravitational force (Section 5.2). But, for the the last years the trend can be assumed as linear.

The horizontal displacement rates can be compared with the components of the observed GPS velocities (Figure 5.2). The GPS observations are relative to the stable core of the South American plate (*Kendrick et al.*, 2001). To make the results comparable the applied velocity of -2.8 cm/a was subtracted from the east component of the calculated velocity field. 200 km away from the trench the modelled displacement rates in east direction show values between 18 and 21 mm/a, which fits the GPS observation of $\sim$ 20 mm/a fairly well. An eastward decrease in velocity is seen in the modelled as well as in the GPS results. The red spot with values >27 mm/a might be caused by the nearby model edge. An effect of the trench geometry is hard to identify. For the deformation in north direction an eastward decreasing cannot be seen by the GPS data and an average value for velocity is $\sim$6 mm/a. In the modelled results the north displacement changes to southward displacements (blue negative values) $\sim$200 km away from trench. The displacement rates in the centre of the model show values of 2 to 5 mm/a which are a little bit lower than the values from GPS data.

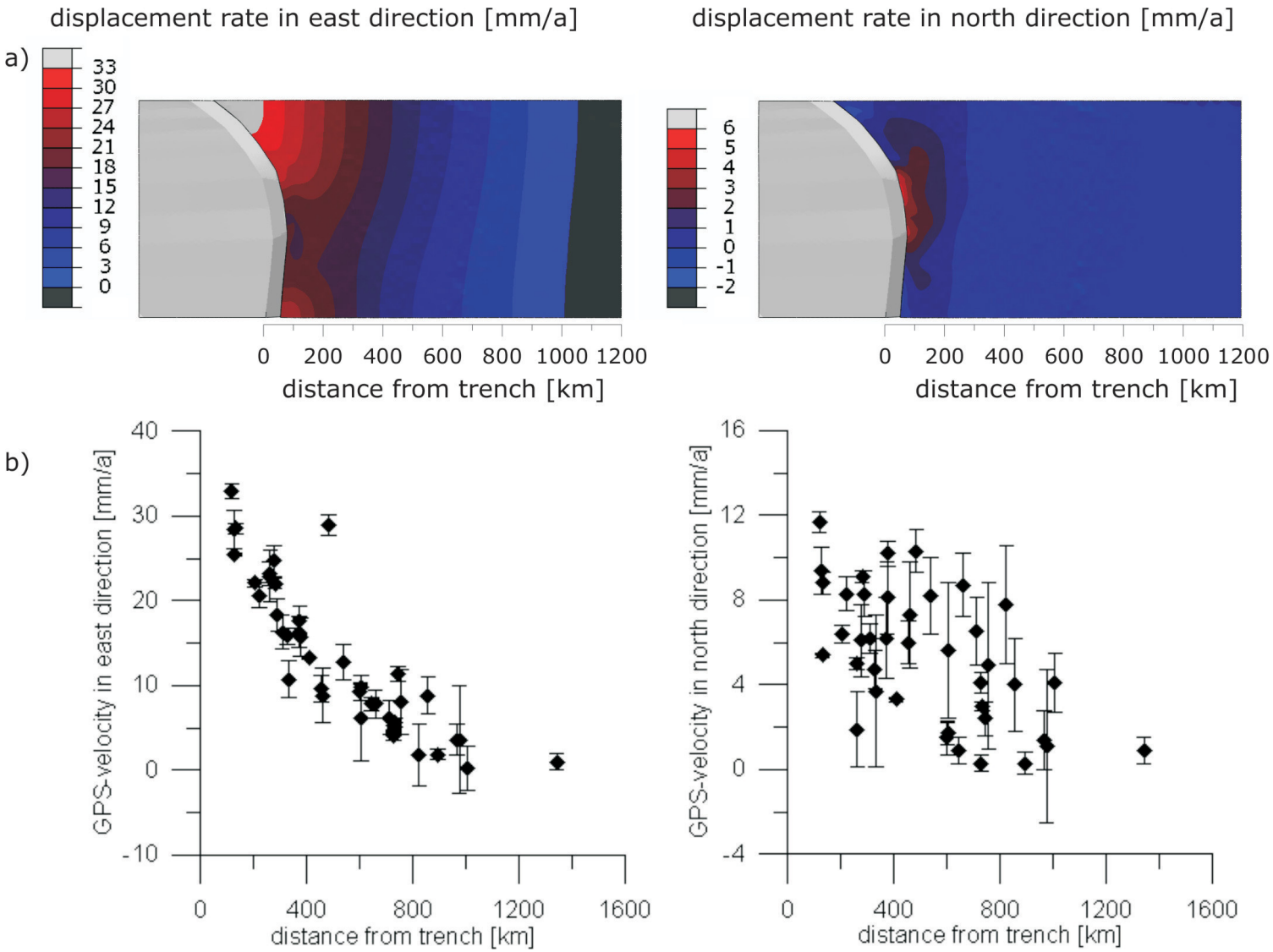

Figure 5.2: Horizontal displacements in east and north direction in mm/a (a) compared to observed GPS data from *Kendrick et al.* (2001) (b).

Another possibility to investigate deformations is to consider the strain. The horizontal strain components after 100 000 years and expressed as strain rates calculated from the last 5000 years are shown in Figure 5.3. The east-west strain after 100 000 years shows that most of the model has a compressional regime (negative values) and the largest compressional strain occurs in the Precordillera (PC), Western Cordillera (WC), and Atacama basin (Ab) with values in the range of -0.004 to -0.006 (blue belt). It seems that trench geometry affect the strain. The compressional strain in the arc region (PC, WC) is higher in the south, where the margin is straight, than in the northern part, where the margin has a concave shape. In contrast the compressional east-west strain in the Eastern Cordillera (EC) and Subandean region (SubA) is higher in the north (-0.002 to -0.003) than in the southern part (-0.001 to -0.002). In the centre of the model the fore-arc region shows an area of extensional strain (positive values) in the coastal region, which might be also an effect of the trench geometry. (*Bonnardot et al.*, 2008) found that a concave shaped margin induces an extensional regime in the upper plate. But, the area of extension in Figure 5.3 is not in the zone of maximum trench curvature but a little further south. In the horizontal shear strain component compressional strain occurs in the northern part and extensional strain in the southern part of the fore-arc region. Due to the curved trench the obliquity of convergence velocity of the Nazca plate varies within the model. In the southern part, where the trench is straight the convergence obliquity is 20° whereas in the curved trench area in the northern part of the model the convergence velocity is nearly perpendicular to the trench (obliquity angle = 0). The compressional strain in the fore-arc increases with increasing obliquity angle, what was also shown by (*Kellner*, 2007) and (*Zeumann et al.*, 2013).

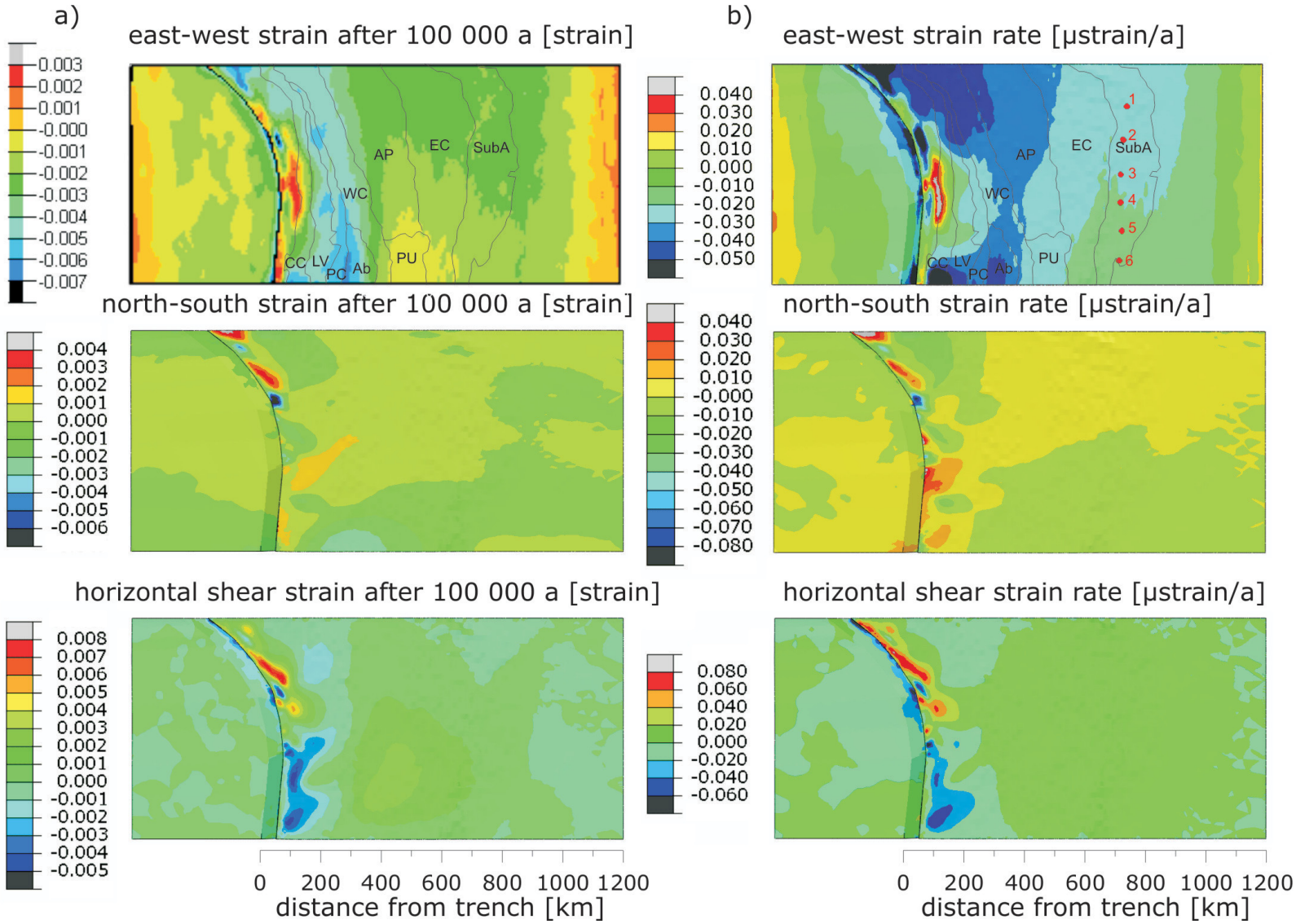

Figure 5.3: Horizontal strain components after 100 000 years (a) and expressed in mm/a calculated from the last 5000 years (b): Black lines denote the morphotectonic units. For abbreviations see Figure 2.1. For the red points values of horizontal strain rate components and calculated principal strain rates are summarized in Table 5.1.

In the Subandean region the model reveals horizontal strain rates with values between -0.015 and 0.025 μstrain/a in east-west, less than 0.001 μstrain/a in north-south, and for the shear component between 0.02 and 0.005 μstrain/a (Figure 5.3 b). Table 5.1 shows the horizontal strain rate components as well as the calculated horizontal principal strain rates (Equation 3.38) and axis (azimuths) for the red points marked in Figure 5.3. The principal strain rates calculated from the model results can be compared to the recent strain rates estimated from GPS measurements and geological observations. *Hindle et al.* (2002) estimated recent principal strain rates from GPS data and from geological observations considering the last 10 Ma which are by the factor 2 higher than the strain rates calculated from the models. The estimation of recent strain rate considering the last 25 Ma fits to the strain rate from the model. However, the estimation from geological observations have uncertainties. Therefore, it is a good result that the values from the model are in the same order of magnitude as the values from *Hindle et al.* (2002).

The strain rate is an expression for shortening. The value -0.022 μstrain/a is equal to a shortening rate of 4.4 mm/a at a length of 200 km. *Bevis et al.* (2001) investigated GPS measurements and found present shortening rates between the GPS stations in the Subandean region and the stable South American craton of ∼9.5 mm/a at 18.5°S and of ∼6.5 mm/a at 21.5°S, which means that the shortening rate is lower in the south. This is also the case for the shortening rates calculated from the model results however, the values are by the factor 2 lower (Table 5.1).

Table 5.1: Horizontal strain rate components, calculated principal strain rates and azimuths for the red points marked in Figure 5.3 b) compared to the estimations of *Hindle et al.* (2002). Shortening rates are calculated for a length of 200 km.

	strain rates [μstrain/a]					shortening rate
point	EW	NS	shear	principal	azimuth [°]	[mm/a]
1	-0.022	0.0011	0.003	-0.022	83	4.4
2	-0.022	0.0005	0.005	-0.023	79	4.6
3	-0.021	-0.0003	0.004	-0.022	79	4.4
4	-0.018	-0.0002	0.004	-0.019	77	3.8
5	-0.019	-0.0010	0.003	-0.019	80	3.8
6	-0.018	-0.0010	0.002	-0.018	85	3.6
estimated at 20°S (*Hindle et al.*, 2002)						
GPS				-0.038	83	
10 Ma				-0.041	83	
25 Ma				-0.022	88	

5.2 Effect of gravity

Gravity is a fundamental force acting on everything on earth. One model was running without gravity to check the effect of gravity on the results. All other parameters of this model are identical to the reference model. But in the first step, gravity, and initial stress were neglected. Figure 5.4 shows the von Mises stress (Equation 3.37) of the reference model (a) and the model without gravity (b) after 100 000 years. In the reference model the stress accumulates in the fore-arc region (green belt). When gravity is neglected the zone of stress accumulation shifts eastward and is lower than for the reference model. The deformation patterns change also when gravity is disregarded. For the black point in the

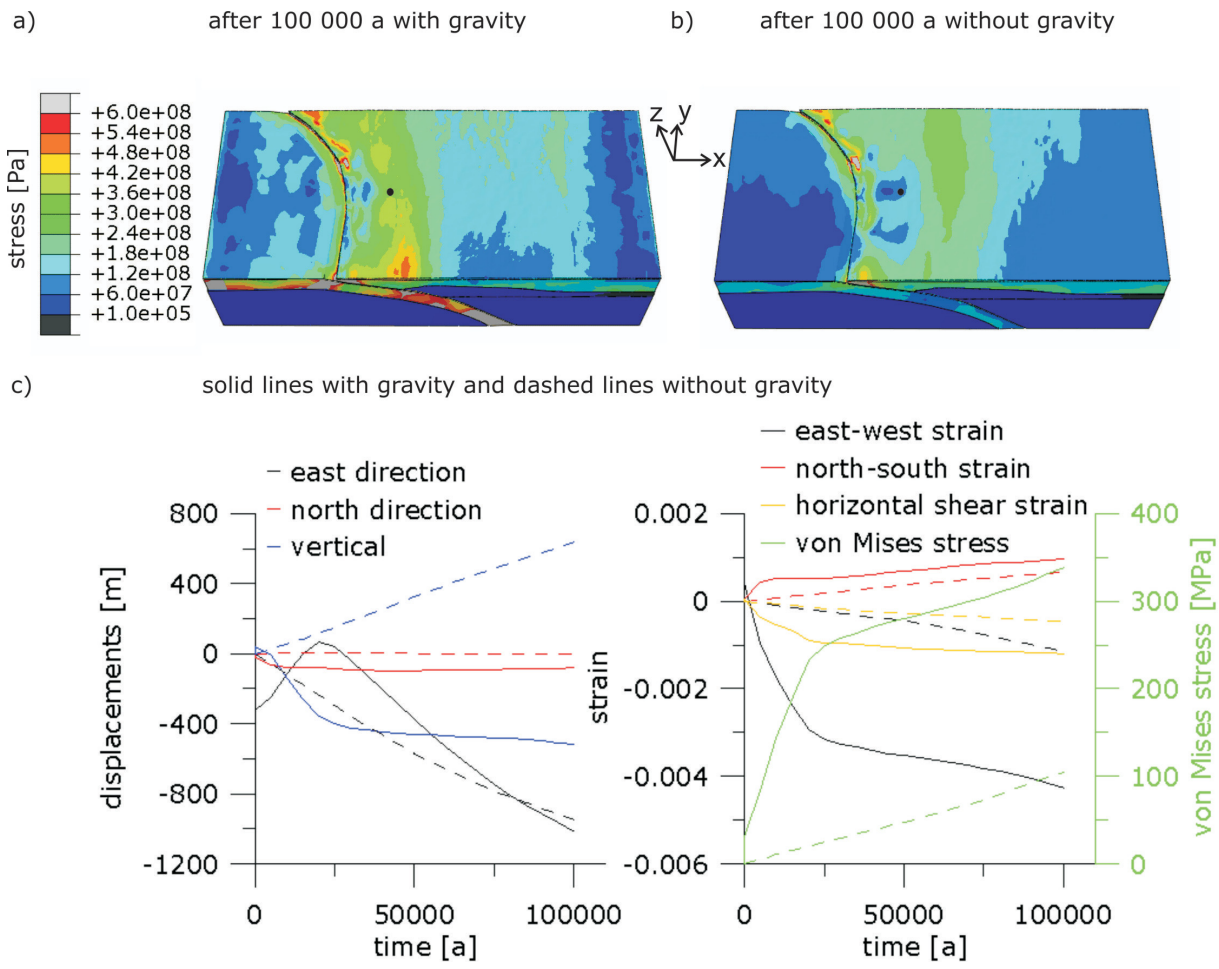

Figure 5.4: Von Mises stress after 100 000 years for the reference model (a) and a model without gravity (b): Area of stress accumulation shift eastward when gravity is neglected. c) Evolution of displacement and strain components for the black dot marked in a) and b). Displacement and strain components develop nearly linear from the beginning when gravity is disregarded (dashed lines) and show a region of maximum curvature at 20 000 years when gravity is included (solid lines).

figure, the evolution of the displacement and strain components are compared for the two

models (c). The solid lines denote the reference model, where gravity is considered and the dashed curves show the results for the model without gravity. All dashed lines show a nearly linear trend. In contrast the lines of the reference model reveal a steep slope at the beginning of the model until a zone of maximum curvature is reached after ∼20 000 years running time. After this the slope flattens and in case of the east displacement changes its algebraic sign. The trend at the end of the running time is similar between the two models, but not the total amount of values. However, in case of vertical displacement (blue lines) the curves differ totally. In the model without gravity uplift occurs from the beginning of modelling process. In contrast, the reference model shows subsidence which decreases after 20 000 years but is still present. The rapid subsidence at the beginning is due to gravity, because the initial stress given at the start of modelling process did not work perfectly. The amount of subsidence depends on the coupling between Nazca and South America plate and the slab pull (Section 5.3). It seems that the first 20 000 years are needed to reach a kind of equilibrium state due to the acting gravity. Therefore, the first 20 000 years should not be considered for interpretation of the results.

5.3 Effect of slap pull

Since phase transition is neglected in the models ridge push and slab pull are the driving mechanisms for subduction. The importance of slab pull is still a matter of discussion (Section 2.5). In the reference model the slab pull has the same amount as the east component of the ridge push (4.7 cm/a). For investigation of the effect of slab pull on the results one model without slab pull and one model with slab pull twice as high as ridge push were investigated and compared to the reference model.

The slab pull influences the deformation pattern of the model (Figure 5.5). A higher slab pull increases the compressional strain rate in the fore-arc region of the model and the extensional strain rate in the centre of the model increases, too (first row). In the Nazca plate the strain regime switch from compressional behaviour for no slab pull to extensional behaviour in case slab pull is higher than ridge push. When slab pull and ridge push are equal nearly no strain occurs in the oceanic plate. In the case of no slab pull uplift (red) occurs in the whole fore-arc region (row 2). A belt with subsidence rates of -2 to -4 mm/a (blue) can be seen 400 to 800 km away from the trench. In the northern part of the model the zone of subsidence starts further east due to the bending of the trench. When slab pull is equal to ridge push uplift remains only in the offshore fore-arc in the southern part of the model. The belt of subsidence broadens and shifts towards the trench reaching now from 200 to 700 km in the southern part. In the centre of the model is an area with less subsidence rates of -4 mm/a whereas in the northern and southern parts subsidence rates of -6 mm/a can be found. When slap pull is increased subsidence

increases. No uplift remains in the fore-arc region when slap pull is twice as high as ridge push. The displacement rate (velocity) in east direction increases with higher slab pull (row 3). For the black dot the values are 13.6 mm/a (no slab pull), 18.8 mm/a (slab pull = ridge push), and 20.6 mm/a (slab pull twice as high as ridge push). It can be summarized that higher slab pull increases extensional and compressional strain, causes larger subsidence, and increases displacement in east direction.

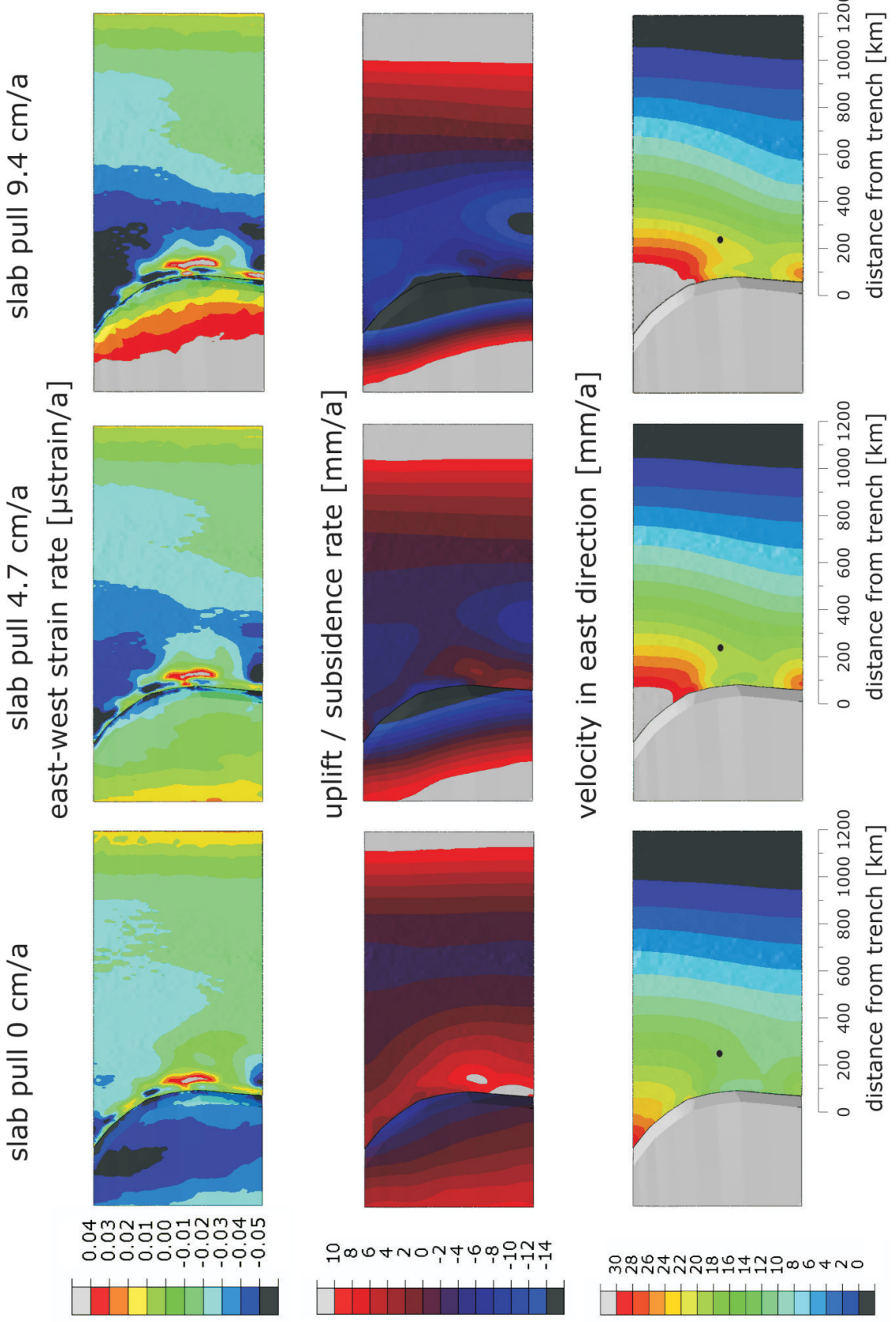

Figure 5.5: Comparison of models with slab pull rates of 0 cm/a (column 1), 4.7 cm/a (column 2), and 9.4 cm/a (column 3). Faster slab pull increases the strain rates (row 1), the subsidence rates (row 2), and the velocity in east direction (row 3).

5.4 Effect of mantle viscosity

5.4.1 Non-Newtonian viscosity in the uppermost continental asthenosphere

As in Section 3.1.4 described there are different creep behaviours in the earth. In this work the models have a linear (Newtonian) creep behaviour with a pre-exponential factor calculated after Equation 3.36 and the exponent n=1 (Diffusion creep). After *Babeyko and Sobolev* (2008) and *Kameyama et al.* (1999) deformation in the mantle is mainly accommodated by power law creep for typical geological strain rates ($10^{-15}s^{-1}$) and moderate temperatures (<1330°C; *Burov*, 2009). Diffusion creep becomes dominant at high temperatures or very low strain rates. Recent studies show that non-Newtonian upper mantle rheology is more consistent with seismic and laboratory data (e.g. *Billen and Hirth*, 2005; *Billen and Hirth*, 2007; *Andrews and Billen*, 2009).

To investigate the effect of power law creep (non-Newtonian) a model with power law behaviour in the uppermost continental asthenosphere (UCA) is compared to the reference model. The pre-exponential factor in case of power law can not be calculated after Equation 3.36. The relationship between strain rate ($\dot{\epsilon}$) and stress (σ) is

$$\dot{\epsilon} = A\sigma^n exp\left(-\frac{E_a}{RT}\right) \tag{5.1}$$

with A is a material parameter, E_a is the activation energy, R is the ideal gas constant (R=8.31451 J $K^{-1}mol^{-1}$), and T is the absolute temperature. From A and the exponent term a new pre-exponential factor $\tilde{A}$ has to be calculated. With A=4.89*10^6 s^{-1} MPa^{-n}, E_a=515 kJ mol^{-1} (*Hirth and Kohlstedt*, 1996) and an average temperature of 1100 C° (1373.15 K) for UCA we obtain $\tilde{A} = 1.26 * 10^{-34}$.

For the model discussed here the UCA has a non-Newtonian behaviour with $\tilde{A} = 1.26 * 10^{-34}$ and n=3.5. The rest of the asthenosphere behaves linear as in the reference model. Low values ($< 10^{-27}$) for the pre-exponential factor can lead to convergence problems in ABAQUS (*ABAQUS tutorial version 6.10*, 2010). A model with power law creep for the whole modelled asthenosphere did not run due to numerical problems. Figure 5.6 shows the east-west strain of the non-Newtonian model after 100 000 years as difference to the reference model (Section 5.1). This means, that the east-west strain of the reference model was subtracted from the result of the model with power law creep. Positive values indicate that the strain is higher than in the reference model, and negative values denote lower strain than in the reference model.

As expected the largest changes occur in the UCA with east-west strain values up to 500 μstrain higher as in the reference model (Figure 5.6 a). The UCA is shown in a perspective view only and all other units are hidden. Considering the crust the strain changes reach from -10 to 4 μstrain (Figure 5.6 b). In case of vertical displacement the difference in the crust lies between 1 and -2 m (not shown here). Power law creep has an impact on the UCA but has a small effect only on the crustal deformation. Therefore, it is sufficient for this work to consider a linear Newtonian creep process. For models with time span of some million years power law and other creep mechanisms seem to be more important (e.g. *Babeyko and Sobolev*, 2008; *Billen and Hirth*, 2005; *Billen and Hirth*, 2007).

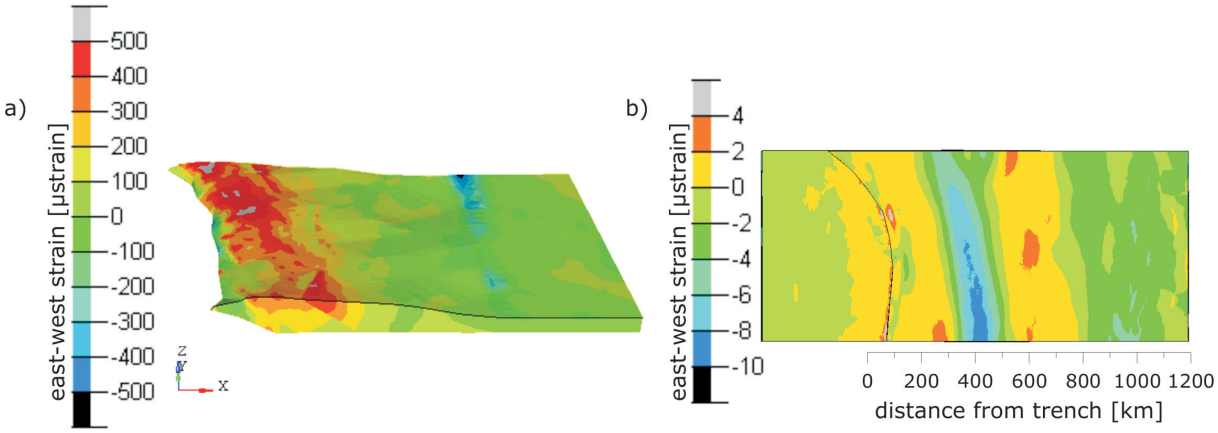

Figure 5.6: East-west strain for a model with nonlinear upper continental asthenosphere (UCA) viscosity: Shown is the difference to the reference model. a) Perspective view of the UCA only. The other model parts are hidden. b) Top view on the continental crust. Note that scales of pictures are different.

5.4.2 Variation of mantle viscosity

The effect of mantle viscosity on the crustal deformation is investigated by varying the viscosity of the asthenosphere. Either the viscosity of the uppermost continental asthenosphere (UCA) or the viscosity of the rest of the continental (CA) and the oceanic asthenosphere (OA) is changed in the models. For the UCA viscosities of 10^{19} Pa·s (reference model), 10^{20} Pa·s , and 10^{21} Pa·s are used. The viscosities investigated for CA and OA are 10^{20} Pa·s, $5*10^{20}$ Pa·s, 10^{21} Pa·s (reference model), $5*10^{21}$ Pa·s, and 10^{22} Pa·s.

In Figure 5.7 the east-west strain for the models is shown as difference to the reference model. Positive values mean strain are higher and negative values denote strain are lower than in the reference model. The expression "higher strain" is equal to the expression "lower compressional strain", because of the negative sign for compressional strain (Section 5). Figure 5.7 a) shows the variation of the asthenosphere viscosity and Figure 5.7 b) shows the results for varied UCA viscosity. The left column in Figure 5.7 a) presents models where viscosity is smaller than in the reference model, and in the right column the viscosity is higher than in the reference model. In Figure 5.7 b) both models have a higher UCA viscosity than the reference model.

A higher asthenosphere viscosity leads to higher east-west strain in the Longitudinal valley (LV), Precordillera (PC), Western Cordillera (WC), and Subandean region (SubA) (Figure 5.7 a). In the Subandean ranges decreasing the viscosity from 10^{21} Pa·s (reference model) to 10^{20} Pa·s results in strain changes between -100 and -150 μstrain. For a viscosity of 10^{22} Pa·s the strain changes are more than 250 μstrain (yellow belt) with values up to 750 μstrain in the northern part of the model. For this case the strain changes in the Precordillera are up to 1000 μstrain (red belt).

Other noticeable structures in Figure 5.7 a) can be seen in the oceanic crust. There is one long structure where strain increases with increasing viscosity and another structure near the bending where strain decreases with increasing viscosity. The second structure near the bending is also present at the continental crust but cannot be dissolved in the presented pictures. The structure near the bending could be either caused by the curvature of the trench or it is just an edge effect provoked by the border of the South American plate (black line).

In case of varied UCA viscosity the effect on strain is different (Figure 5.7 b). Here, an increased viscosity from 10^{19} Pa·s (reference model) to 10^{21} Pa·s results in less strain in the Western Cordillera with values up to ca. -500 μstrain. Positive strain differences can be noticed in the Eastern Cordillera. An increased viscosity of UCA results in lower strain (higher compressional strain) in the Western Cordillera whereas an increased viscosity of the rest of the asthenosphere leads to higher strain values (lower compressional strain) in the Precordillera and Western Cordillera.

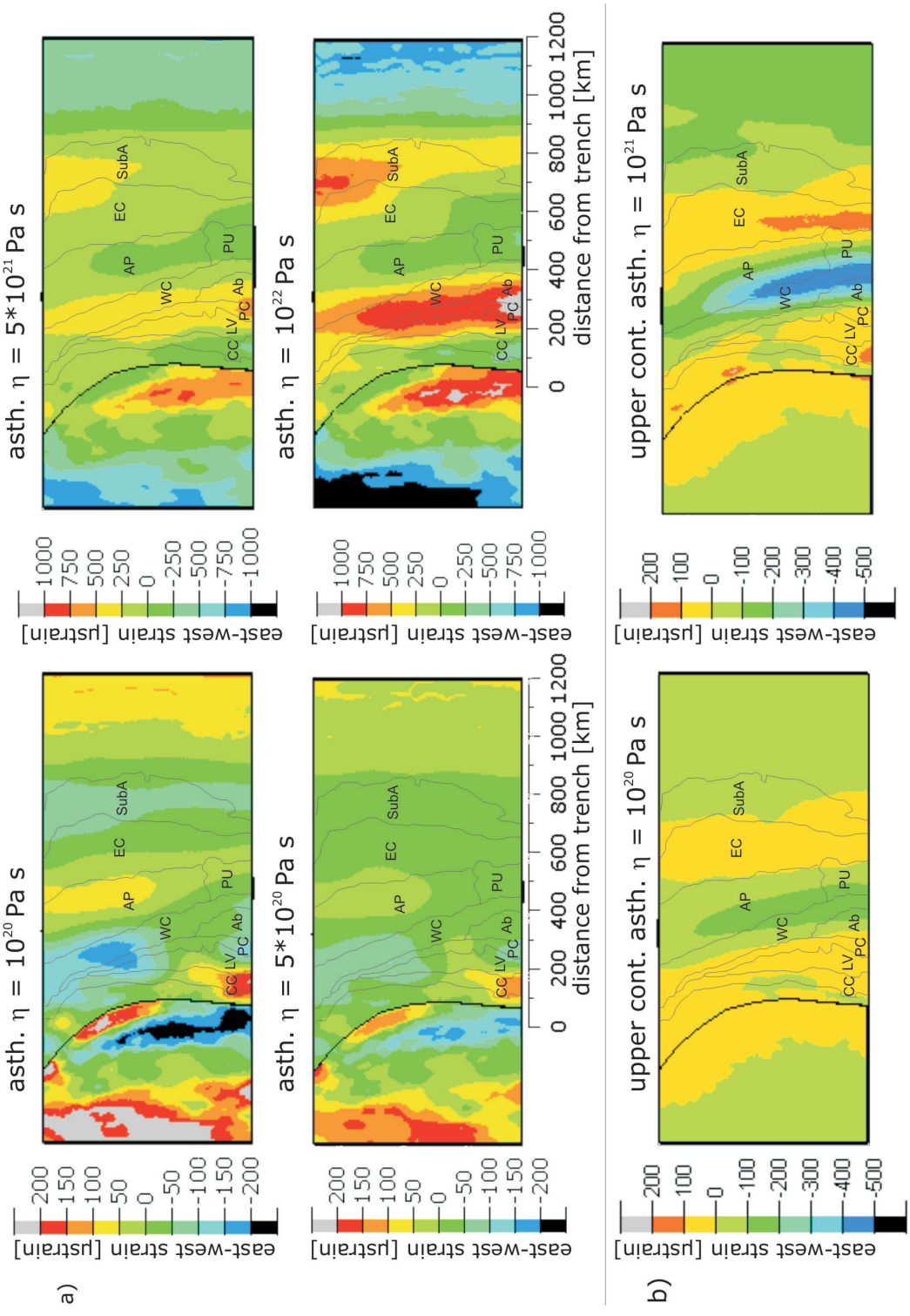

Figure 5.7: East-west strain after 100 000 years for models with different asthenosphere viscosities (a) and varied viscosities for the uppermost continental asthenosphere (UCA) (b): Shown are the differences to the reference model (asthenosphere η=10^{21} Pa·s and UCA η=10^{19} Pa·s). Negative values mean strain is lower in the shown model than in the reference model (higher compressional strain). Note that scales of pictures are different.

A similar investigation can be made considering the vertical displacements of the models with varied viscosities instead of strain. This is done in Figure 5.8. All results are shown as difference to the reference model. In Figure a) the vertical displacements are shown for varied asthenosphere viscosities. An increasing viscosity results in less subsidence (higher values). Regions which are most effected are the Precordillera and Western Cordillera. For the model with $\eta = 10^{22}$ Pa·s the uplift is up to 800 m (orange region) higher compared to the reference model with $\eta = 10^{21}$ Pa·s. In contrast, an increasing UCA viscosity results in less uplift in the Western Cordillera with values up to 100 m lower than in the reference model (Figure 5.8 b). In the Eastern Cordillera the uplift is up to 60 m higher than in the reference model. In Figure 5.8 c) the difference of velocity in east direction for the model with an ashthenosphere viscosity of 10^{22} Pa·s is shown. The differences to the reference model are ± 1.2 mm/a, which is within the error bars of the observed GPS measurements. For the other viscosities investigated in this work the changes in velocity are even smaller.

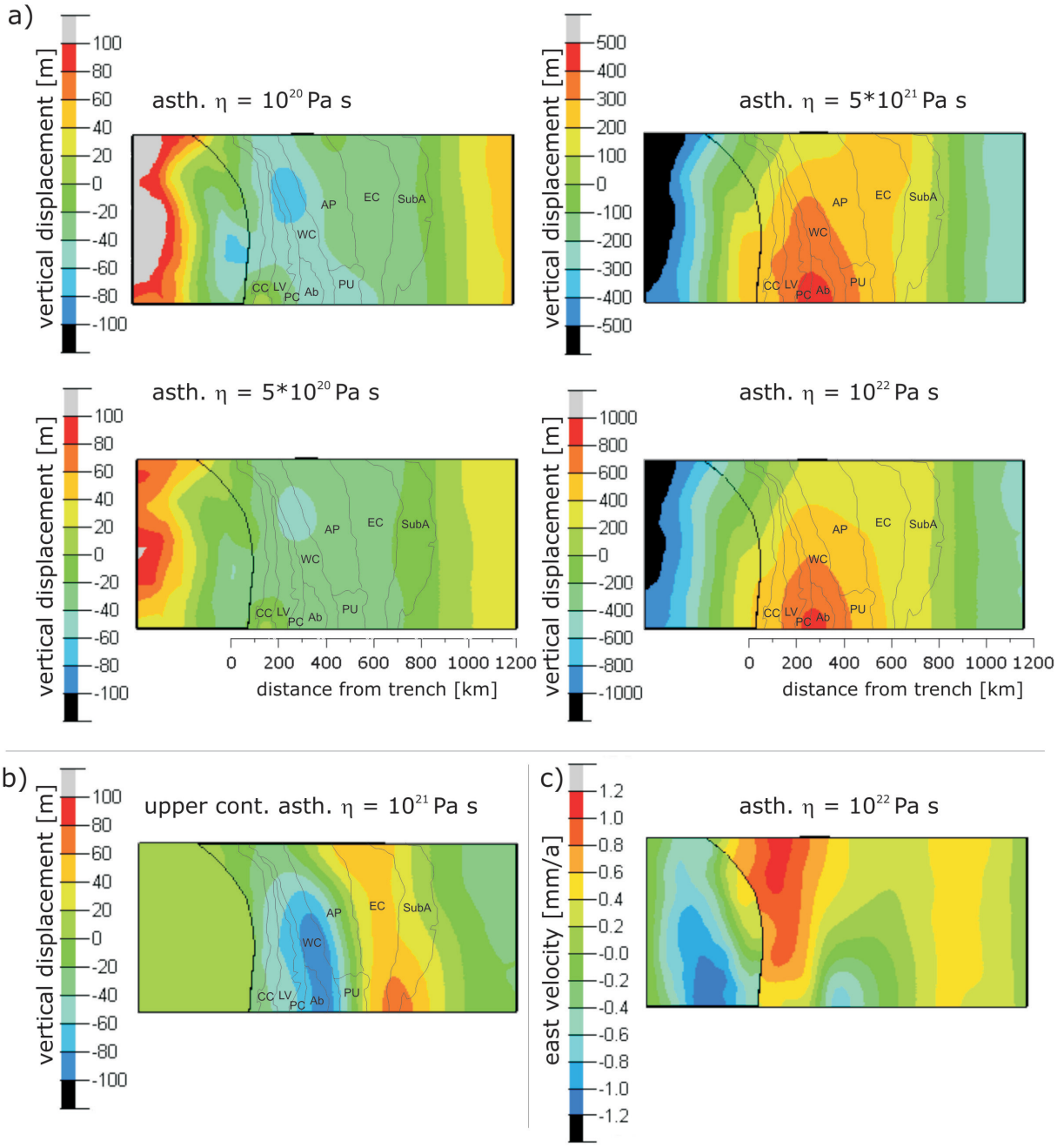

Figure 5.8: Vertical displacement for models with different asthenosphere viscosities a) and b): Shown is the difference to reference model. Note that pictures have different scales. c) Difference of east velocity for the model with η=10^{22} Pa·s. Changes are smaller than ±1 mm/a, which is within the error bars of the GPS observations.

5.5 Effect of viscous lithosphere

So far, all models presented in this work have a lithosphere with a pure elastic behaviour. Typical viscosities of the lithosphere are 10^{23} to 10^{24} Pa·s (*Ranalli*, 1995; *Turcotte and Schubert*, 2002). Assuming an average Young's modulus of 125 GPa for the lithosphere, a viscosity of 10^{23} Pa·s results in a Maxwell time about 64 000 years which is smaller than the running time of the models (100 000 years). Therefore, including a lithosphere viscosity of 10^{23} Pa·s should influence the deformation pattern. Higher viscosities result in Maxwell times much higher than the time span of the models and therefore elastic behaviour will be dominated in the lithosphere.

A model with the same parameters as the reference model and an additional lithosphere viscosity of 10^{23} Pa·s was created. The results compared to the reference model are shown in Figure 5.9. The total viscoelastic model shows in most parts lower east-west strain after 100 000 years (Figure 5.9 a). Compressional strain (negative values) increases which can be seen especially in the Precordillera, Western Cordillera, and the Subandean region. The extensional strain (positive values) decreases in the fore-arc region. An exception can be found in the Puna plateau where the east-west strain switches from a compressional to an extensional regime when viscosity for the lithosphere is included. A similar behaviour can be found in the horizontal shear strain component (Figure 5.9 b). The total viscoelastic model reveals lower extensional strain in the fore-arc but higher extensional strain in the region of the Atacama basin, Southern Western Cordillera, Southern Altiplano, and Puna plateau.

Figure 5.9 c) presents the uplift of the total viscoelastic model (right) as difference to the reference model (left) after 100 000 years. Including viscosity in the lithosphere increases the uplift in the fore-arc region. In the northern fore-arc the uplift is higher than in the southern part due to the curved trench. In the back-arc region the viscosity of the lithosphere reduces the uplift. In the Subandean region the uplift is up to 500 m lower than for the reference model.

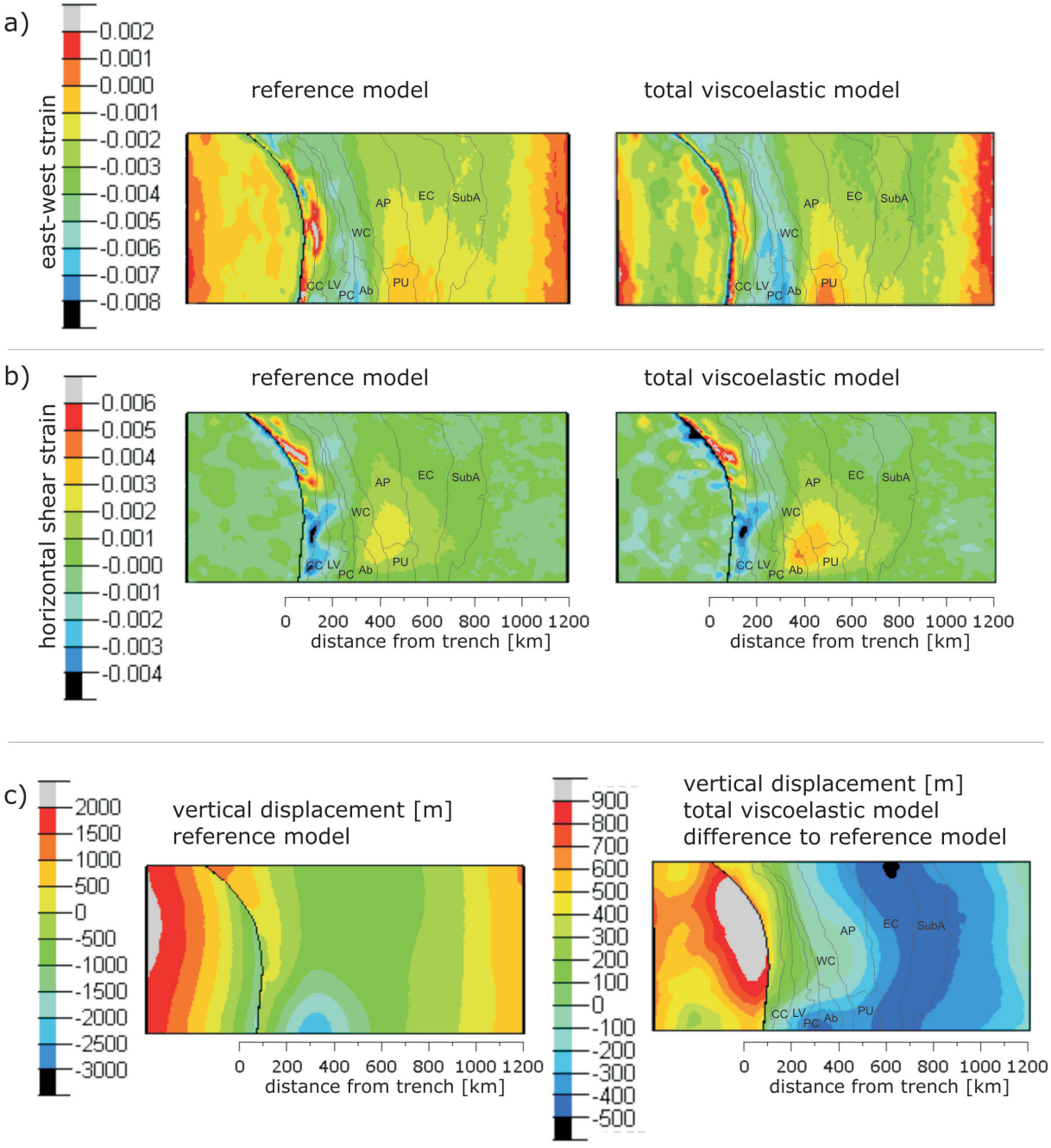

Figure 5.9: Effect of lithosphere viscosity on the deformation pattern: In most parts the east-west strain (a) and the horizontal shear strain (b) decreases for the total viscoelastic model. A viscoelastic lithosphere supports the uplift in the fore-arc and hinders the uplift in the back-arc (c).

5.6 Effect of upper continental crust rheology

As discussed in Section 3.1 there are different types of rheological behaviour. So far, pure elastic and viscoelastic behaviour were included in the presented models. Another important rheology is plasticity (Section 3.1.6) which plays a role commonly in the upper lithosphere. It is linked to earthquakes, faulting and folding. The brittle-ductile transition in the crust has an important bearing on the depth distribution of earthquakes, because most seismicity occurs in the brittle regime (*Ranalli*, 1995).

To test the effect of upper continental crust (UC) rheology three models were investigated (Figures 5.10, 5.11, and 5.12). All three models have a viscosity of 10^{23} Pa·s for the oceanic and continental lithosphere except UC and all other parameters are the same as in the reference model. The first model has a pure elastic UC. In the second model UC has additionally a viscosity of $\eta = 10^{23}$ Pa·s. In the third model Drucker Prager plasticity (Section 3.1.6) was additionally applied to the UC. Plasticity plays an important role in crustal deformation processes like earthquakes, faulting, and folding (*Ranalli*, 1995). The parameters used for implementing plasticity in the model are shown in Table 5.2.

Table 5.2: Parameter for plasticity in the upper continental crust.

parameter	value	reference
angle of friction ϕ	30°	(*Vermeer and de Borst*, 1984)
diletation angle ψ	10°	(*Vermeer and de Borst*, 1984)
cohesion C	30 MPa	(*Kennett and Bunge*, 2008)

Comparing the east-west strain of the three different models after 100 000 years running time reveals, that compressional strain (negative values) increases if viscosity or plasticity is included to the UC rheology (Figure 5.10 a). In case of an elastoplastic UC there is more compressional strain in the Precordillera and Western Cordillera than in case of a viscoelastic UC. The extensional strain in the region of the Puna plateau increases also when viscosity or plasticity is included, but the difference to the elastic model is higher in case of elastoplastic UC. Therefore, the plasticity parameters used here have stronger influence on the east-west strain than a viscosity of 10^{23} Pa·s. For example the difference of compressional strain in the Precordillera and Longitudinal valley to the elastic crust model is up to 0.001 for the viscoelastic case but up to 0.002 for the elastoplastic case. Figure 5.10 b) shows the uplift of the models with viscoelastic and elastoplastic UC after 100 000 years as difference to the model with an elastic UC. The uplift is hindered (negative values) in the fore-arc, arc region and in the Subandean region, but in later the effect is smaller than in the fore-arc. The uplift is higher (positive values) compared to the

model with pure elastic UC in the region of Altiplano and Puna plateau. In the Altiplano the uplift is up to 35 m higher in case of a viscoelastic crust. For an elastoplastic crust the uplift difference to the elastic crust model is even higher up to 50 m. Therefore, it can be summarized that viscosity as well as plasticity supports plateau uplift. However, like the east-west strain component plasticity affects the uplift more than viscosity. The reason might be that the elastic strain components play the major role for the viscoelastic crust model whereas in case of an elastoplastic crust the inelastic strain is the bigger part of total strain (Figure 5.11). Table 5.3 presents the maximum principal strain rates for

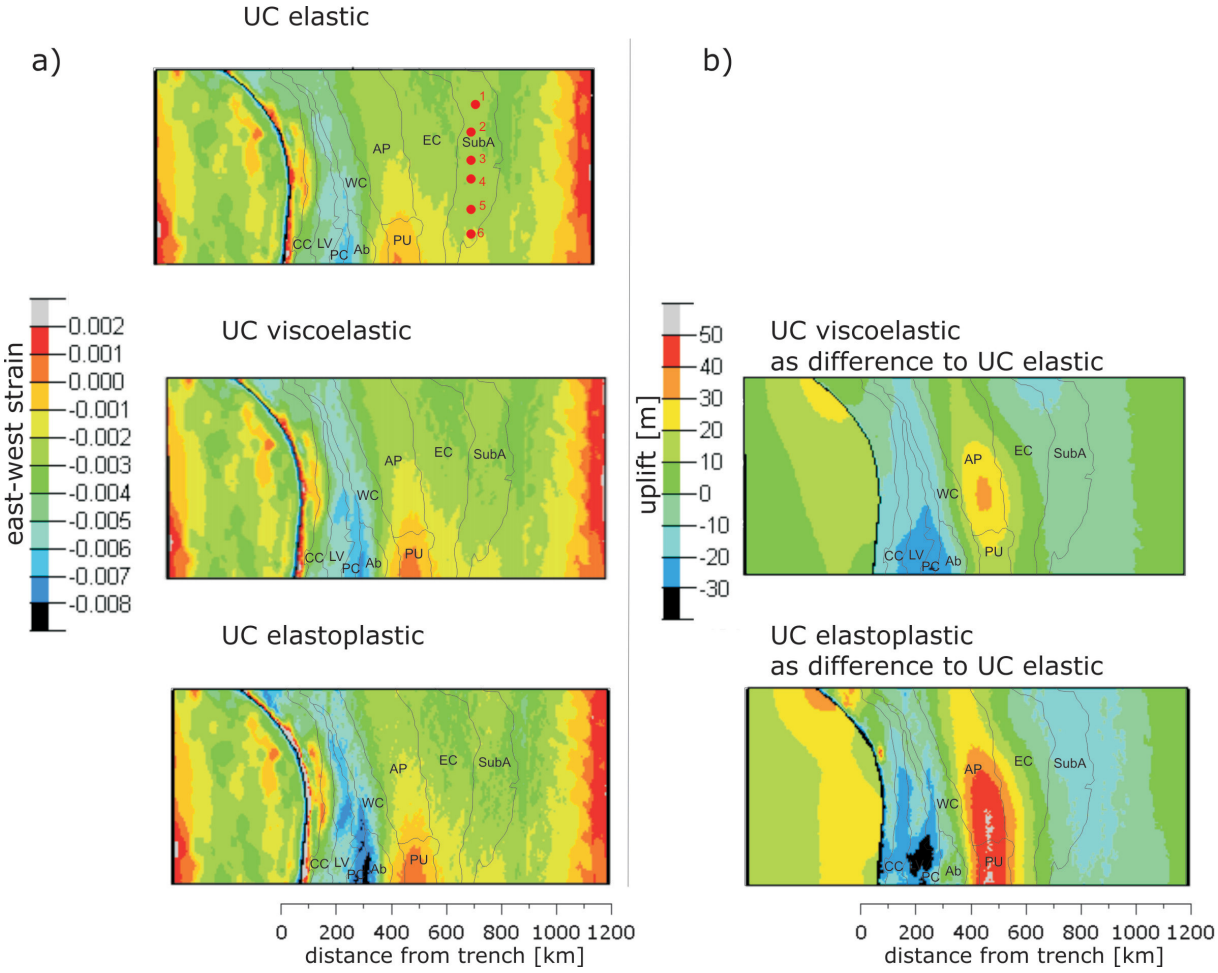

Figure 5.10: Effect of continental upper crust (UC) rheology on the east-west strain (a) and uplift (b): Including viscosity or plasticity increases the compressional east-west strain in the Precordillera and Western Cordillera. The uplift decreases in the fore-arc and Subandean region, but increases in the Altipano- and Puna plateau about 35 m (viscoelastic UC) or about 50 m (elastoplastic UC).

the models with different UC rheologies compared to the strain rates estimation of *Hindle et al.* (2002). The calculation was done for 6 points in the Subandean region which are marked in Figure 5.10. The differences towards the UC elastic model is bigger when

plasticity is included than for a viscoelastic crust. The calculated values fit the strain rates of *Hindle et al.* (2002) when the last 25 million years are considered. Estimations from GPS data or the last 10 million years only are higher by a factor of 1.5 than the calculated values.

Table 5.3: Calculated principal strain rates (P) and azimuths (A) for different continental crust rheology compared to the estimations of *Hindle et al.* (2002): The values are calculated for the red dots marked in 5.10 a).

	strain rates [μstrain/a] and azimuth [°]						estimated at 20°S (*Hindle et al.*, 2002)		
	UC elastic		UC viscoelastic		UC elastoplastic				
point	P	A	P	A	P	A		P	A
1	-0.024	87	-0.024	87	-0.021	85	GPS	-0.038	83
2	-0.025	82	-0.026	81	-0.026	80	10 Ma	-0.041	83
3	-0.026	83	-0.027	84	-0.029	83	25 Ma	-0.022	88
4	-0.024	75	-0.025	74	-0.028	72			
5	-0.025	74	-0.027	71	-0.032	67			
6	-0.022	81	-0.021	81	-0.020	84			

In case of elastoplastic behaviour the amount of inelastic deformation depends on the parameters of plasticity, especially on the yield strength (Section 3.1.6). For a viscoelastic behaviour the relation of elastic to inelastic deformation depends on the Maxwell time (Section 3.1.5). The elastic and inelastic part of the total east-west strain for an elastoplastic and a viscoelastic UC is presented in Figure 5.11), showing the results after 100 000 years. The scale for all pictures is the same and therefore the colours can be compared directly. In the elastoplastic model (Figure 5.11 a) the elastic strain reaches values of up to -0.02, but in most parts of the model the inelastic deformation (middle) plays the major role. However, in some parts of the Eastern Cordillera and the Subandean region the elastic and inelastic components of the east-west strain are nearly the same, denoted by the yellow coulor in the inelastic strain picture. The highest influence of inelastic strain can be found in the fore-arc region and Western Cordillera. This area starts to behave plastic in an early stage of modelling whereas the rest of the model remains longer elastic and starts inelastic behaviour later. In contrast to the elastoplastic model, for the model with a viscoelastic UC the elastic strain components play the major role (Figure 5.11 b). The Young's modulus for UC is 78 GPa and the viscosity is 10^{23} Pa·s. Therefore, the Maxwell time is slightly (about 1700 years) higher than the running time of the model and for this reason the elastic response dominates. Like in the elastoplastic model the fore-arc region and Western Cordillera show the highest amount of inelastic strain.

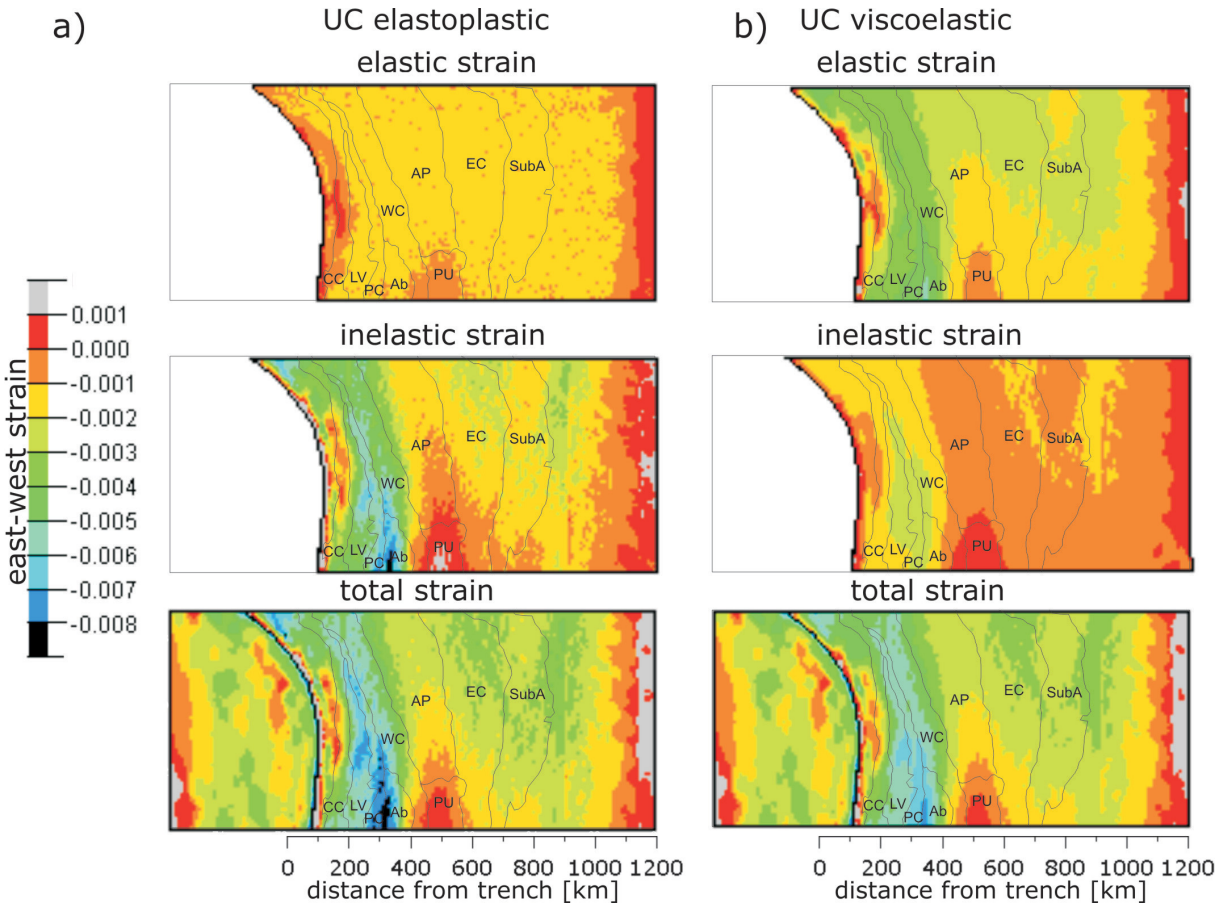

Figure 5.11: East-west strain for elastoplastic (a) and viscoelastic (b) upper continental crust: Elastic part (top), inelastic part (middle), and total strain (bottom) are shown. In the elastoplastic model the inelastic component dominates whereas the elastic component bestrides in the viscoelastic model.

Figure 5.12 presents the east displacement after 100 000 years (a) and the velocity in east direction (b) calculated from the last 5000 years of modelling time. The results of the model with viscoelastic UC (middle) and the elastoplastic model (bottom) are shown as differences to the model with a pure elastic UC (top). As in the east-west strain plasticity has a higher effect on the east displacement as viscosity. Highest differences to the elastic model can be found in the fore-arc region with values up to 100 m in case of viscoelasticity and values up to 150 m in case of an elastoplastic UC. Considering the east velocity (b) the differences to the model with elastic UC are between 2 and -1 mm/a and it is slightly higher for the model with elastoplastic UC. These values are within the range of the error bars of the observed GPS data (Figure 5.2 b).

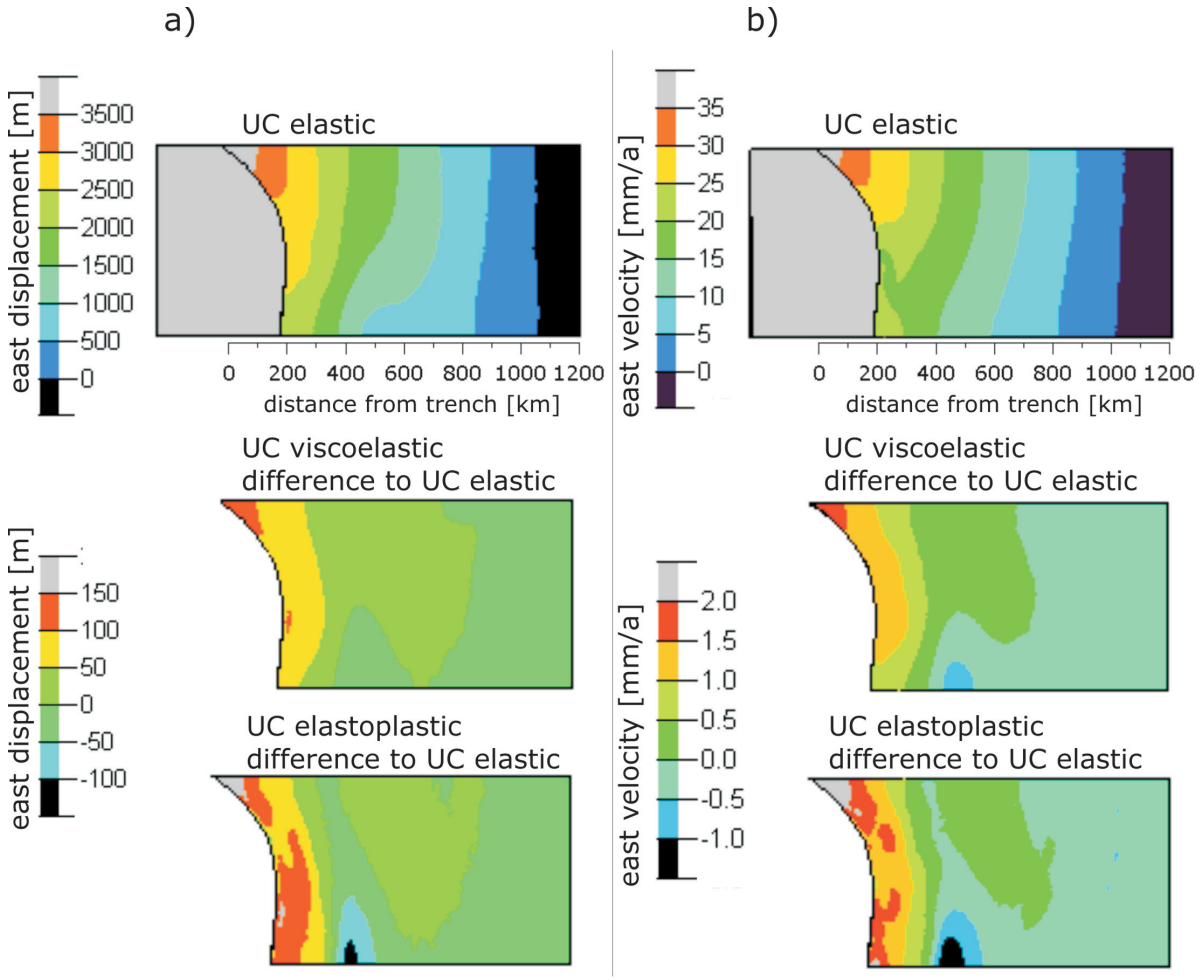

Figure 5.12: East displacement (a) and east velocity (b) for different upper continental crust rheologies: Results of the model with viscoelastic upper crust (middle) and elastoplastic crust (bottom) are presented as difference to the model with elastic upper crust (top). Differences in velocities are within the error bars of the GPS observations.

5.7 Effect of density of the upper continental crust

Density is a crucial parameter for dynamic modelling. In this work the densities were adopted from a well constrained density model (*Tassara et al.*, 2006). To investigate the sensitivity of the model results to the density two models were developed with different densities for the upper continental crust (UC). The results are compared to the reference model, which has a density of 2700 kg/m^3 and a Young's modulus of 78 GPa for the UC (Table 4.1). In one model the density of the reference model for the upper continental crust is increased and in another model the density is decreased by 50 kg/m^3 (Table 5.4). Because, Young's modulus and density are related to each other (Equation 3.16) the Young's modulus was changed, too. All other parameters are the same like in the reference model (Table 4.1).

Table 5.4: Density and Young's modulus for the upper continental crust for different models.

model	ρ [kg/m^3]	E [GPa]
reference model	2700	78
model in Figure 5.13 a)	2750	80
model in Figure 5.13 b)	2650	77

The results for the two models are shown as difference to the reference model in Figure 5.13. Negative sign means that values are lower and positive sign means that values are higher than in the reference model. In Figure 5.13 a) the results for the model with higher density are shown whereas Figure 5.13 b) present the results for the model with lower density than the reference model. First the results of the top row (a) will be discussed.

Increasing the density of UC by 50 kg/m^3 leads to lower east-west strain in the Coastal Cordillera (CC) in the centre of the model with values up to -120 μstrain (first picture in 5.13a). This is the region where the reference model shows extensional east-west strain with values up to 0.003 strain after 100 000 years (Figure 5.3 a). Therefore, higher density of UC reduces the extensional strain in the centre of the model. Lower east-west strain occurs in the Longitudinal valley (LV), the Western Cordillera (WC), and the Altiplano-Puna region (AP, PU), too. These are regions which show compressional regime (negative values) in the reference model (Figure 5.3 a), which leads to the conclusion that the compressional strain in these regions increase. The differences to the reference model in the Western Cordillera and Plateau region are larger in the southern part of the model which might be an effect of the trench geometry. In the Subandean region and further east the

presented strain values are positive, which means that they are higher than in the reference model. It can be conclude that the compressional strain in the Subandean region decreases up to 20 μstrain when the density of UC is increased by 50 kg/m^3.

Comparing the vertical displacements or uplift (second picture in 5.13a), reveal that an increased density for the UC results in lower uplift (larger subsidence) with values of $\sim$70 m (blue belt). The last picture in row a) shows that the changes in east displacement are gradual, increasing in the fore-arc and arc region, and decreasing in the Eastern Cordillera and Subandean region.

It can be summarized that a higher density of UC reduces the extensional strain in the fore-arc in the centre of the model, increases the compressional strain in the LV, WC and AP, and decreases the compressional strain in the Subandean region. It results in larger subsidence, increases the east displacement in the fore-arc and arc region, and decreases the east displacement in the Eastern Cordillera and Subandean region.

The pictures in figure 5.13 b) show the results of the model with a decreased density of UC by 50 kg/m^3. It is obvious that they show the opposite of the pictures in row a). Decreasing the density by the same amount like increasing it result in the same amount of values but with opposite signs. It can be conclude that a lower density of UC increases the extensional strain in the fore-arc and the compressional strain in the Subandean region, decreases the compressional strain in LV, WC, AP, PU, reduces subsidence (increases uplift), decreases east displacement in the fore-arc and arc region, and increases the east displacement in the Eastern Cordillera and Subandean region. This is in agreement with the conclusions derived from the pictures in row a).

This investigation reveals the importance of density for dynamic modelling. Here the density influence of one unit (UC) only was shown, but density is essential for every unit. Section 5.8 will show the bearing of density distribution in the slab. How many different units are implemented in the dynamic models depend on the knowledge of the parameters. It makes no sense to include lots of units if the parameters for these units are unknown. The simplest rheological behaviour is pure elastic but, even for this rheology knowing the density is crucial.

To define the units and densities for dynamic modelling well constrained density models derived from gravity measurements helps a lot. Well constrained density models derived from gravity measurements helps a lot to define the units and densities for the dynamic models. An improvement of density models by including more data (terrestrial and satellite data) will therefore improve the dynamic models. Including more and better

constraints from e.g. seismic profiles, boreholes, geophysic measurements, petrology, and geology will improve the density models also and indirectly the dynamic models.

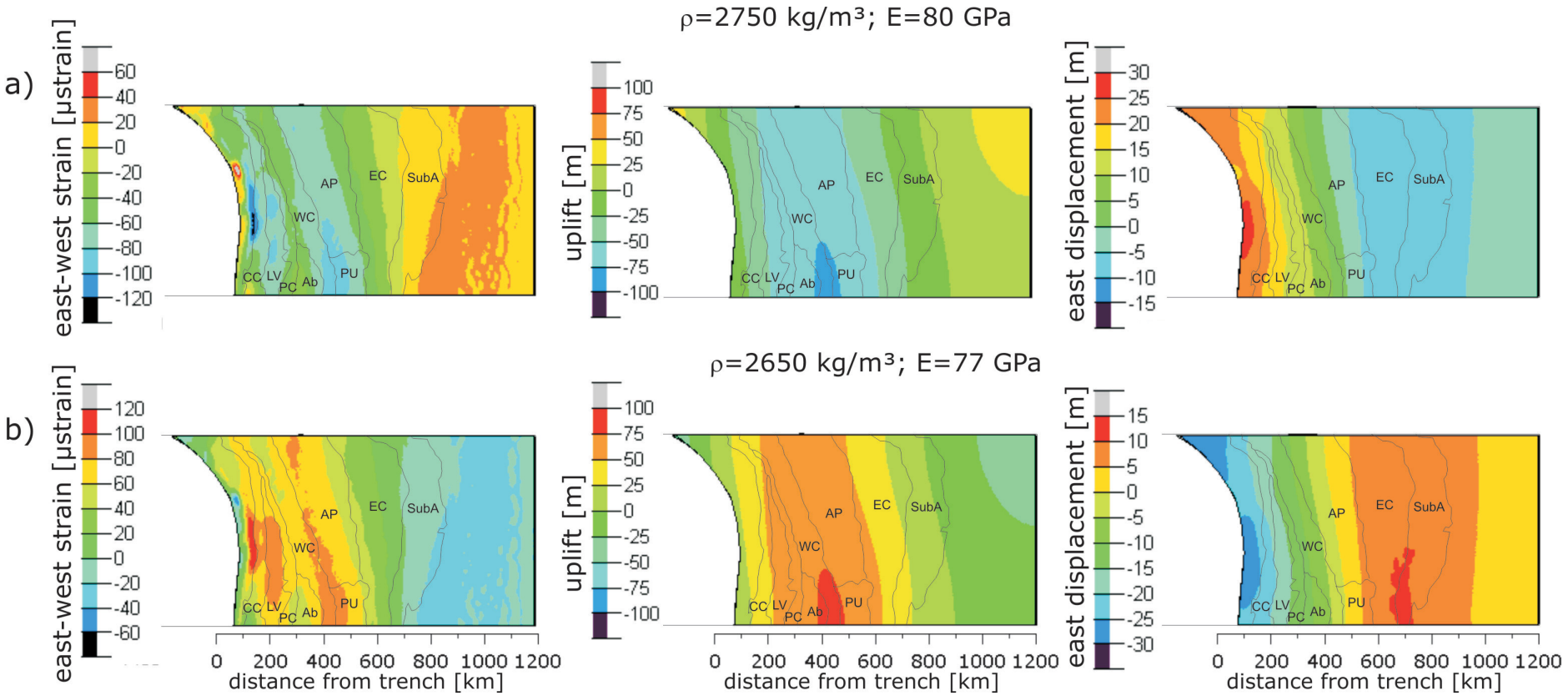

Figure 5.13: Effect of the density of the continental crust: a) Model results of a model with increased density and b) results of a model with decreased density. The results are shown as difference to the reference model.

5.8 Effect of homogeneous slab

In contrast to existing models (e.g. *Hampel and Pfiffner*, 2006; *Kellner*, 2007; *Babeyko and Sobolev*, 2008; *Bonnardot et al.*, 2008) the models of this work contain a slab which is divided into several parts with different densities and Young's moduli (Figure 4.3 and Table 4.1). With this distinction the increasing density with depth of the descending plate is considered.

To investigate the effect of slab parameters a model with homogeneous slab was created for comparison. The distinction in oceanic crust and lithospheric mantle remains but there is no longer a distinction with depth. As average density and Young's modulus the values of ρ=3300 kg/m^3; E=116 GPa for the oceanic crust and ρ=3400 kg/m^3; E=186 GPa for the lithospheric mantle were chosen. All other parameters are the same as in the reference model.

Figure 5.14 compares the east-west strain (a) and the uplift (b) of the reference model with the homogeneous slab model after 100 000 years model running time. The compressional strain in the Precordillera and Western Cordillera reaches values up to -0.007 in the reference model but only up to -0.005 in the model with homogeneous slab. However, the subsidence in the homogeneous slap model is lower. In Figure 5.14 c) the uplift difference of the homogeneous slab model to the reference model is presented. Negative values mean uplift is lower than in the reference model and positive values implicate that uplift is higher than in the reference model. In the area of Western Cordillera and Altiplano the uplift difference between the reference model and the model with homogeneous slab is up to 500 m. It can be summarized that a homogeneous slab reduces the compressional strain and increases the uplift of the model. However, the changing of parameters with depth is closer to reality than a homogeneous slab. The fact that the descending plate is cooler and denser than the surrounding asthenosphere arises the slab pull force (*Kennett and Bunge*, 2008). But, this is not given for the homogeneous slab model. *Bonnardot et al.* (2008) investigated the influence of slab asthenosphere density relation for a oceanward concave trench geometry. They conclude that a negative density contrast (slab is lighter than the asthenosphere) induces a fore-arc basin and that this fore-arc basin is amplified in case of a positive density contrast (slab is denser than the asthenosphere).

This investigation shows ones more how important the density is for dynamic modelling. Well constrained density models helps a lot to define the densities for dynamic models (Section 5.7).

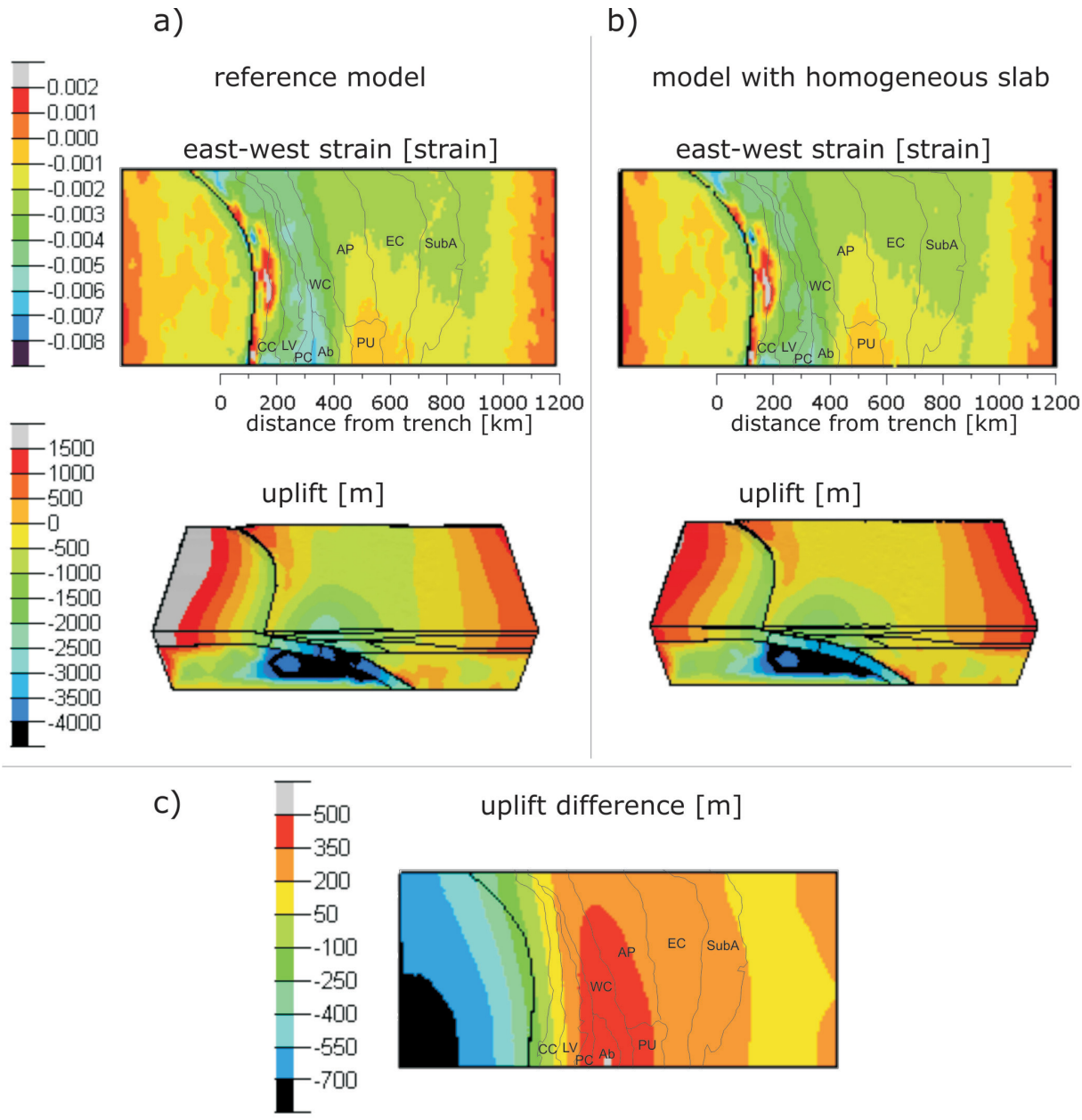

Figure 5.14: Comparison of east-west strain and uplift after 100 000 years between the reference model (a) and a model with homogeneous slab (b): The model with a homogeneous slab shows less compressional strain and higher uplift. The uplift difference between the models shows values up to 500 m and is highest in the region of the Western Cordillera (c).

5.9 The stress pattern on the Nazca plate

Up to now the main aspect of this study lied on the deformation patterns of the continental crust. Now, there will be a closer look at the stress distribution. As mentioned before the stress distribution on the oceanic plate has to be interpreted with care (Section 4.2.6). Therefore, the absolute magnitude of stress is not discussed here.

The world largest earthquakes occur in subduction zones, due to the frictional coupling between the subducting and overriding plate. Strong coupling leads to earthquakes with large magnitudes. The Central Andean margin is a region with large earthquakes, like the Antofagasta earthquake in 1995 with a magnitude of M_w 8.1, the Arequipa earthquake in 2001 with M_w 8.4, or the Toccopilla earthquake in 2007 with M_w 7.7 (*Schurr et al.*, 2012). The segment between approximately 18°S and 23°S broke last in 1877 in a large Magnitude M >8.5 earthquake and it is therefore considered to be most mature for rerupture (*Comte and Pardo*, 1991; *Schurr et al.*, 2012).

The hypocentres of moderate subduction earthquakes are located within the descending oceanic crust and they are an indicator to detect the slab surface. Therefore, the modelled stress pattern on the Nazca plate interface can be compared to the earthquake distribution in the investigation area (Figure 5.15). Shown are only earthquakes with magnitudes >5 taken from the USGS catalogue. The modelled von Mises stress (Equation 3.37) shows a pattern with stripes of higher stress and areas with lower stress (blue areas) between these stripes. There are regions where the stress accumulation fits quite well to the earthquake distribution. These areas are marked with black ellipses and letters. The high stress stripe including zone A, B, and C has a depth between 15 km and 50 km which is the zone where friction is applied to the dynamic models. This fits the hypocentre depth of the red and light blue dots in Figure 5.15 a). The stripe including zone D has a depth of circa 100 km and it is more noticeable in the southern part of the model. This feature correlates with the hypocentres of the dark green dots. Also more of these dots are in the southern part. For the next stripe in ca. 150 km depth there is no clear correlation to the earthquake distribution. Another area which can be correlated is zone E with a depth of ca. 170 km. In the stress accumulation picture there is a stripe from north to south whereas only in the southern part is a cluster of earthquakes (zone E). The focal mechanisms in Figure 5.15 c) reveal that most earthquakes are of normal type, and only some have strike slip components, which is common for subduction zones.

In the model results the areas with higher stress occur at areas where two or more model units with different parameters meet each other. It seems that these parameter changes cause the stress accumulation zones on the plate interface. May be earthquakes occur

where material parameters in the slab show steep gradients. The stress accumulation near the bottom of the model might be an edge effect caused by the nearby bottom of the model. A finer mesh for the descending slab is necessary to say more about the correlation between stress and earthquake occurrence. Temperature and pressure dependent material parameters instead of fixed borders where material changes, will avoid a discontinuous behaviour at these boundaries. However, zones of stress accumulation at the plate interface matches to the regions with higher earthquake distribution, which shows that it is general possible to link stress on the Nazca plate interface with the earthquake distribution in the Central Andes region.

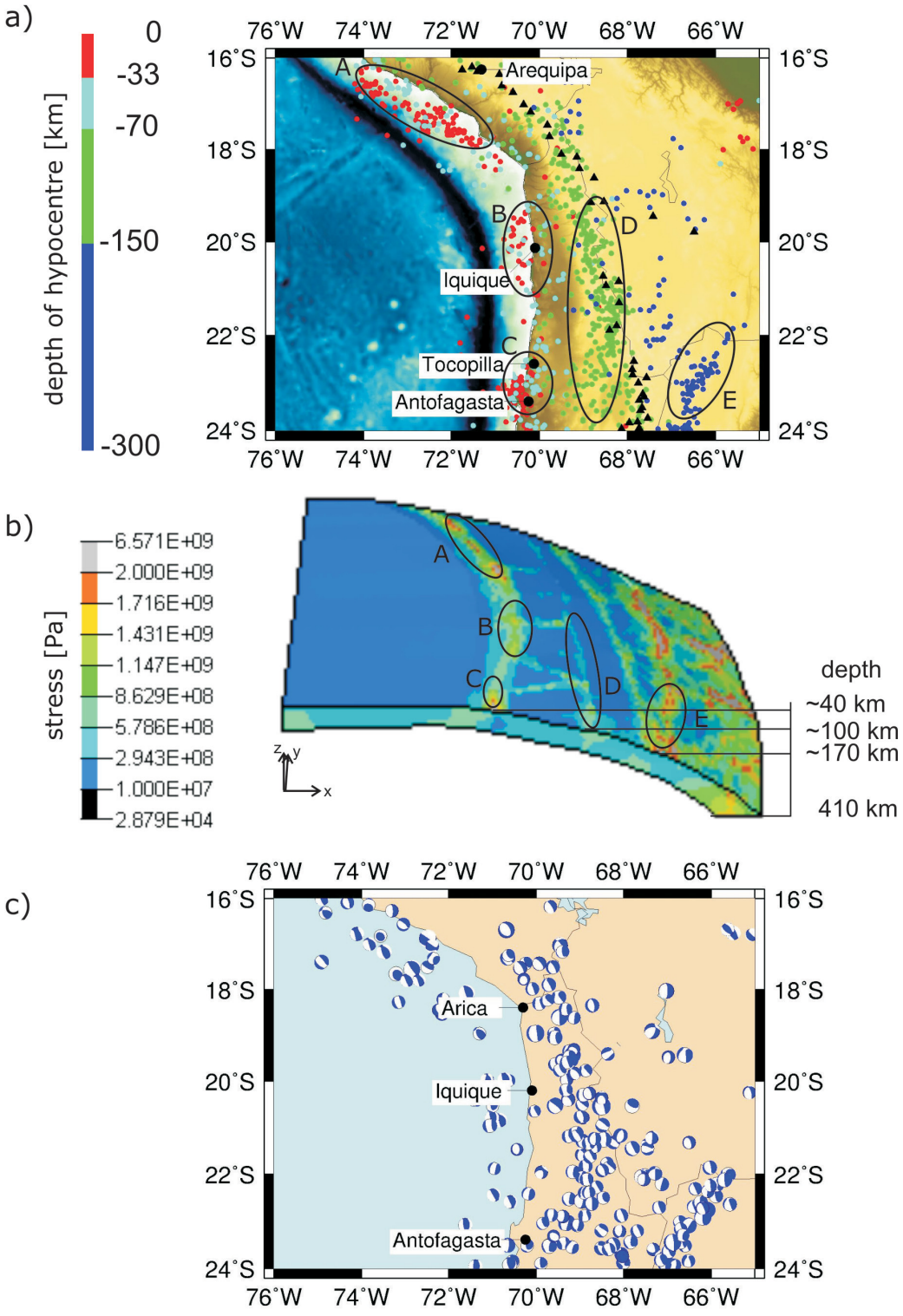

Figure 5.15: Comparison of earthquake distribution (USGS) in the investigation area (a) and stress accumulation on the Nazca plate interface (b). Regions with higher stress correlate with areas where earthquakes accumulate. Focal mechanisms reveal that most earthquakes are of normal type (c).

5.10 The stress pattern on the continental crust

The World Stress Map (WSM) provides information on the maximum horizontal stress orientation gained from a wide range of stress indicators (*Heidbach et al.*, 2008a; *Heidbach et al.*, 2008b). In the investigation area of this work 24 stress orientations estimated from focal mechanisms, borehole breakouts, and geological indicators are available in the WSM database. The reliance of the WSM data are classified in different types (A, B, C, D, E), where the uncertainties are small for data of type A and large for data of type E. Most data used in the Central Andean region are of quality type C, which means that the uncertainties in the azimuths are within ±25° (*Heidbach et al.*, 2008a; *Heidbach et al.*, 2008b). Figure 5.16 compares the stress orientations of the WSM data (red) with the horizontal stress directions calculated from the modelled results (black). Within the uncertainties the orientations fit quite well in the Subandean region. In the coastal region the deviation of modelled and WSM directions is higher, but even the WSM data show big differences in their orientations. It seems that there are more local stress variations in the coastal area than in the Subandean region. Unfortunately there are no WSM data in the Western Cordillera or plateau region. The agreement between modelled and observed stress orientations show that the models are a good description of the dynamic in the Central Andean region.

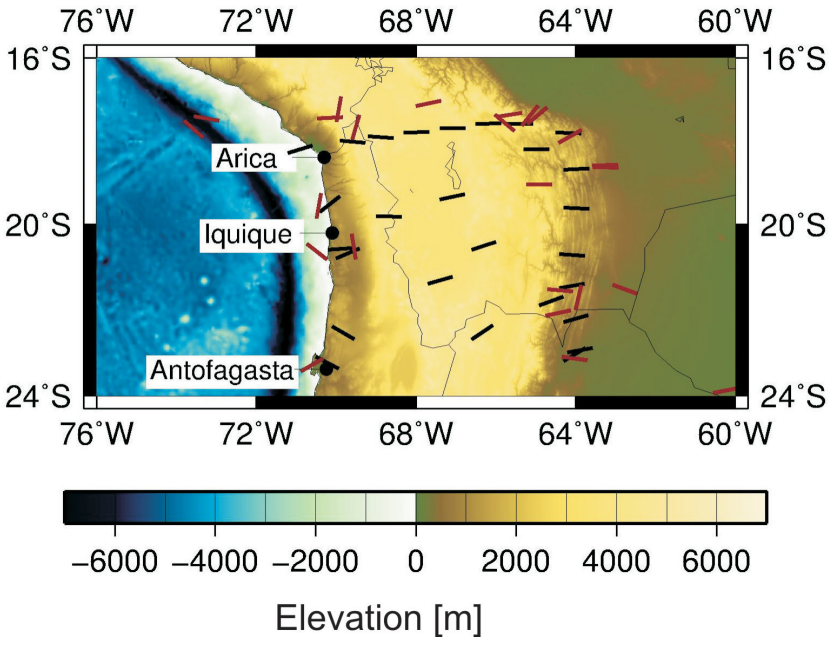

Figure 5.16: Maximum horizontal stress directions of the reference model (black) compared to the stress orientations of the World Stress Map (red) (*Heidbach et al.*, 2008b)

6 Conclusions and future research

The investigation and understanding of subduction zone processes were an interest of research over a long time, and still there are unsolved riddles. One of the worldwide prominent subduction zones is the margin of the Central Andes with its unique concave trench curvature, which was chosen as investigation area of this work. Due to the fact that subduction is a complex process not all aspects could be taken into account for the modelling. However, some main conclusions and advices for further modellings can be derived from the results of this study.

The geometry and densities of the dynamic models are based on the geometry and densities of a well constrained density model, which fits quite well to the measured gravity field. Therefore, the developed dynamic models have a most realistic geometry describing a real existent location, here the subduction zone of South America in the region of the Central Andes. The modelled results fit quite well to geodetic and geological observations:

- The east velocity of the models fits to the GPS measurements of *Kendrick et al.* (2001).
- The strain rates in the Subandean fits to the strain rates estimated from geological observations by *Hindle et al.* (2002).
- The stress pattern on the plate interface correlates with the earthquake distribution.
- The modelled stress orientation matches to the stress directions from the World Stress Map by *Heidbach et al.* (2008b).

This good agreements with other results show that the developed models are a successful numerical description of the Central Andean region and that taking a density model as basis is an excellent approach for dynamic modelling. Density models are a good possibility to define the geometry and the densities of the dynamic models. The dynamic models of this work with theire rheological parameters and boundary conditions explain the observed geological, geodetical, and geophysical data.

Including or neglecting the gravitational force has an influence on the model results. Because it is a fundamental force which should be considered for dynamic modelling. Unfortunately including gravity leads to a running in behaviour at the beginning of modelling

time. This has to be considered for trend calculation. Corresponding to the expectation gravity induces subsidence.

The amount of slab pull is still a matter of debate. The results presented here show that an increased slab pull leads to more compressional strain, to higher east velocity but also to higher subsidence rates.

Due to the different convergence velocities of the oceanic plate caused by trench curvature the trench geometry has an important influence on the deformation patterns in the continental crust, which is consistent with the results of *Bonnardot et al.* (2008), *Boutelier and Oncken* (2010) and *Gassmöller* (2011). These authors investigated the influence of concave and convex trench geometries in a general way. The models in this thesis present especially the trench of the Central Andean margin. The results show for the oceanward concave curved trench region, where the convergence velocity is nearly perpendicular to the trench, subsidence rates of -5 to -9 mm/a in the fore-arc. In contrast in the model parts where the trench is straight and the convergence velocity has an obliquity of 20° the fore-arc region shows uplift rates of 2 to 4 mm/a. The horizontal strain is also influenced by the trench curvature with higher compressional east-west strain in the arc-region (Precordillera and Western Cordillera) for the model part with straight trench. The horizontal shear strain shows compression in the straight trench area and extension in the concave curved trench area.

Variations of the asthenosphere viscosity show that this is an important parameter controlling the deformation in the crust. For example in the Subandean region a viscosity of 10^{22} Pa·s results in strain changes of more than 250 μstrain compared to a model with viscosity of 10^{21} Pa·s.

The rheological behaviour of the crust controls the crustal deformation. Including viscosity or plasticity in the crust leads to higher compressional strain in the Precordillera and Western Cordillera, to lower uplift in the fore-arc region and Subandean and to higher uplift in the Altiplano- and Puna plateau. The effect of plasticity is higher than the influence of viscosity. In case of an elastoplastic crust the inelastic components of strain bestride whereas in case of a viscoelastic crust the elastic strain components are dominant. For the short running time of 100 000 years crustal viscosity with values in the range 10^{23} Pa·s or higher plays a minor role but for longterm investigations viscosity becomes more important.

This work shows how important the density is for dynamic modelling. Knowing the density for the different units is essential even in the simplest rheological behaviour which

is pure elastic. Well constrained density models derived from gravity measurements helps a lot to define the units and densities for the dynamic models. An improvement of density models by including more data (terrestrial and satellite data) and more and better constraints (e.g. geophysic, petrology, and geology) will improve the dynamic models.

Due to metamorphic reactions the descending slab densifies with depth which is considered in most of the models in this work. It is discussed that the fact that the descending plate is cooler and denser than the asthenosphere arises the slab pull force (*Kennett and Bunge*, 2008). The densities for the model are taken from the density model, which fits well to the observed gravity measurements. In the lower part the slab is denser than the surrounding asthenosphere. A dynamic model with homogeneous slab, which is lighter than the asthenosphere, shows lower compressional strain and increases the uplift. But, this density distribution will not match the gravity observations as good as the model with inhomogeneous slab.

Due to the high coupling between the subducting and overriding plate the world largest earthquakes occur in subduction zone regions. The hypocentres of the moderate earthquakes are located within descending oceanic crust and are an indicator to detect the slab surface. The model results show that the stress pattern on the plate interface of the Nazca plate correlates with the earthquake distribution in the investigation area.

The main results and conclusions following from the results can be summarized as:

- The model results are in good agreement with other geodetic and geological observations and therefore they are a well numerical description of the processes of the Central Andean subduction zone region.

- Taking the geometry of a well constrained density model for dynamic modelling is a successful approach to get a realistic geometry, which describes a real existent location.

- As expected, the amount of slab pull is important for the results.

- The trench geometry has an influence on the crustal deformation and should be included in subduction zone models. In case of the Central Andes the concave curved trench is important to consider.

- Asthenosphere viscosity controles the deformation pattern in the continental crust.

- The rheological behaviour of the continental crust controls the deformation pattern. An elastoplastic behaviour has more influence than an viscoelastic behaviour for

a modelling time of 100 000 years. Therefore plasticity should be included for the crust. For longterm investigations also viscosity is important.

- Density is important for dynamic modelling and well constrained density models are a good possibility for defining densities.
- The density distribution of the slab influences the deformation pattern in the crust. An inhomogeneous slab which becomes denser with depth is closer to reality than a homogeneous slab density.
- The stress distribution at the plate interface of the descending Nazca plate shows good correlation with the earthquake distribution in the investigation area. Further modelling with the main aspect on the plate interface might therefore be helpful to investigate earthquakes caused by subduction.

There is still a lot of work to do in order to learn more about subduction zones. This work investigates some aspects and shows for example how important the trench geometry and the viscosity of the asthenosphere are. From this results some advises for future research on subduction zone modelling can be derived. Most parameters used for the models are temperature dependent e.g. density, Young's modulus, viscosity. This is considered in this work by the division in several units with different parameters. However, including a 3D temperature model and link the parameters with it will be more precise. It is shown that the asthenosphere viscosity influences crustal deformation. Obviously, the asthenosphere plays an important role. Therefore, mantle convection processes linked to temperature should be considered. Furthermore, the coupling between lithosphere and asthenosphere is not well understood and might be a future research topic. It is known that fluids play a role for melting processes within the mantle wedge and for volcanism. Including fluids will also influence the frictional behaviour between the oceanic and continental plates. The stress distribution on the plate interface correlates with the earthquake distribution. A further investigation of this correlation can be made by models concentrating mainly on the slab interface with a finer mesh of the slab. The coupling between the subducting and overriding plate is an important aspect which was not discussed in this work but should be further investigated. In a separate work within the IMOSAGA project frictional coupling and parameters like friction coefficient and width of coupling zone will be one of the main interests of investigation (Sharma, in prep.).

For the first time it was shown that taking a well constrained density model as basis for the dynamic models is an excellent approach for dynamic modelling. Including satellite-derived gravity data will improve the density models. They fill gaps in regions where no terrestrial gravity measurements exist and are suitable to constrain the deep structures of the models. The new satellite missions GRACE and GOCE significantly improve the

coverage and availability of gravity data. Satellite only models have lower spatial resolution than the terrestrial data but, combined models using terrestrial and satellite-derived gravity data will improve the density models and indirectly the dynamic models.

References

ABAQUS tutorial version 6.10 (2010), Dassault Systèmes Simulia Corp., Providence, RI, USA http://abaqus.civil.uwa.edu.au:2080/v6.10/index.html.

Alvers, M. R., S. Schmidt, H.-J. Götze, and C. Fichler (2010), IGMAS+ Software for 3D Gravity, FTG and Magnetic Modeling towards semantic constraints, in *EGM 2010 International Workshop: Adding new value to Electromagnetic, Gravity and Magnetic Methods for Exploration. Capri, Italy, April 11-14, 2010.*

Amante, C., and B. W. Eakins (2009), ETOPO1 1 Arc-Minute Global Relief Model: Procedures, Data Sources and Analysis, *NOAA Technical Memorandum NESDIS NGDC-24*, p. 19.

ANCORP Working Group (1999), Seismic reflection image revealing offset of Andean subduction-zone earthquake locations into oceanic mantle, *Nature*, *397*, 341–344.

ANCORP Working Group (2003), Seismic imaging of a convergent continental margin and plateau in the central Andes (Andean Continental Research Project 1996 (ANCORP'96)), *J. Geophys. Res.*, *108*(B7), 2328, doi:10.1029/2002JB001771.

Andersen, O. B., and P. Knudsen (1998), Global marine gravity field from the ERS-1 and Geosat geodetic mission altimetry, *J. Geophys. Res.*, *103*(C4), 8129–8137, doi: 10.1029/97JC02198.

Andrews, E. R., and M. I. Billen (2009), Rheologic controls on the dynamics of slab detachment, *Tectonophysics*, *464*, 60–69, doi:10.1016/j.tecto.2007.09.004.

Antonioli, A., A. Piersanti, and G. Spada (1998), Stress diffusion following large strike-slip earthquakes: A comparison between spherical and flat-earth models, *Geophys. J. Int*, *133*, 85–90.

Artyushkov, E. V. (1983), *Geodynamics*, Elsevier, Amsterdam.

Babeyko, A. Y., and S. V. Sobolev (2008), High-resolution numerical modeling of stress distribution in visco-elasto-plastic subducting slabs, *Lithos*, *103*, 205–216, doi: 10.1016/j.lithos.2007.09.015.

Babeyko, A. Y., S. V. Sobolev, T. Vietor, O. Oncken, and R. B. Trumbull (2006), Numerical Study of Weakening Processes in the Central Andean Back-Arc, In: Oncken, O., Chong, G., Franz, G., Giese, P., Götze, H.-J., Ramos, V. A., Strecker, M. and Wigger, P. (eds.) The Andes: Active subduction orogeny, *Frontiers in Earth Science Series*, pp. 495–512.

Barnes, J., and T. Ehlers (2009), End member models for Andean Plateau uplift, *Earth Science Reviews*, *97*, 105–132.

Barrel, J. (1914), The strength of the Earth's crust, *Journal of Geology*, *22*, 28–48.

Bevis, M., E. Kendrick, R. Smalley, B. Brooks, R. Allmendinger, and B. Isacks (2001), On the strength of interplate coupling and the rate of back arc convergence in the central Andes: An analysis of the interseismic velocity field, *Geochem. Geophys. Geosyst.*, *2(11)*, 1067, doi:10.1029/2001GC000198.

Billen, M. I. (2008), Modeling the Dynamics of Subducting Slabs, *Annu. Rev. Earth Planet. Sci.*, *36*, 325–356, doi:10.1146/annurev.earth.36.031207.124129.

Billen, M. I., and G. Hirth (2005), Newtonian versus non-Newtonian upper mantle viscosity: Implications for subduction initiation, *Geophys. Res. Lett.*, *32*, L19,304, doi:10.1029/2005GL023457.

Billen, M. I., and G. Hirth (2007), Rheologic controls on slab dynamics, *Geochem. Geophys. Geosyst.*, *8*(8), Q08,012, doi:10.1029/2007GC001597.

Bird, P. (2003), An updated digital model of plate boundaries, *Geochem. Geophys. Geosyst.*, *4*, 1027, doi:1010.1029/2001GC000252.

Bonnardot, M.-A., R. Hassani, E. Tric, E. Ruellan, and M. Régnier (2008), Effect of margin curvature on plate deformation in a 3-D numerical model of subduction zones, *Geophys. J. Int*, *173*, 1084–1094, doi:10.1111/j.1365-246X.2008.03752.

Boutelier, D., and O. Oncken (2010), Role of the plate margin curvature in the plateau buildup: Consequences for the central Andes, *J. Geophys. Res.*, *115*, B04,402, doi:10.1029/2009JB006296.

Buiter, S. J. H., A. Y. Babeyko, S. Ellis, T. V. Gerya, B. J. P. Kaus, A. Kellner, G. Schreurs, and Y. Yamada (2006), The numerical sandbox: Comparison of model results for a shortening and an extension experiment, In: Buiter, S. J. H. and Schreurs, G. (eds.) Analogue and Numerical Modelling of Crustal Scale Processes, *Geological Society, London, Special Publication*, *253*, 29–64.

Bunge, H.-P. (2005), Low plume exess temperature and high core heat flux inffered from non-adiabatic geotherms in internally heated mantle circulation models, *Phys. Earth Planet. In.*, *153*, 3–10.

Burov, E. (2009), Plate Rheology and Mechanics, In: Schubert, G. and Watts, A. B. (eds.) Crust and Lithosphere Dynamics, *Treatise on Geophysics*, *6*, 99–151.

Comte, D., and M. Pardo (1991), Reappraisal of Great Historical Earthquakes in the Northern Chile and Southern Peru Seismic Gaps, *Natural Hazards*, *4*, 23–44.

Cruciani, C., E. Carminati, and C. Doglioni (2005), Slab dip vs. lithospere age: no direct function, *Earth Planet. Sci. Lett.*, *238*, 298–310.

DeMets, C. (1995), Plate motions and crustal deformation, *Rev. Geophys.*, *33*, 365–369.

DeMets, C., R. G. Gordon, D. F. Argus, and S. Stein (1990), Current plate motions, *Geophys. J. Int*, *101*, 425–478.

Dietz, R. S. (1961), Evolution by spreading of the sea floor, *Nature*, *190*, 854.

Doglioni, C., E. Carminati, M. Cuffaro, and D. Scrocca (2007), Subduction kinematics and dynamic constraints, *Earth Science Reviews*, *83*, 125–175.

Drucker, D. C., and W. Prager (1952), Soil Mechanics and Plastic Analysis or Limit Design, *Quarterly of Applied Mathematics*, *10*(2), 157–165.

Dumont Weltatlas (2003), 337 pp., DuMont Reiseverlag, Köln.

Eisbacher, G. H. (1996), *Einführung in die Tektonik*, 374 pp., Ferdinand Enke Verlag.

Elger, K., O. Oncken, and J. Glodny (2005), Plateau-style accumulation of deformation: Southern Altiplano, *Tectonics*, *24*, TC4020, doi:10.1029/2004TC001675.

Fischer, K. D. (2006), The influence of different rheological parameters on the surface deformation and stress field of the Aegean-Anatolian region, *Int. J. Earth Sci. (Geol. Rundsch)*, *95*, 239–249, doi:10.1007/s00531-005-0031-0.

Förste, C., R. Shako, F. Flechtner, C. Dahle, O. Abrykosov, K.-H. Neumayer, F. Barthelmes, R. König, S.-L. Bruinsma, J.-C. Marty, J.-M. Lemoine, G. Balmino, and R. Biancale (2012), A new release for EIGEN-6 - the latest combined global gravity field model including LAGEOS, GRACE and GOCE data from the collaboration of GFZ Potsdam and GRGS Toulouse, in *General Assembly European Geosciences Union (Vienna, Austria 2012).*

Forsyth, D., and S. Uyeda (1975), On the Relative Importance of the Driving Forces of Plate Motion, *Geophys. J. R. astr. Soc.*, *43*, 163–200.

Gassmöller, R. (2011), Spannungs- und Deformationsverteilung an gebogenen Subduktionszonen, Ph.D. thesis, Friedrich-Schiller-Universität Jena.

Gebauer, A., H. Steffen, C. Kroner, and T. Jahr (2010), Finite element modelling of atmosphere loading effects on strain, tilt and displacement at multi-sensor stations, *Geophys. J. Int*, *181*(3), 1593–1612, doi:10.1111/j.1365-246X.2010.04549.x.

Giese, P., E. Scheuber, F. Schilling, M. Schmitz, and P. Wigger (1999), Crustal thickening processes in the Central Andes and the different natures of the Moho-discontinuity, *Journal of South American Earth Sciences*, *12*, 201–220, doi: 10.1016/S0895-9811(99)00014-0,.

Götze, H.-J., and S. Krause (2002), The Central Andean gravity high, a relic of an old subduction complex?, *Journal of South American Earth Sciences*, *14*(8), 799–811, doi: 10.1016/S0895-9811(01)00077-3.

Götze, H.-J., and B. Lahmeyer (1988), Application of three-dimensional interactive modeling in gravity and magnetics, *Geophysics*, *53*(8), 1096–1108, doi:10.1190/1.1442546.

Götze, H.-J., B. Lahmeyer, S. Schmidt, and S. Strunk (1994), The Lithospheric Structure of the Central Andes (20-26S) as Inferred from Quantitative Interpretation of Regional Gravity, In: Reutter, K.-J., Scheuber, E., Wigger, P. (eds.) Tectonics of the Southern Central Andes, *Springer Verlag, Heidelberg*, pp. 7–21.

Gregory-Wodzicki, K. M. (2000), Uplift history of the Central and Northern Andes: A review, *Geol. Soc. Am. Bull.*, *112*(7), 1091–1105, doi:10.1130/0016-7606(2000)112.

Guillaume, B., J. Martinod, and N. Espurt (2009), Variations of slab dip and overriding plate tectonics during subduction: insights from analogue modeling, *Tectonophysics*, *469*, 1–12.

Gutscher, M.-A. (2002), Andean subduction styles and their effect on thermal structure and interplate coupling, *Journal of South American Earth Sciences*, *15*, 3–10.

Gutscher, M.-A., W. Spakman, H. Bijwaard, and E. R. Engdahl (2000), Geodynamics of flat subduction: Seismicity and tomographic constraints from the Andean margin, *Tectonics*, *19*(5), 814–833, doi:10.1029/1999TC001152.

Hampel, A., and A. Pfiffner (2006), Relative importance of trenchward upper plate motion and friction along the plate interface for the topographic evolution of subduction-related moutain belts, In: Buiter, S. J. H. and Schreurs, G. (eds.) Analogue and Numerical Modelling of Crustal-Scale proceses, *Geological Society, London, Special Publication*, *253*, 105–115.

Haschke, M., A. Günther, D. Melnick, H. Echtler, K.-J. Reutter, E. Scheuber, and O. Oncken (2006), Central and Southern Andean Tectonic Evolution Inferred from Arc Magmatism, In: Oncken, O., Chong, G., Franz, G., Giese, P., Götze, H.-J., Ramos, V. A., Strecker, M. and Wigger, P. (eds.) The Andes: Active subduction orogeny, *Frontiers in Earth Science Series*, pp. 337–353.

Heidbach, O., and H. Drewes (2003), 3D finite element model of major tectonic processes in the Eastern Mediterranean, In: D. A. Nieuwland (ed.) New Insights into Structural Interpretation and Modelling, *Geological Society, London, Special Publication*, *212*, 261–274, doi:10.1144/GSL.SP.2003.212.01.17.

Heidbach, O., G. Iaffaldano, and H.-P. Bunge (2008a), Topography growth drives stress rotations in the central Andes: Observations and models, *Geophys. Res. Lett.*, *35*, L0831, doi:10.1029/2007GL032782.

Heidbach, O., M. Tingay, A. Barth, J. Reinecker, D. Kurfeß, and B. Müller (2008b), The World Stress Map database release 2008, doi:10.1594/GFZ.WSM.Rel2008.

Hess, H. (1962), History of ocean basins, *Geol. Soc. Am. Bull., Petrologic Studies: A volume to Honour A. F. Buddington*, pp. 559–620.

Heuret, A., and S. Lallemand (2005), Plate motions, slab dynamics and back-arc deformation, *Phys. Earth Planet. In.*, *149*(1-2), 31 – 51, doi:10.1016/j.pepi.2004.08.022.

Hindle, D., J. Kley, E. Klosko, S. Stein, T. Dixon, and E. Norabuena (2002), Consistency of geologic and geodetic displacements during Andean orogenesis, *Geophys. Res. Lett.*, *29*, doi:10.1029/2001GL013757.

Hirth, G., and D. L. Kohlstedt (1996), Water in the oceanic upper mantle: Implications for rheology, melt extraction and the evolution of the lithosphere, *Earth Planet. Sci. Lett.*, *144*, 93–108.

Hoffmann-Rothe, A., N. Kukowski, G. Dresen, H. Echtler, O. Oncken, J. Klotz, E. Scheuber, and A. Kellner (2006), Oblique Convergence along the Chilean Margin: Partitioning, Margin-Parallel Faulting and Force Interaction at the Plate Interface, In: Oncken, O., Chong, G., Franz, G., Giese, P., Götze, H.-J., Ramos, V. A., Strecker, M. and Wigger, P. (eds.) The Andes: Active subduction orogeny, *Frontiers in Earth Science Series*, pp. 125–146.

Husen, S., E. Kissling, E. Flueh, and G. Asch (1999), Accurate hypocentre determination in the seismogenic zone of the subducting Nazca Plate in northern Chile using a combined on-/offshore network, *Geophys. J. Int.*, *138*(3), 687–701, doi:10.1046/j.1365-246x.1999.00893.x.

Hyndman, R. D., M. Yamano, and D. Oleskevich (1997), The seismogenic zone of subduction thrust faults, *The Island Arc*, *6*, 244–260.

Hyperworks version 11 (2011), Altair Engineering GMbH.

Jahr, T., G. Jentzsch, A. Gebauer, and T. Lau (2008), Deformation, seismicity, and fluids: Results of the 2004/2005 water injection experiment at the KTB/Germany, *J. Geophys. Res.*, *113*, B11,410, doi:10.1029/2008JB005610.

Jarrard, R. D. (1986), Relations among subduction parameters, *Rev. Geophys.*, *24*, 217–284.

Jordan, T. E., B. L. Isacks, R. W. Allmendinger, J. Brewer, V. A. Ramos, and C. J. Ando (1983), Andean tectonics related to geometry of subducted Nazca Plate, *Geol. Soc. Am. Bull.*, *94*, 341–361.

Kameyama, M., D. A. Yuen, and S.-I. Karato (1999), Thermal-mechanical effects of low-temperature plasticity (the Peierls mechanism) on the deformation of a viscoelastic shear zone, *Earth Planet. Sci. Lett.*, *168*, 159–172, doi:10.1016/S0012-821X(99)00040-0.

Kellner, A. (2007), Different styles of deformation of the fore-arc wedge along the Chilean convergent margin: Insights from 3D numerical experiments, Ph.D. thesis, Universität Potsdam.

Kendrick, E., M. G. Bevis, R. Smalley, and B. A. Brooks (2001), An integrated crustal velocity field for the central Andes, *Geochem. Geophys. Geosyst.*, *2*, doi: 10.1029/2001GC000191,.

Kennett, B. L. N., and H.-P. Bunge (2008), *Geophysical Continua*, Cambridge University Press, Cambridge, 432 p.

Khazaradze, G., and J. Klotz (2003), Short- and long-term effects of GPS measured crustal deformation rates along the south central Andes, *J. Geophys. Res.*, *108*(B6), 2289, doi:10.1029/2002JB001879.

Kirchner, A., H.-J. Götze, and M. Schmitz (1996), 3D-density modelling with seismic constraints in the Central Andes, *Physics and Chemistry of The Earth*, *21*(4), 289–293, doi:10.1016/S0079-1946(97)00050-5.

Kley, J., and C. R. Monaldi (1998), Tectonic shortening and crustal thickness in the Central Andes: How good is the correlation?, *Geology*, *26*(8), 723–726.

Kley, J., and C. R. Monaldi (2002), Tectonic inversion in the Santa Barbara System of the central Andean foreland thrust belt, northwestern Argentina, *Tectonics*, *21(6)*, 1061, doi:10.1029/2002TC902003.

Kley, J., C. Monaldi, and J. A. Slafity (1999), Along-strike segmentation of the Andean foreland: Causes and consequences, *Tectonophysics*, *301*, 75–94.

Kösters, M. (1998), 3D-Dichtemodellierung des Kontinentalrandes sowie quantitative Untersuchungen zur Isostasie und Rigidität der Zentralen Anden (20° -26°S) , Ph.D. thesis, Berliner geowissenschaftliche Abhandlungen: Reihe B, Geophysik, 32, Freie Universität Berlin.

Köther, N., H.-J. Götze, B. D. Gutknecht, T. Jahr, G. Jentzsch, O. H. Lücke, R. Mahatsente, R. Sharma, and S. Zeumann (2012), The seimically active Andean and Central American margins: Can satellite gravity map lithospheric structures?, *J. Geodyn.*, *59-60*, 207–218, doi:10.1016/j.jog.2011.11.004.

Krabbenhöft, A., J. Bialas, H. Kopp, N. Kukowski, and C. Hübscher (2004), Crustal structure of the Peruvian continental margin from wide-angle seismic studies, *Geophys. J. Int*, *159*, 749–764.

Kukowski, N., and O. Oncken (2006), Subduction Erosion the "Normal" Mode of Fore-Arc Material Transfer along the Chiean Margin?, In: Oncken, O., Chong, G., Franz, G., Giese, P., Götze, H.-J., Ramos, V. A., Strecker, M. and Wigger, P. (eds.) The Andes: Active subduction orogeny, *Frontiers in Earth Science Series*, pp. 217–236.

Kurz, J. H., T. Jahr, and G. Jentzsch (2004), Earthquake swarm examples and a look at the generations mechanism of the Vogtland/Western Bohemia earthquake swarms, *Phys. Earth Planet. In.*, *142*, 75–88.

Lamb, S., and P. Davis (2003), Cenozoic climate change as a possible cause for the rise of the Andes, *Nature*, *425*(6960), 792–797, doi:10.1038/nature02049.

Lamb, S., and L. Hoke (1997), Origin of the high plateau in the central Andes, Bolivia, South America, *Tectonics*, *16*(4), 623–649, doi:10.1029/97TC00495.

Leier, M. (2007), *Weltatlas der Ozeane*, 264 pp., Frederking & Thaler Verlag GmbH, München.

Lithgow-Bertelloni, C., and M. A. Richards (1998), The dynamics of Cenozoic and Mesozoic Plate motions, *Rev. Geophys.*, *36*(1), 27–78.

Liu, M., Y. Yang, S. Stein, and E. Klosko (2002), Crustal Shortening and Extension in the Central Andes: Insights from a Viscoelastic Model, In: Stein, S., and J. T. Freymueller (eds.) Plate Boundary Zones, *AGU Geodyn. Ser.*, *30*, 325–339, doi:10.1029/030GD19.

Mahatsente, R., G. Ranalli, D. Bolte, and H.-J. Götze (2012), On the relation between lithospheric strength and ridge push transmission in the Nazca plate, *J. Geodyn.*, *53*, 18–26, doi:10.1016/j.jog.2011.08.002.

Mayer-Gürr, T. (2007), ITG-Grace03s: The latest GRACE gravity field solution computed in Bonn, in *GSTM+SPP conference Potsdam*.

Montgomery, D. R., G. Balco, and S. D. Willett (2001), Climate, tectonics, and the morphology of the Andes, *Geology*, *29*, 579–582.

Mpodozis, C., and V. A. Ramos (1989), The Andes of Chile and Argentina. In: Ericksen, G., Canas-Pinochet, M., Reinemund, J. (Eds.), Geology of the Andes and its Relation to Hidrocarbon and Mineral Resources, *Circum-Pacific Council for Energy and Mineral Resources Earth Sciences Series*, *11*, 59–90.

Müller, R. D., W. R. Roest, J.-Y. Royer, L. M. Gahagan, and J. G. Sclater (1997), Digital isochrones of the world's ocean floor, *J. Geophys. Res.*, *102*, 3211–3214.

Müller, R. D., C. Gaina, and W. R. Roest (2008), Age, spreading rates, and spreading asymmetry of the worlds ocean crust, *Geochem. Geophys. Geosyst.*, *9*(4), Q04,006, doi:10.1029/2007GC001743.

Nüchter, J.-A., and S. Ellis (2010), Complex states of stress during the normal faulting seismic cycle: Role of midcrustal postseismic creep, *J. Geophys. Res.*, *115*, B12,411, doi:10.1029/2010JB007557.

Oleskevich, D., R. D. Hyndman, and K. Wang (1999), The updip and downdip limits to great subduction earthquakes: Thermal and structural models of Casdadia, south Alaska, SW Japan and Chile, *J. Geophys. Res.*, *4*, 14,965–14,991.

Oncken, O., D. Hindle, J. Kley, K. Elger, P. Victor, and K. Schemman (2006a), Deformation of the Central Andean Upper Plate System - Facts, Fiction, and Constraints for Plateau Models, In: Oncken, O., Chong, G., Franz, G., Giese, P., Götze, H.-J., Ramos, V. A., Strecker, M. and Wigger, P. (eds.) The Andes: Active subduction orogeny, *Frontiers in Earth Science Series*, pp. 3–27.

Oncken, O., G. Chong, G. Franz, P. Giese, H.-J. Götze, V. A. Ramos, M. Strecker, and P. Wigger (2006b), *The Andes: Active Subduction Orogeny*, *Frontiers in Earth Science Series*, vol. 1, 567 pp., Springer-Verlag, Berlin Heidelberg New York.

Ortlieb, L., C. Zazs, J. L. Goy, C. Hillaire-Marcel, B. Ghaleb, and L. Cournoyer (1996a), Coastal deformation and sea-level changes in the northern Chile subduction area (23°S) during the last 330 ky, *Quat Sci Rev*, *15*, 819–831.

Ortlieb, L., C. Zazs, J. L. Goy, C. Dabrio, and J. Macharé (1996b), Pampa del Palo: An anomalous composite marine terrace on the uprising coast of southern Peru, *Journal of South American Earth Sciences*, *9*, 367–379.

Pail, R., H. Goiginger, W.-D. Schuh, E. Höck, J. M. Brockmann, T. Fecher, T. Gruber, T. Mayer-Gürr, J. Kusche, A. Jäggi, and D. Rieser (2010), Combined satellite gravity field model GOCO01S derived from GOCE and GRACE, *Geophys. Res. Lett.*, *37*, L20,314, doi:10.1029/2010GL044906.

Pail, R., S. Bruinsma, F. Migliaccio, C. Förste, H. Goiginger, W.-D. Schuh, E. Höck, M. Reguzzoni, J. M. Brockmann, O. Abrikosov, M. Veicherts, T. Fecher, R. Mayrhofer, I. Krasbutter, F. Sanso, and C. C. Tscherning (2011), First GOCE gravity field models derived by three different approaches, *J. Geodesy*, *85*, 819–843.

Patzwahl, R., J. Mechie, A. Schulze, and P. Giese (1999), Two-dimensional velocity models of the Nazca Plate subduction zone between 19.5°S and 25°S from wide-angle seismic measurements during the CINCA95 project, *J. Geophys. Res.*, *104(B4)*, 7293–7317, doi:10.1029/1999JB900008.

Pavlis, N. K., S. A. Holmes, S. C. Kenyon, and J. K. Factor (2008), An Earth Gravitational Model to Degree 2160: EGM 2008, *EGU General Assembly, Vienna*.

Pope, D. C., and S. D. Willett (1998), Thermal-mechanical model for crustal thickening in the central Andes driven by ablative subduction, *Geology*, *26*(6), 511–514, doi: 10.1130/0091-7613.

Prawirodirdjo, L., and Y. Bock (2004), Instantaneous global plate motion model from 12 years GPS observations, *J. Geophys. Res.*, *109*, B08,405.

Press, F., and R. Siever (2003), *Allgemeine Geologie - Einführung in das System Erde*, Elsevier GMbH, München.

Prezzi, C. B., H.-J. Götze, and S. Schmidt (2009), 3D density model of the Central Andes, *Phys. Earth Planet. In.*, *177*, 217–234, doi:10.1016/j.pepi.2009.09.004.

Ramos, V. A. (2005), Seismic ridge subduction and topography: Foreland deformation in the Patagonian Andes, *Tectonophysics*, *399*, 73–86, doi:10.1016/j.tecto.2004.12.016.

Ramos, V. A. (2010), The tectonic regime along the Andes: Present-day and Mesozoic regimes, *Geol. J.*, *45*, 2–25, doi:10.1002/gj.1193.

Ranalli, G. (1995), *Rheology of the Earth*, Chapman & Hall, New York, 413 p.

Reigber, C., R. Schmidt, F. Flechtner, R. König, U. Meyer, K.-H. Neumayer, P. Schwintzer, and S. Y. Zhu (2005), An Earth gravity field model complete to degree and order 150 from GRACE: EIGEN-GRACE02S, *J. Geodyn.*, *39*(1), 1 – 10, doi:10.1016/j.jog.2004.07.001.

Reutter, K.-J., and H.-J. Götze (1994), Comments on the geological and geophysical maps, In: Reutter, K.-J. , Scheuber, E., Wigger, P. (eds.) Tectonics of the Southern Central Andes, *Springer Verlag, Heidelberg*, pp. 329–333.

Russo, R. M., and P. G. Silver (1996), Cordillera formation, mantle dynamics, and the Wilson cycle, *Geology*, *24*, 511–514, doi:10.1130/0091-7613(1996)0240511:CFMDAT2.3.CO;2.

Rutland, R. (1971), Andean orogeny and ocean floor spreading, *Nature*, *233*, 252–255.

Saffer, D. M., and C. Maroneb (2003), Comparison of smectite- and illite-rich gouge frictional properties: Application to the updip limit of the seismogenic zone along subduction megathrusts, *Earth Planet. Sci. Lett.*, *215*(1-2), 219–235, doi:10.1016/S0012-821X(03)00424-2.

Sandiford, M., D. D. Coblentz, and R. M. Richardson (1995), Ridge torques and continental collision in the Indian-Australian plate , *Geology*, *23*, 653–656, doi:10.1130/0091-7613(1995)0230653:RTACCI2.3.CO;2.

Schellart, W. P. (2004), Quantifying the net slab pull force as a driving mechanism for plate tectonics, *Geophys. Res. Lett.*, *31*, L07,611, doi:10.1029/2004GL019528.

Schellart, W. P. (2008), Overriding plate shortening and extension above subduction zones: a parametric study to explain formation of the Andes Mountains, *Geol. Soc. Am. Bull.*, *120*, 1441–1454.

Scheuber, E., T. Bogdanic, A. Jensen, and K.-J. Reutter (1994), Tectonic development of the north Chilean Andes in relation to plate convergence and magmatism since the Jurassic, In: Reutter, K.-J. , Scheuber, E., Wigger, P. (eds.) Tectonics of the Southern Central Andes, *Springer Verlag, Heidelberg*, pp. 7–22.

Schmidt, S., and H.-J. Götze (1998), Interactiv visualization and modification of 3D models using GIS functions, *Physics and Chemistry of The Earth*, *23*, 289–296.

Schmidt, S., and H.-J. Götze (2006), Bouguer and Isostatic Maps of the Central Andes, In: Oncken, O., Chong, G., Franz, G., Giese, P., Götze, H.-J., Ramos, V. A., Strecker, M. and Wigger, P. (eds.) The Andes: Active subduction orogeny, *Frontiers in Earth Science Series*, pp. 559–562.

Schmidt, S., H.-J. Götze, C. Fichler, and M. Alvers (2010), IGMAS+ a new 3D Gravity, FTG and Magnetic Modeling Software, In: A. Zipf, K. Behncke, F. Hillen and J. Schefermeyer (eds.) GEOINFORMATIK 2010 "Die Welt im Netz", *Akademische Verlagsgesellschaft AKA GmbH*, pp. 57–63.

Schurr, B., G. Asch, M. Rosenau, R. Wang, O. Oncken, S. Barrientos, P. Salazar, and J.-P. Vilotte (2012), The 2007 M7.7 Tocopilla northern Chile earthquake sequence: Implications for along-strike and downdip rupture segmentation and megathrust frictional behavior, *J. Geophys. Res.*, *117*, B05,305, doi:10.1029/2011JB009030.

Silver, P. G., R. M. Russo, and C. Lithgow-Bertelloni (1998), Coupling of South American and African Plate Motion and Plate Deformation, *Science*, *279*, 60–63, doi: 10.1126/science.279.5347.60.

Sobolev, S. V., and A. Y. Babeyko (2005), What drives orogeny in the Andes?, *Geology*, *33*, 617–620, doi:10.1130/G21557.1.

Somoza, R. (1998), Updated Nazca (Farallon) - South America relative motions during the last 40 My: Implications for mountain building in the central Andean region, *Journal of South American Earth Sciencesi*, *11*(3), 211–215.

Springer, M. (1999), Interpretation of heat-flow density in the Central Andes, *Tectonophysics*, *306*, 377–395.

Stein, S., and G. F. Sella (2002), Plate Boundary Zones: Concept and Approaches, In: Stein, S., and J. T. Freymueller (eds.) Plate Boundary Zones, *AGU Geodyn. Ser.*, *30*, 1–26, doi:10.1029/030GD01.

Strunk, S. (1990), Analyse und Interpretation des Schwerefeldes des aktiven Kontinentalrandes der zentralen Anden (20 - 26°S) , Ph.D. thesis, Berliner geowissenschaftliche Abhandlungen : Reihe B, Geophysik ; Bd. 17, Freie Universität Berlin.

Tassara, A. (2005), Interaction between the Nazca and South American plates and formation of the Altiplano-Puna plateau: Review of a flexural analysis along the Andean margin (15°-34°S), *Tectonophysics*, *399*, 39 57.

Tassara, A., H.-J. Götze, S. Schmidt, and R. Hackney (2006), Three-dimensional density model of the Nazca plate and the Andean continental margin, *J. Geophys. Res.*, *111*, B09,404, doi:10.1029/2005JB003976.

Tašárová, Z. A. (2007), Towards understanding the lithospheric structure of the southern Chilean subduction zone (36°S-42°S) and its role in the gravity field, *Geophys. J. Int*, *170*(3), 9951014, doi:10.1111/j.1365-246X.2007.03466.x.

Tichelaar, B. W., and L. J. Ruff (1991), Seismic coupling along the Chilean Subduction Zone, *J. Geophys. Res.*, *96*(B7), 11,997, doi:10.1029/91JB00200.

Tichelaar, B. W., and L. J. Ruff (1993), Depth of Seismic Coupling Along Subduction Zones, *J. Geophys. Res.*, *98(B2)*, 2017–2037.

Turcotte, D., and G. Schubert (2002), *Geodynamics*, Cambridge University Press, Cambridge, 456 p.

Uyeda, S., and H. Kanamori (1979), Back-arc opening and the mode of subduction, *J. Geophys. Res.*, *84*, 1049–1061.

Vermeer, P. A., and R. de Borst (1984), Non-associated plasticity for soils, concrete and rocks, *HERON*, *29*(3), 1–64.

Victor, P., O. Oncken, and J. Glodny (2004), Uplift of the western Altiplano plateau: Evidence from the Precordillera between 20° and 21°S (northern Chile), *Tectonics*, *23*, TC4004, doi:10.1029/2003TC001519.

Wang, K., and K. Suyehiro (1999), How does plate coupling affect crustal stresses in northeast and southwest japan?, *Geophys. Res. Lett.*, *26*(15), 2307–2310.

Wessel, P., and R. D. Müller (2009), Plate Tectonics, In: Schubert, G. and Watts, A. B. (eds.) Crust and Lithosphere Dynamics, *Treatise on Geophysics*, *6*, 49–98.

Wigger, P., M. Schmitz, M. Araneda, G. Asch, S. Baldzuhn, P. Giese, W.-D. Heinsohn, E. Martinez, E. Ricaldi, P. Rwer, and J. Viramonte (1994), Variation in the Crustal Structure of the Southern Central Andes Deduced from Seismic Refraction Investigations, In: Reutter, K.-J. , Scheuber, E., Wigger, P. (eds.) Tectonics of the Southern Central Andes, *Springer Verlag, Heidelberg*, pp. 23–48.

Wilson, J. T. (1965), A new class of faults and their bearing on continental drift, *Nature*, *207*, 343–347.

Yuan, X., S. V. Sobolev, R. Kind, O. Oncken, and Andes Seismology Group (2000), New constraints on subduction and collision processes in the central Andes from comprehensive observations of P to S converted seismic phases, *Nature*, *408*, 958–961.

Zeumann, S., R. Sharma, R. Gassmöller, T. Jahr, and G. Jentzsch (2013), New Finite-Element modelling of subduction processes in the Andes using realistic geometries, *Proceedings of the 2011 IAG Symposium, Melbourne, Australia, IAG Symposia*, *139, in press.*

Zienkiewicz, O. C., R. L. Taylor, J. Z. Zhu, and P. Nithiarasu (2005), *The finite element method*, Butterworth-Heinemann.

Figures 1.2, 2.1, 2.5, 5.15, and 5.16 were created with the GMT software package (by Wessel and Smith; http://gmt.soest.hawaii.edu/).

Appendix

The following pages show the ABAQUS-input file for the reference model.

```
*Heading
** Job name: tn_b_sp5rp5_lithel_nP_ini4 Model name:
 tn_b_sp5rp5_lithel_nP_ini4
** Generated by: Abaqus/CAE 6.10-EF1
*Preprint, echo=NO, model=NO, history=NO, contact=NO
**
** PARTS
**
*Part, name=PART-1
*Node
      1,   233721.672,    8068386.5,  -46023.7852
      ...
      (ALL OTHER NODE COORDINATES)
*Element, type=C3D4
      1,  49936,  49835,  49780,  49883
      ...
      (ALL OTHER ELEMENTS)
*Elset, elset=OA, generate
    1,  1306,     1
...
(ALL OTHER UNITS)
*Nset, nset=OA_bottom
 49840, 49841, 49842,
 ....
(ALL OTHER NODE SETS)
*Elset, elset=_Con_OC_fric_S1, internal
 131227, 135200, 137863,
 ...
(ALL OTHER ELEMENT SETS)
** Section: Section-1-MESH-OA
*Solid Section, elset=MESH-OA, material=OA
1.,
...
(ALL OTHER UNITS)
*End Part
**
** ASSEMBLY
**
*Assembly, name=Assembly
**
*Instance, name=PART-1-1, part=PART-1
*End Instance
**
** Constraint: CA_UCA
*Tie, name=CA_UCA, adjust=yes, position tolerance=4000., type=SURFACE TO SURFACE
```

```
PART-1-1.UCA_CA, PART-1-1.CA_UCA
** Constraint: LC_UC
*Tie, name=LC_UC, adjust=yes, position tolerance=4000., type=SURFACE TO SURFACE
PART-1-1.UC_LC, PART-1-1.LC_UC
** Constraint: OM_OC
*Tie, name=OM_OC, adjust=yes, position tolerance=4000., type=SURFACE TO SURFACE
PART-1-1.OC_OM, PART-1-1.OM_OC
*End Assembly
**
** MATERIALS
**
*Material, name=CA
*Creep
 3.33e-22,1.,0.
*Density
3430.,
*Elastic
 2.07e+11, 0.25
*Material, name=CM
*Density
3320.,
*Elastic
 1.36e+11, 0.25
*Material, name=LC
*Density
3100.,
*Elastic
 1.03e+11, 0.25
*Material, name=MW
*Density
3230.,
*Elastic
 1.1e+11, 0.25
*Material, name=OA
*Creep
 3.33e-22,1.,0.
*Density
3411.,
*Elastic
 2.05e+11, 0.25
*Material, name=OCI+II
*Density
3050.,
*Elastic
 9.8e+10, 0.25
*Material, name=OCIII
*Density
3200.,
```

```
*Elastic
 1.13e+11, 0.25
*Material, name=OCIV
*Density
3300.,
*Elastic
 1.16e+11, 0.25
*Material, name=OCV
*Density
3550.,
*Elastic
 1.25e+11, 0.25
*Material, name=OMI+II
*Density
3350.,
*Elastic
 1.83e+11, 0.25
*Material, name=OMIII
*Density
3370.,
*Elastic
 1.84e+11, 0.25
*Material, name=OMIV
*Density
3400.,
*Elastic
 1.86e+11, 0.25
*Material, name=OMV
*Density
3500.,
*Elastic
 1.91e+11, 0.25
*Material, name=UC
*Density
2700.,
*Elastic
 7.8e+10, 0.25
*Material, name=UCAE
*Creep
 3.33e-20,1.,0.
*Density
3350.,
*Elastic
 1.83e+11, 0.25
*Material, name=UCAW
*Creep
 3.33e-20,1.,0.
*Density
```

```
3320.,
*Elastic
 1.64e+11, 0.25
*INITIAL CONDITIONS,Type=stress,unbalanced stress=step,input=stress4_nP.inp
**
** INTERACTION PROPERTIES
**
*Surface Interaction, name=free
1.,
*Friction
0.,
*Surface Behavior, no separation, pressure-overclosure=HARD
*Surface Interaction, name=fric
1.,
*Friction, slip tolerance=0.005
 0.3,
*Surface Behavior, no separation, pressure-overclosure=HARD
**
** INTERACTIONS
**
** Interaction: CON_OC_free
*Contact Pair, interaction=free, type=SURFACE TO SURFACE, adjust=3000.
PART-1-1.OC_CON, PART-1-1.CON_OC_free
** Interaction: OA_OM
*Contact Pair, interaction=free, type=SURFACE TO SURFACE, adjust=4000.
PART-1-1.OM_OA, PART-1-1.OA_OM
** Interaction: OC_CON_fric
*Contact Pair, interaction=fric, type=SURFACE TO SURFACE, adjust=3000.
PART-1-1.Con_OC_fric, PART-1-1.OC_CON
** Interaction: UCA_MWCM
*Contact Pair, interaction=free, type=SURFACE TO SURFACE, adjust=4000.
PART-1-1.MWCM_UCA, PART-1-1.UCA_MWCM
** ----------------------------------------------------------------
**
** STEP: Step-1
**
*Step, name=Step-1, nlgeom=YES, inc=1
*Static
1., 1., 1e-05, 1.
**
** BOUNDARY CONDITIONS
**
** Name: CON_Asth_ost Type: Symmetry/Antisymmetry/Encastre
*Boundary
PART-1-1.CON_Asth_ost, XSYMM
** Name: CON_Lith_ost Type: Symmetry/Antisymmetry/Encastre
*Boundary
PART-1-1.CON_Lith_ost, XSYMM
```

```
** Name: CON_bottom Type: Symmetry/Antisymmetry/Encastre
*Boundary
PART-1-1.CON_bottom, ZSYMM
** Name: CON_nord Type: Symmetry/Antisymmetry/Encastre
*Boundary
PART-1-1.CON_nord, YSYMM
** Name: CON_sued Type: Symmetry/Antisymmetry/Encastre
*Boundary
PART-1-1.CON_sued, YSYMM
** Name: OA_bottom Type: Symmetry/Antisymmetry/Encastre
*Boundary
PART-1-1.OA_bottom, ZSYMM
** Name: OA_nord Type: Symmetry/Antisymmetry/Encastre
*Boundary
PART-1-1.OA_nord, YSYMM
** Name: OA_sued Type: Symmetry/Antisymmetry/Encastre
*Boundary
PART-1-1.OA_sued, YSYMM
** Name: OA_west Type: Symmetry/Antisymmetry/Encastre
*Boundary
PART-1-1.OA_west, XSYMM
** Name: OCOM_bottom Type: Symmetry/Antisymmetry/Encastre
*Boundary
PART-1-1.OCOM_bottom, ZSYMM
** Name: OCOM_nord Type: Symmetry/Antisymmetry/Encastre
*Boundary
PART-1-1.OCOM_nord, YSYMM
** Name: OCOM_sued Type: Symmetry/Antisymmetry/Encastre
*Boundary
PART-1-1.OCOM_sued, YSYMM
** Name: OCOM_west Type: Symmetry/Antisymmetry/Encastre
*Boundary
PART-1-1.OCOM_west, XSYMM
**
** LOADS
**
** Name: GRAVITY-1   Type: Gravity
*Dload
, GRAV, 9.81, 0., 0., -1.
**
** OUTPUT REQUESTS
**
*Restart, write, frequency=0
*Print, solve=NO
**
** FIELD OUTPUT: F-Output-1
**
*Output, field
```

```
*Node Output
U,
*Element Output, directions=YES
LE, S
**
** HISTORY OUTPUT: H-Output-1
**
*Output, history, variable=PRESELECT
*End Step
** ----------------------------------------------------------------
**
** STEP: Step-2
**
*Step, name=Step-2, nlgeom=YES, inc=100000
*Visco, cetol=0.01
2e+08, 3.15e+12, 1e-05, 3.15e+12
**
** BOUNDARY CONDITIONS
**
** Name: CON_Asth_ost Type: Symmetry/Antisymmetry/Encastre
*Boundary, op=NEW
PART-1-1.CON_Asth_ost, XSYMM
** Name: CON_Lith_ost Type: Symmetry/Antisymmetry/Encastre
*Boundary, op=NEW
** Name: CON_Lith_ost_v Type: Velocity/Angular velocity
*Boundary, op=NEW, type=VELOCITY
PART-1-1.CON_Lith_ost, 1, 1, -8.89e-10
** Name: CON_bottom Type: Symmetry/Antisymmetry/Encastre
*Boundary, op=NEW
PART-1-1.CON_bottom, ZSYMM
** Name: CON_nord Type: Symmetry/Antisymmetry/Encastre
*Boundary, op=NEW
PART-1-1.CON_nord, YSYMM
** Name: CON_sued Type: Symmetry/Antisymmetry/Encastre
*Boundary, op=NEW
PART-1-1.CON_sued, YSYMM
** Name: OA_bottom Type: Symmetry/Antisymmetry/Encastre
*Boundary, op=NEW
PART-1-1.OA_bottom, ZSYMM
** Name: OA_nord Type: Symmetry/Antisymmetry/Encastre
*Boundary, op=NEW
PART-1-1.OA_nord, YSYMM
** Name: OA_sued Type: Symmetry/Antisymmetry/Encastre
*Boundary, op=NEW
PART-1-1.OA_sued, YSYMM
** Name: OA_west Type: Symmetry/Antisymmetry/Encastre
*Boundary, op=NEW
PART-1-1.OA_west, XSYMM
```

```
** Name: OCOM_bottom Type: Symmetry/Antisymmetry/Encastre
*Boundary, op=NEW
** Name: OCOM_bottom_v Type: Velocity/Angular velocity
*Boundary, op=NEW, type=VELOCITY
PART-1-1.OCOM_bottom, 1, 1, 1.29e-09
PART-1-1.OCOM_bottom, 3, 3, -7.45e-10
** Name: OCOM_nord Type: Symmetry/Antisymmetry/Encastre
*Boundary, op=NEW
** Name: OCOM_nord_v Type: Velocity/Angular velocity
*Boundary, op=NEW, type=VELOCITY
PART-1-1.OCOM_nord, 2, 2, 2.7e-10
** Name: OCOM_sued Type: Symmetry/Antisymmetry/Encastre
*Boundary, op=NEW
** Name: OCOM_sued_v Type: Velocity/Angular velocity
*Boundary, op=NEW, type=VELOCITY
PART-1-1.OCOM_sued, 2, 2, 2.7e-10
** Name: OCOM_west Type: Symmetry/Antisymmetry/Encastre
*Boundary, op=NEW
** Name: OCOM_west_v Type: Velocity/Angular velocity
*Boundary, op=NEW, type=VELOCITY
PART-1-1.OCOM_west, 1, 1, 1.49e-09
**
** OUTPUT REQUESTS
**
*Restart, write, frequency=0
*Print, solve=YES
**
** FIELD OUTPUT: F-Output-2
**
*Output, field, number interval=20
*Node Output
U,
*Element Output, directions=YES
CE, CEEQ, CEP, E, EE, IE, LE, S, VE
**
** HISTORY OUTPUT: H-Output-1
**
*Output, history, variable=PRESELECT
*End Step
```

Acknowledgements

First I would like to sincerely thank my supervisors PD Dr. Thomas Jahr and Prof. Dr. Gerhard Jentzsch for providing me this interesting topic and spending their time for discussions on my work. Their hints and suggestions help to improve this work a lot. Besides them, I want to thank especially Dr. Adelheid Weise for scientific and non-scientific discussions and her help. I gratefully acknowledge the German Research Foundation (DFG) for the financial support.

I thank the whole working group of "Applied and General Geophysics" and the other colleagues of the Institute of Geoscience for the joyful time at the institute.

I gratefully acknowledge Prof. Hans-Jürgen Götze for his hints on the project meetings and his agreement to be an external reviewer of my thesis. My thank goes to Dr. Andrés Tassara for providing his density model.

I am thankful to Dr. Kasper Fischer, Dr. Jens-Alexander Nüchter, Dr. André Gebauer, René Gassmöller, Rebekka and Dr. Holger Steffen, and all participants of the ABAQUS workshop 2012, for there help with ABAQUS. Dr. Anne Hegewald and Dr. Markus Müller are thanked for the introduction in the world of gmt.

I would like to thank all project partners of University Kiel and TU Munich: Benjamien Gutknecht, Dr. Martin Horwath, Michael Hosse, Nils Köther, Oscar Lücke, Rezene Mahatsente, Prof. Roland Pail for the helpful discussions on the project meetings. I thank Rekha Sharma for helpful hints.

My final words go to my parents and family. Thanks for your encouragement, support, and for always believing in me.

Selbständigkeitserklärung

Ich erkläre, dass ich die vorliegende Arbeit selbständig und unter Verwendung der angegebenen Hilfsmittel, persönlichen Mitteilungen und Quellen angefertigt habe.

Jena, den 24. Juli 2013

Stefanie Zeumann